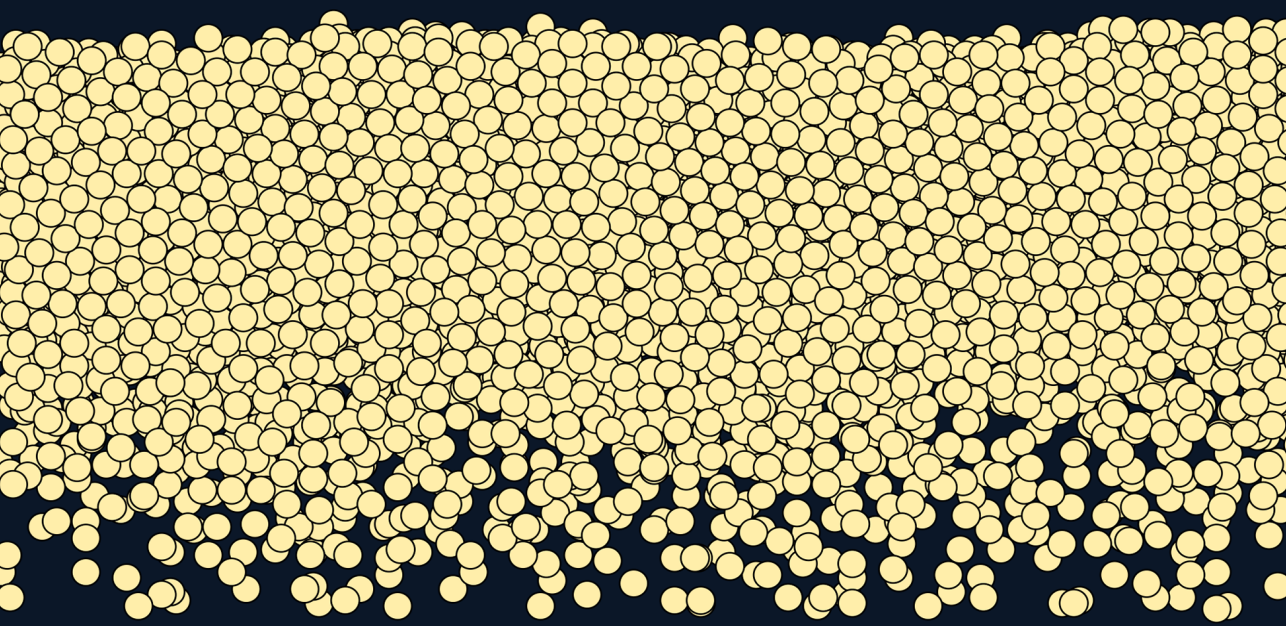


Discrete and Continuum Descriptions of Shaken Granular Matter

Nicolás Rivas



DISCRETE AND CONTINUUM DESCRIPTIONS OF
SHAKEN GRANULAR MATTER

NICOLÁS ALEJANDRO RIVAS ABUD

Thesis committee members:

Promotor

Prof. Dr. rer. nat. S. Luding Universiteit Twente

Assistent promotor

Dr. A.R. Thornton Universiteit Twente

Commission

Prof. Dr. D. van der Meer Universiteit Twente
Prof. Dr. J.D.R. Harting Technische Universiteit Eindhoven
Dr. A. Puglisi Sapienza – Università di Roma
Prof. Dr. T. Pöschel Universität Erlangen-Nürnberg
Dr. A.J. Hogg University of Bristol

MESA+

INSTITUTE FOR NANOTECHNOLOGY

The work in this thesis was carried out at the Multiscale Mechanics group, MESA+ Institute for Nanotechnology, Faculty of Science and Technology (CTW) of the University of Twente, Enschede, The Netherlands.

This work was financially supported by the NWO-STW VICI grant number 10828, “Bridging the gap between particulate systems and continuum theory.”

This work (included the cover image) is licensed under the Creative Commons Attribution 3.0 Unported License. To view a copy of this license, visit <http://creativecommons.org/licenses/by/3.0/> or send a letter to Creative Commons, 444 Castro Street, Suite 900, Mountain View, California, 94041, USA.

ISBN: 978-90-365-3815-2

DOI nummer: 10.3990/1.9789036538152

Officiële URL: <http://dx.doi.org/10.3990/1.9789036538152>

DISCRETE AND CONTINUUM DESCRIPTIONS OF SHAKEN GRANULAR MATTER

DISSERTATION

to obtain
the degree of doctor at the University of Twente,
on the authority of the rector magnificus,
Prof. Dr. H. Brinksma,
on account of the decision of the graduation committee,
to be publicly defended
on Friday the 20th of February 2015 at 12:45

by

Nicolás Alejandro Rivas Abud
Born on the 19th of April 1985
in Santiago, Chile

This dissertation has been approved by the promotor:

Prof. Dr. rer. nat. Stefan Luding

and the assistant-promotor:

Dr. Anthony R. Thornton

Contents

1 Granular matter, an inland problem	11
1.1 Granular materials definition	12
1.2 Granular flow	14
1.3 Granular matter as a complex system	16
1.4 Vibrated granular materials	17
1.5 Simulation of granular materials	19
1.6 Thesis outline	23
2 Low-frequency oscillations in vibrated granular systems	25
2.1 Introduction	26
2.2 Simulations	27
2.3 Continuum model	36
2.4 Thermodynamic model	42
2.5 Conclusions	43
3 Low-frequency oscillations and convective phenomena in a vibrated granular system	47
3.1 Introduction	48
3.2 System Details	48
3.3 Results and Analysis	52
3.4 Conclusions	58
4 From granular Leidenfrost to buoyancy-driven convection	59
4.1 Introduction	60
4.2 System and simulations	61
4.3 Results	63
4.4 Conclusions	76

5 On creating macroscopically identical granular systems with significantly different number of particles	79
5.1 Introduction	80
5.2 Granular hydrodynamics particle-size dependencies	81
5.3 Granular Leidenfrost system	85
5.4 Simulations	87
5.5 Conclusions	94
6 Hydrodynamics of the granular Leidenfrost to convection transition	97
6.1 Introduction	98
6.2 System and simulations	99
6.3 Granular hydrodynamics model	99
6.4 One-dimensional steady state	102
6.5 Boussinesq approximation	105
6.6 Conclusions	108
7 Conclusions and Outlook	113
Bibliography	119
Acknowledgements	133
Publications	135
Summary	137
Samenvatting	139

A mi madre.

1

INTRODUCTION: GRANULAR MATTER, AN INLAND PROBLEM

Such simple things,
And we make of them something so complex it defeats us,
Almost.

—John Ashbery

The Waldseemüller map, published in 1507 by German cartographer Martin Waldseemüller, is known for being the first map that uses the name “America” for the then newly recognized continent. It is wonderful to look at; beautiful not only for its intricate illuminated borders and detailed illustrations, but also for the scientific accomplishment that lies behind, and the spirit of knowledge that must have inspired it. It might make us laugh, at first sight, for its easily comical imprecision. But on second thought, after a quick reflection on what would it have taken to make a map of the world in the XVI century, it may reveal to us as an Herculean feat. It is the collection of small fragments of information, taken from thousands of travellers and sent by ship and land for years, summarized and arranged in one careful illustration. After years of coming back to this map, by chance and purpose, the feature that now most deeply calls my attention is the marked difference on the level of detail between coast and inland. While names of ports and sites populate the coast of America, inland the map is basically empty; no names, no rivers, not even monsters, just a honest depiction of lack of information.

Just as classic cartography, physics struggles with the middle lands. Curiosity hints that it is precisely there, in these unexplored no-man’s lands, where richness usually lies. It is these blank patches and the drive for knowledge what sets the pace of determined research. But the path is difficult. Full of illusions, every student quickly learns in the first hard years of their training that physics is, in its more fun-

electronic computers, and statistical physics methods are to be applied with care, as such crucial assumptions as molecular chaos may no longer be valid. The number of particles involved is the first challenge to overcome in the study of granular materials.

Grains –the constituent particles of granular media– are usually considered to lie in between $1\mu\text{m}$ and the size of asteroids, that is, in the 10^5m range. Even though common behaviours have been observed in this wide range of length-scales, most of the research has centred on micro- to centimetric particles, as they can be manufactured and handled with precision, to be used in various experiments. These are, also, the scales most relevant for practical applications. The lower size limit is set by the influence of thermal fluctuations: granular materials are defined to be athermal, in the sense that fluctuations due to temperature do not have a relevant influence in their movement [1]. This has a fundamental physical consequence, as the (in-land) phase space of possible configurations is not explored unless the material is externally excited [1]. Granular materials thus exhibit metastable states which are far from global equilibrium, affecting the reproducibility of phenomena and making classical thermodynamic arguments inapplicable. The size of the grains is thus situated in a complicated mid-range, big enough so that external fluctuations and cohesive effects are negligible, but small enough so that self-gravity does not yet kick-in.

In fact, the characteristic of granular materials that is most relevant for the description of their behaviour stems from their size. Disregarding other effects [2, 3], the fundamental interaction of grains is through the contact forces present in every grain-grain collision. Being macroscopic, grains possess a large enough number of internal degrees of freedom such that at every collision, momentum and energy can be irreversibly converted into heat, or lost in deforming their internal structure, effects which generally have no influence on the macroscopic dynamics. Thus, granular media is said to be a dissipative system: energy is being constantly “lost” due to grain collisions. This should come as no surprise, as we intuitively know that sand dunes, rice grains or Lego-brick collections quickly come to a rest after being pushed, tilted or vibrated: that is, externally excited. The dissipative nature of granular media makes it an excellent candidate for the study of out-of-equilibrium systems, as will be shown in one of the chapters of this thesis, and provides another spectacularly hard property to take into account when trying to model their behaviour.

Summing up, we reach the usual definition of granular materials: conglomerations of solid, macroscopic and dissipative particles. Granular matter is studied in many different scenarios: flowing or static, from dry hard-sphere collections to soft polygons immersed in fluids. The variety of phenomena, applications and modelling challenges makes them a vast area of research. In particular, this thesis inserts itself in the multidisciplinary and decades long effort to answer one question: *how do granular materials flow?* We will study the movement of grains when externally excited through vibrations, and try to understand the origin of their unexpected be-

haviour. This is done using simulations, continuum modelling, and collaborations with fellow experimental researchers. Before we dwell into the specifics of our work, a general overview of the context of our research is given. First, the general challenges of granular flow are described, followed by a revision of previous research on the particular scenario considered, and finally introducing the numerical tools used.

1.2 GRANULAR FLOW

Without an external energy source grains will quickly come to a rest, and settle into mechanically stable configurations. The mechanical properties of such arrangements are complex and present strong deviations from classical elastic theory, due in great part to the inhomogeneity and anisotropy of their structure [4]. Modelling such properties has proven to be an exceptional challenge for both physical and mechanical engineering research [5], as theories must take into account both the microscopic and macroscopic scales.

In this thesis we will avoid the static packing scenario, keeping grains in movement by constantly injecting energy into the system. Body forces, usually gravity, can also sustain granular flows, as for example in the case of avalanches, although in our work we will focus on excitation through boundary forces. In general, grain flows are also particularly difficult to predict, due in part to ubiquitous phase-coexisting scenarios, as well as deviations from the usual distributions of velocity [6, 7]. Furthermore, they critically depend on the form and strength of energy injection [7, 8]. Notice how hard it usually is to pour sugar or salt from one container to another; we struggle with the amount of tilting needed to trigger the movement, and then the direction and strength of flow is not easy to predict. An enormous amount of research has been done, inspired in part by the relevant presence of granular flows in industry, as well as by the variety of interesting complex phenomena they exhibit.

After observing how sand falls through our hand, or pasta flows from the package to the pot, it naturally comes to mind that granular flow should be describable in terms of a continuum theory not so different from the one describing regular fluids, that is, the Navier-Stokes equations. In fact, most of the theoretical approaches to describe granular flow consist in reinterpreting the hydrodynamic fields and determining the appropriate constitutive relations, while the general form of the equations is borrowed from Newtonian classical fluids. It would be easy to conclude that this is to be expected, as closed granular systems also obey the basic laws used to derive the Navier-Stokes equations, that is, the conservation of mass and momentum [9]. Nevertheless, the questionable point of granular hydrodynamic theories resides not on the conservation laws, but on the assumption that the continuum hypothesis holds for granular flows [10]. That is, for a continuum description to be valid, we would at least demand that there exists something as a representative volume element, as also separation of scales. But inhomogeneous and anisotropic arrangements are the norm

in granular materials, making the definition of a unit cell complicated, especially at high packing densities. This is the fundamental reason for the need of micro-macro theories which can relate particular arrangements to universal macroscopic quantities. Furthermore, the Knudsen number quickly becomes greater than unity with increasing packing fraction, as the relevant length scale of the problem, that is, the size of the particles, is greater than the mean-free path [11]. The continuum approximation of this discrete medium is therefore, at first sight, not expected to be valid for all densities.

Surprisingly [9], even though the continuum hypothesis could be expected to fail for granular materials [10], granular hydrodynamics has had great success in describing flows in a number of different scenarios [12, 13, 14, 15, 16, 17, 18]. The success of such theories is in itself an interesting point and subject of ongoing research [15, 16]. Nevertheless, microstructures, correlations between fields, and non-Gaussian velocity distributions cannot be ignored in most cases, especially for higher densities and moderate to high dissipation. The development of granular continuum theories continues to be an active area of research [17, 19, 20, 21]; although significant progress has been made, researchers are far from a universal granular hydrodynamic theory, and even the existence of it is heavily questioned [9, 10].

Contrary to the continuity and momentum conservation equations, which in most cases keep their general form from classical systems, the energy conservation condition must account for the dissipative interaction of the grains. This is usually done by adding a sink term, the specific form of which depends on the particles' properties [9, 22]. On the other hand, energy injection is usually included in the boundary conditions; this imbalance between dissipation at the bulk and injection at the boundaries turns out to be crucial for the behaviour of many granular systems.

Most of the granular hydrodynamic theories start from the Boltzmann-Enskog extension of kinetic theory [23, 24, 25]. The solution to those equations involves finding an expression for the velocity distribution function, for which many approximation methods have been proposed [26, 27]. No closed form of the transport coefficients or the dissipation term exists for a general granular flow, although several expressions model the low-density, high elasticity limit. In these cases, theories show a remarkable agreement with numerical simulations and experiments. At some points in this thesis we will also make use of these expressions, and study the limits of their validity as a function of the number of particles involved. As will be seen, the constitutive relations are somewhat involved, and depend on parameters which are not straightforward to measure in experiments. Still, and even though the approximations made by kinetic-theory are far from realistic models of grains, these results are highly relevant, as continuum solutions can be scaled with no extra computation cost, while the discrete simulation of the amount of particles involved in many practical applications remains impractical. Again we recognize here a similar image: the limits have been resolved –of low densities and highly elastic particles— but things quickly become obscure going inland.

1.3 GRANULAR MATTER AS A COMPLEX SYSTEM

Granular materials have not only been studied in the context of complex fluids. Considered as a dissipative, out-of-equilibrium many-body system, excited granular matter is an excellent scenario for the study of complex dynamic phenomena. Typical behaviour of highly nonlinear dynamical systems is observed, such as pattern formation and hydrodynamic-like instabilities [28, 29]. Basic self-organization is also observed in a variety of different setups, and its study yields further insight into the influence of individual particle interactions on collective behaviour [29]. Broadly speaking, understanding the dynamics of these phenomena is relevant for many areas of active scientific research of far from equilibrium complex systems, such as colloids, foams, suspensions and biological self-assembled systems.

The observed complex behaviour of granular matter usually shares many characteristics with other condensed matter, molecular systems. Thus, the respective theories can often be applied to granular media, with varying degrees of success. The effort yields further insight into the universality of such theories, as granular materials usually relax or even violate some of their derivation conditions. It also explores further the relation between classical continuum fields and their granular equivalents, specially regarding the temperature field and its correct definition in macroscopic athermal systems. As an example, consider a vertically agitated two-dimensional granular monolayer. It has been shown that as energy is increased, grains go from a highly ordered crystalline state to a two-dimensional fluid-like behaviour. This process was observed to be very similar to the scenario described by the Kosterlitz, Thouless, Halperin, Nelson and Young (KTHNY) theory, that is, the melting of two-dimensional molecular solids in equilibrium conditions [30]. Interpreting the validity of such a classic equilibrium theory for a far-from-equilibrium system presents a challenge, and suggests new definitions for granular hydrodynamic or thermodynamic fields [31, 32].

Much knowledge has been gained on non-equilibrium phase transitions from granular studies. The low number of constituents of granular media, when compared to molecular fluids, provides a unique way of studying the role of noise in phase transitions [33, 34, 35]. It is known that fluctuations in macroscopic fields are proportional to the number of particles involved in the system, and thus the difference of noise intensity between molecular and granular systems is expected to be enormous. For example, only by including additive noise terms to the appropriate universal amplitude equations it has been possible to follow the growth and saturation of the relevant modes in pattern formation scenarios [34, 35]. It then becomes possible to establish an analogy with systems with the same amplitude equations, sometimes for quite different physical phenomena [36, 37]. The advantages that granular media offer, such as individual particle tracking and visible experiments, become an opportunity to understand the dynamics close to the transition for harder to visualize, e.g. molecular systems. The whole process is, in part, a classification

scheme that shows what is relevant and what is not in the critical dynamics of many transition scenarios. In this thesis we study fluctuations at the onset of a convective transition, and suggest a new interpretation of the transition based on the best suited amplitude equation.

1.4 VIBRATED GRANULAR MATERIALS

Granular flow depends on the existence of an external source of energy. A common way of keeping grains fluidized is by vibrating the container that holds them. Energy is thus injected through collisions with the grains and the moving walls, and dissipated by grain-grain collisions. A direct consequence of this is the creation of spatial inhomogeneities in the temperature field, which produces all sorts of non-equilibrium effects. This particular case of energy injection has in great part been favoured by its practical experimental implementation: electromagnetic shakers can be used to vibrate the container in a specified waveform and with accurate amplitude and frequencies. High-speed cameras are then commonly used to track the grains. Nevertheless, we wish to remark that the experimental setup does involve several complications, as the accumulation of static charges and the precise alignment of the container, among many others.

The plethora of phenomena present in vibrated granular systems is outstanding. Spontaneous phase-separation in vertically vibrated monolayers inspired a whole range of experiments, theory and simulations [30, 31, 38, 39, 40, 41, 42, 43]. Emerging patterns and localized structures yielded interesting relations with general dynamics based on the amplitude of the observed patterns [44, 29, 45, 46]. The correct explanation of the Brazil-nut effect, whereby particles which differ in size, mass or other properties migrate to the surface or bottom of a shaken container, continues to be a subject of debate, although a consensus on the involved effects seems to have been reached [47, 48, 49, 50, 51, 52]. When subject to horizontal vibrations, grains also present phase transitions [53], segregation [54] and pattern formation [28]. Sudden expansions, or sublimation-like phase transitions, are also observed either in initially crystalline configurations [55], or self-segregating ones [56]. Recently, standing waves and other patterns were observed in vibrated spheres filled with grains [57]. Overall, a wide range of complex phenomena has been reported, presenting both similarities and fundamental divergences from regular fluids. For general overviews we refer the reader to available reviews that treat the subject [29, 58, 59].

This thesis deals extensively with one specific geometry: a vertical quasi-two-dimensional (quasi-2D) box, whose height and length is much larger than its depth. Quasi-2D geometries are popular experimental setups, as most of the grains can then be easily visualized and tracked. When subject to vertical vibrations, grains inside the vertical quasi-2D container develop several distinct stable states. For low energy injections and a high enough number of particles, the granular bed bounces in sync with the vibrating box, and its behaviour is analogous to that of a single particle

bouncing on a moving plate [60, 61]. This occurs after the maximal acceleration of the bottom plate has exceeded the acceleration of gravity by a considerable amount, providing enough energy for the bed of grains to detach from the moving plate. As energy is increased, the bed goes through a period-doubling instability, eventually giving rise to a pattern [61, 62]. Depending on the amplitude, filling height, and particle factors, the granular bed can develop sub-harmonic surface-wave-like modulations, or spikes, both of which switch their peaks and valleys every two oscillation cycles [61, 63, 64, 65, 66]. The wavelength of such states roughly decreases as the energy is increased, and seems to depend heavily on dissipation, both due to the filling height and the restitution coefficient [64, 65, 66]. If, on the other hand, the number of particle layers is low, a gaseous state is found where particle motion is essentially uncorrelated [60].

For very high number of layers and low energy injections heaping can occur, whereas grains migrate to a specific sections of the container, forming one or several heaps of grains. Also in the high number limit but for higher energy injections, convection rolls are observed [67]. Convection or, more generally, average circulatory motion, seems to be present in almost all previously described states, although the driving factors and its dynamics change considerably [68]. We have ignored so far the role of air in the dynamics of the bed, which is known to be relevant [69]. Although a general quantification of the effects of interstitial air remains elusive [69, 70], they can be estimated from considering the relative importance of the forces exerted on the particles due to viscous drag (Stokes-type forces), and/or the forces from pressure gradients and the ensuing flow of air through the grains, a situation modelled by Darcy's law or relevant extensions [69]. In our study we consider the container to be in vacuum, as it significantly simplifies simulations. A non-exhaustive review of all these states can be found in [71]. In it, a density-inverted and a buoyancy driven convective state are described for even higher energy injections, both of which will be the focus of this thesis.

THE GRANULAR LEIDENFROST EFFECT

Experiments and simulations suggested that there were new behaviours to be seen in the narrow box beyond undulations, for even higher energy inputs [72, 73]. In the narrow box, it was observed that the modulated surface pattern is suddenly lost, and a density inverted state is reached [15]. In it, a gaseous, highly agitated region near the bottom boundary of the container sustains a solid or fluid-like upper region. This state was then referred to as granular Leidenfrost effect due to the analogous water-over-vapour phenomena [74]: if a droplet of water hits a surface with a sufficiently high temperature, it does not evaporate immediately, as a cushion of vapour is formed below it that prevents it from touching the plate. The moving plate in our system is analogous to the high temperature surface in the classical system. The molecular Leidenfrost effect continues to be an active area of research, partly due to

its many practical applications in industrial processes [75, 76, 77, 78].

Eshuis *et al.* carried further the experimental study of the granular Leidenfrost effect in a strictly 2D setup [79]. They confirmed that the appropriate order parameter to capture the transition was the dimensionless shaking strength $S \equiv a^2 \omega^2 / g d$, where a and ω are the amplitude and angular frequency of oscillation, d the particle size and g the acceleration of gravity. They were also able to obtain a matching density profile from a granular hydrodynamics model, considering the moving boundary as a temperature boundary condition, in analogy with [15]. In a subsequent study, carried out in a slightly deeper, quasi-2D setup, Eshuis *et al.* increased further the energy injection until the Leidenfrost state lost its stability and gave rise to a buoyancy driven convective state [71]. It was then shown that this transition can be captured by a linear stability analysis over a granular hydrodynamics model, with good agreement on the critical points for both experiments and simulations [80]. They took as initial stable state the vertical density profile, obtained from simulations and experiments, and studied its stability against a modulation of the hydrodynamic fields with a given wave number k_x . The critical wave number was found to coincide with the observed density profiles in simulations and experiments. Part of this thesis explores further the precursor states of the granular Leidenfrost to convection transition, and looks at the critical behaviour in the context of bifurcation theory, further deepening the understanding of this transition.

1.5 SIMULATION OF GRANULAR MATERIALS

Original research on granular materials was limited to phenomenological observations mainly by the experimental resources available [81]. The development of modern imaging techniques and the use of computers for data analysis at the middle of the previous century is certainly one of the factors that explains the explosion of granular research. Suddenly it became possible to observe and track the individual trajectory of grains in various different scenarios, providing a unique opportunity to link macroscopic behaviour with particular dynamics [82]. Another determinant factor for the growing interest on granular media was the rise of computer simulations, which from the start could correctly reproduce and predict many behaviours, permitting an until then impossibly detailed analysis of their structure and dynamics. If, as history hints, scientific revolutions are associated with technical advancements, then the science of granular matter is in great measure part of the computing revolution that took place in the second half of the past century.

Algorithms that simulate the motion of a collection of particles are usually referred to as particle simulations. There are many different methods, with different ranges of applicability and validity [83, 84]. The most widely used one consists of a straightforward solution of the equations of motion: given the total force acting on each particle, Newton's second law is integrated in time. Time is advanced in small enough time-steps so as to resolve with good enough resolution the duration of the

contacts. After moving the particles accordingly, forces are recomputed, and the process is repeated. These types of implementations are referred to as discrete particle methods (DPM). Critical optimizations can be done in the computation of the total force acting on each particle by dividing the system in cells and using appropriate data structures [85]. This method has proven accurate in a number of physical cases, and is now widely used for both academic and industrial purposes.

EVENT-DRIVEN ALGORITHM

In this thesis we use the event driven (ED) discrete particle method [86, 87, 88]. The fundamental difference between an ED and plain DPM algorithms lies in the handling of the time evolution: ED does not possess a fixed time step, as DPM simulations, but a variable one, given always by the next event. An event is either the collision of two particles, or the collision of one particle with a boundary. ED simulations are usually orders of magnitude faster than their plain DPM equivalents, as collisions are resolved in a lower number of computational steps, and the undisturbed free-flight motion of the particles is not computed. Nonetheless, it is important to remark that the ED algorithm is not easily parallelized [88], with the computational gain as a function of the particles number (N) being less than optimal, at most proportional to \sqrt{N} . This is a highly relevant aspect for today's overall computing efficiency.

The simplified model of collisions used in event-driven simulations allows for a much faster treatment of collisions than plain DPM simulations. Velocities are updated instantly, according to rules based on momentum conservation and energy balance. For two smooth spheres of radius a , and masses m_1 and m_2 , the post-collisional velocities \vec{v}' in their centre of mass reference frame are given, in terms of the pre-collisional velocities \vec{v} , by

$$\vec{v}'_{1,2} = \vec{v}_{1,2} \mp (1+r)\vec{v}_n/2, \quad (1.1)$$

with $\vec{v}_n \equiv [(\vec{v}_1 - \vec{v}_2) \cdot \vec{n}] \vec{n}$, the normal component of the relative velocity $\vec{v}_1 - \vec{v}_2$, parallel to \vec{n} , the unit vector pointing along the line connecting the centres of the colliding particles from 2 to 1. The restitution coefficient, $r \in [0, 1]$, is a measure of the level of inelasticity in every collision, with $r = 1$ corresponding to the elastic case. Most of the results of this thesis will depend heavily on r , especially when comparing with hydrodynamic theories, which are valid in different regions of r . Roughly speaking, higher dissipations lead to more strongly correlated dynamics, and thus are harder to model by continuum theories. This simple collision model is used extensively throughout this thesis, and serves as the starting point for more involved ones. Rough hard-spheres that include rotational degrees of freedom are also considered, as friction is known to play a determinant role in many phenomena [89, 17].

Once the collision rule has been specified, the algorithm is then completely defined. The main cycle consists of, first, the determination of the most immediate

event from the set of all possible future events. Specific computations are performed for each type of event; in the case of a collision, the velocities of the particles are properly updated. Events can also be any other physical or not physically relevant action, including measurement routines. The last step consists in advancing time and updating the system accordingly, after which the whole process is repeated. ED simulations are thus extremely efficient when the time of the upcoming events can be analytically and easily computed. This is the case for particles subject to constant and homogeneous external fields (usually gravity) and step-wise constant interaction potentials. In this scenario the solution for the time of collision between two particles is actually given just by the intersection of their relative linear trajectories. Walls, on the other hand, involve the solution of quadratic equations. Nevertheless, let us remark that although analytic determination of the collision times highly simplifies the algorithm, the possibility of numerically solving the intersection of the equations of motion is also possible [90].

One clever source of optimization involves the updating process after a collision. Classic ED algorithms updated the whole system after each event, a method which is straightforward but inefficient for large numbers of particles. Modern ED algorithms assign a local time to every particle, and only update the events in which the two particles involved in the last collision participate [86], as the rest of the predicted events will be unmodified. This so called “asynchronous” algorithm saves time by not having to cycle and update the position of every particle in the system after every event, an expensive routine for large numbers of particles.

The critical optimization point for serial ED algorithms is in the determination of the forthcoming collision times. The introduction of cells, which define virtual boundaries, greatly increases the efficiency of this process. Virtual boundary collisions have no effect on the particles motion, but are only introduced to keep track of which particles belong to which cell. If the particles in a given cell and its neighbours are known, then the search for possible collision partners can be done locally, greatly reducing the time for the determination of the next collision for any given particle.

The process can be further optimized using appropriate data structures. The times which indicate the next event for a certain particle are stored in an ordered heap tree, such that the next event is found at the top of the heap with a computational effort of $O(1)$. Changing the position of one particle in the tree from the top to a new position needs $O(\log N)$ operations. In total, optimizations yield a numerical effort of $O(N \log N)$ for N particles. For a more detailed description of the algorithm we refer the interested reader to [86].

Using all these optimizations it is possible to simulate the evolution of 10^6 particles within reasonable time on a normal desktop computer [91]. Throughout this thesis we will be interested in long transient behaviour, especially when studying dynamics near transitions. Moreover, as we have seen, some of the states involved in our study require high energy inputs, which translate into very high frequen-

cies of oscillation of the container. In order to resolve these oscillations, plain DPM methods would have to adjust their time-step to be a fraction of the oscillation period, which together with the expected long transient behaviours render the use of such methods infeasible. As an example, the longest simulations in our studies took around two months of continuous computation; considering that DPM methods were seen to be anywhere between one to two orders of magnitude slower, ED simulations clearly emerged as the most practical alternative.

HARD-SPHERE MODEL

Physical collisions between particles are a very hard problem to model, as they involve the inner structure of individual grains, and surface impurities are also known to play an important role [92, 93, 94, 95]. Simplistic models are usually preferred, as in collisional many-particle systems the details of the interactions are usually averaged out, and thus irrelevant. The most straightforward simplification consists of impenetrable, infinitely hard particles. In the following work we will only consider the hard-sphere model of particles, in the spirit of simplicity and generality of results. Furthermore, as we mostly consider highly agitated systems, the specific interaction between particles or higher order effects, as ternary contacts, are expected to become negligible.

It could be argued that the hard-sphere model does not capture the physical behaviour of particle-particle collisions. Collisions are known to take a finite time, involve deformation of the particles [96], be affected by attractive interactions [97], as well as other factors, all of which are not captured in the hard-sphere limit. The choice of this model is based on the observation that dense matter properties are to first order determined by the impenetrability of its constituents. In abstract terms, it is the arrangement of non-overlapping spheres in three-dimensional space that dominates the properties of dense materials. The study of what properties can and cannot be captured by considering only packings of hard-spheres is important, even if overly simplistic, as it allows the determination of which are the relevant factors on any phenomena that arises when using more elaborate constituent models. It is somehow a reductionist argument: only by studying the simple limits are you able to properly identify the causes in more complex models. Knowledge has been gained on a wide range of physical systems by using hard-sphere models, such as colloids [98], glasses [99, 100], liquids [101], and of course granular materials [102, 103, 104], among others [105, 106]. The model is surprisingly successful in reproducing several phenomena of condensed matter physics, such as the crystallization or melting of liquids [107, 108], decompaction of grain piles [103, 109], and amorphous-to-crystal phase transitions [110].

1.6 THESIS OUTLINE

The thesis is organized into six sections. Overall, we follow a path of increasing energy injection and effective dimensionality, from the Leidenfrost state in quasi-one-dimensional (quasi-1D) geometries to the transition to convective states in wide, quasi-2D geometries. Moreover, as the thesis progresses the emphasis roughly goes from phenomenological descriptions to continuum modelling of the studied phenomena. General conclusions and an outlook of future work are presented at the end.

Chapter 2 describes the collective oscillations observed in vertically vibrated, density inverted granular beds. We call these oscillations low-frequency oscillations (LFOs), as their characteristic period is much larger than the period of oscillation of the container. Chapter 3 delves deeper into the nature of LFOs, presenting an experimental observation of the phenomena by using the Positron Emission Particle Tracking (PEPT) technique. We also report two observed convective phenomena in similar setup configurations which resist an interpretation by previously known results. In Chapter 4 we do a simulational study of the transition from the granular Leidenfrost to the buoyancy-driven convective state. We characterize both density and velocity fluctuations of the precursor state and interpret their behaviour in the context of bifurcation and criticality theories. Fluctuations are studied in a more general aspect in Chapter 5, as a function of the total number of particles involved in a granular system. A definition is given of hydrodynamically equivalent systems, and a scaling is found for the steady-state and no-flux conditions in the granular Leidenfrost state which leaves the equations invariant. The last section, Chapter 6, studies the possibility of describing the granular Leidenfrost state and its transition to buoyancy-driven convection using granular hydrodynamic models. The equations are numerically solved under different physical approximations, and then compared to particle simulations in order to analyse the deviations and understand the relevant physical factors. Finally, general conclusions are presented in Chapter 7, followed by brief discussions about possible future work.

LOW-FREQUENCY OSCILLATIONS IN NARROW VIBRATED GRANULAR SYSTEMS¹

In the following chapter simulations and a theoretical treatment of vertically vibrated granular media are presented. The systems considered are confined in narrow quasi-two-dimensional (quasi-2D) and quasi-one-dimensional (column) geometries, where the vertical extension of the container is much larger than both horizontal lengths. The additional geometric constraint present in the column setup frustrates the buoyancy-driven convective state observed in wider geometries. This makes it possible to clearly recognize collective oscillations of the grains with a characteristic frequency that is much lower than the frequency of energy injection. The frequency and amplitude of these oscillations are studied as a function of the energy input parameters and the size of the container. We observe that, in the quasi-2D setup, low-frequency oscillations are present even in the convective regime. Two models are also presented; the first one, based on Cauchy's equations for continuum media, is able to predict with high accuracy the frequency of the particles' collective motion. This first principles model depends on a first order approximation of the vertical density profile, and shows that a sufficient condition for the existence of the low-frequency mode is an inverted density profile with distinct low and high density regions, a condition that may also apply to other systems. The second, simpler model just assumes an harmonic oscillator like behaviour and, using thermodynamic arguments, is also able to reproduce the observed frequencies with high accuracy.

1. With minor corrections, from: N. Rivas, S. Luding, A.R. Thornton, New Journal of Physics 15 (11), 113043, 2013.

2.1 INTRODUCTION

Vibrated beds of granular materials present a wide range of different behaviours: phase separation [38, 40], Faraday-like pattern formation instabilities [111, 64], heap formation and convection [112, 113], segregation [114, 59], clustering [91] and periodic cluster expansions [56], among many others. These systems generally present a remarkable collection of distinct nonequilibrium inhomogeneous stable states for relatively small changes in the energy injection parameters. Hence, they are specially suited for the study of nonequilibrium phase transitions, as well as non-linear phenomena in general. Careful analysis of the microscopic mechanics behind the different transitions improves the comprehension of the complex dynamics present in driven granular systems. This gives further insight into when, and until what point, granular media behave like classical gases, fluids or solids, or whether they require an altogether different theoretical approach.

As can be seen in the aforementioned studies, the geometry of the system plays a fundamental role in determining the phenomena. Just by reducing the effective dimensionality of the system it becomes possible to observe behaviour not easily identifiable in fully three dimensional systems. The natural approach of study is then confining the grains to quasi-two-dimensional (quasi-2D) systems, where also particle-tracking methods become possible. Our study is inspired by one specific quasi-2D geometry that presents several distinct states in the energy injection parameter space: a vertical narrow box. That is, we focus on a vertically vibrated Hele-Shaw cell with the walls parallel to gravity, inside which the grains are located. The first reported classification of the different states present in this geometry was realised by Thomas et al. [60], in what would now be considered the low energy injection limit. Research then focused on the wave-like dynamics of the granular bed, and its variations with the frequency and the amplitude of oscillation [61, 63]. It was with simulations that the energy input was considerably increased, and the existence of a density inverted state was first reported [15]. This state, named Leidenfrost after the analogous water-over-vapour phenomena [115], was then experimentally studied in depth by Eshuis et al. [79, 71], as well as the buoyancy driven convection regime that is observed for higher energy inputs.

In the following simulational study the dimensionality of the vertical, narrow box is progressively reduced until both the width and depth are only five particle diameters wide, making the system effectively quasi-1D (see Figure 2.1). More precisely, at this limit there are no significant macroscopic inhomogeneities of any hydrodynamic field in the horizontal directions. We refer to this setup as the granular column. The first direct consequence of this further confinement is the frustration of the horizontally inhomogeneous states present in the wider geometries. Particularly, the suppression of convection makes it possible to directly observe the grains collectively oscillating at a much lower frequency than the energy injection frequency. Appropriately, we call these oscillations *low-frequency oscillations* (LFOs). Effective

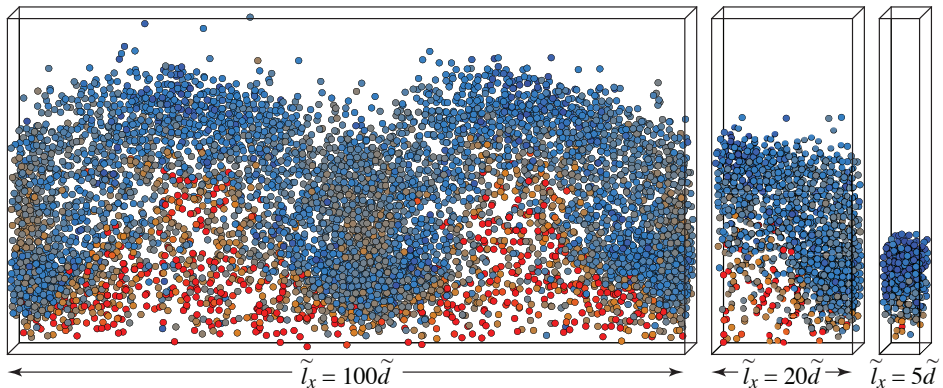


Figure 2.1: Snapshots of three vertical and narrow containers with the same number of filling layers $F = N\tilde{d}^2/\tilde{l}_x\tilde{l}_y = 12$, with N the total number of particles, \tilde{d} the (dimensional) diameter of the spherical particles, and \tilde{l}_x and $\tilde{l}_y = 5\tilde{d}$ the (dimensional) width and depth of the container, respectively; and energy injection parameters, but different widths \tilde{l}_x . From left to right, $\tilde{l}_x = 100\tilde{d}$, $\tilde{l}_x = 20\tilde{d}$, and $\tilde{l}_x = 5\tilde{d}$. The rightmost corresponds to the *column* geometry. Particles are coloured according to their kinetic energy, with red for higher energies.

frequencies and amplitudes are defined and studied in the container length and energy injection parameter space. We then argue that LFOs are an essential feature of the dynamics of the narrow vibrated geometry, but it is only in the quasi-1D column setup that they can be easily isolated from the other collective grain movement of convection. Simulational measurements confirm this, as well as a continuum description of the system, which captures the correct frequency response for high energy inputs. The frequency behaviour is actually analogous to a forced harmonic oscillator, and is obtained mainly by considering a vibrated media with a high density region suspended over a low density one. This density inverted situation is indeed present, to different extents, in both the Leidenfrost and the convective regimes.

2.2 SIMULATIONS

Simulations are performed using an event-driven molecular dynamics algorithm [86]. In this approach, particles move freely under the effect of gravity until an event take place, namely, a collision with another particle or a wall. The motion of the particles in between successive events does not have to be simulated: if their trajectory equation is known, time can be advanced in variable steps. This makes event-driven simulations considerably faster than usual soft-particle simulations, where time is advanced at constant steps, independent of particle interactions. However, the need of having an analytical expression for the particle motion is a strong condition that

limits the possible interaction between particles. In the following, we consider the most common approach: perfect hard-spheres, which imply binary collisions and no overlap or long-range forces between particles. This is a first order approximation of real particle-particle collisions, which is known to be a fairly complex phenomena dependent on shape, surface roughness, ambient conditions, as many other factors. It captures, nevertheless, the dominant effects of the simple geometrical constraint of no significant overlap between particles. In our case, dissipation is modeled by a set of four parameters, normal and tangential restitution coefficients, $\epsilon_n = \epsilon_t = 0.95$, as also static and dynamic friction coefficients, $\mu_s = \mu_d = 0.1$ [116]. The tangential restitution and friction coefficients model the coupling of linear and rotational degrees of freedom, ϵ_t setting the threshold for either sliding or sticking behaviours. The explicit form of the collision law is given in the Appendix. These particular values are known to reproduce complex behaviour observed in similar vibrated setups using stainless-steel spheres of $\tilde{d} = 1$ mm to $\tilde{d} = 5$ mm in diameter [56, 42], and where picked based on previous experimental measurements [117]. In order to avoid inelastic collapse we use the TC model [87], with a constant value $t_c = 10^{-6}(\tilde{d}/\tilde{g})^{1/2}$, with \tilde{d} the (dimensional) diameter of the spheres, and \tilde{g} the (dimensional) gravity. (In the following, quantities without a tilde are dimensionless). That is, collisions between two entities are considered elastic if they occur more frequent than 10^{-6} gravity timescale units.

The setup consists of an infinitely tall container of width \tilde{l}_x and depth \tilde{l}_y inside which the grains can move. The boundaries of the container are considered solid, and have the same collision parameters as particle-particle collisions. The whole box (both the bottom and the side walls) is vertically vibrated in a bi-parabolic, quasi-sinusoidal way with a given frequency $\tilde{\omega}_f$ and amplitude \tilde{A}_f , given by:

$$z = \begin{cases} \frac{8\tilde{A}_f}{\tilde{T}_f^2} (2t - \tilde{T}_f)t & 0 \leq t < \frac{\tilde{T}_f}{2} \\ \frac{8\tilde{A}_f}{\tilde{T}_f^2} (2t - \tilde{T}_f)(\tilde{T}_f - t) & \frac{\tilde{T}_f}{2} \leq t < \tilde{T}_f \end{cases}$$

with $\tilde{T}_f \equiv 2\pi/\tilde{\omega}_f$. The use of a quadratic instead of a sine function gives a considerable speed advantage in simulations, as the prediction of collision times with the moving walls becomes substantially faster. Test simulations were performed using a sine function for exemplary cases, and no significant differences were observed [118]. Furthermore, we considerably varied the collision parameters and found the essential phenomena to be robust. Friction was observed to be relevant, mostly by triggering convective flows near the side-walls for lower energy injections than without friction, as a consequence of the increased inhomogeneity of energy dissipation. The relation is nevertheless not straightforward, as increasing friction also increases the overall bulk dissipation, which is expected to rise the energy needed to obtain steady convective flows. Eliminating friction completely quantitatively modifies the phase space, but all studied states were still observed. We remark that

the role of friction and dissipation in analogous experiments is a matter of ongoing research [119].

We now introduce dimensionless variables, which will be used for the rest of the text. The depth of the box is fixed, $l_y \equiv \tilde{l}_y/\tilde{d} = 5$, and the horizontal width $l_x \equiv \tilde{l}_x/\tilde{d}$ is varied in the $[5, 100]$ region. N is always taken so that the number of filling layers $F \equiv N\tilde{d}^2/\tilde{l}_x\tilde{l}_y = N/l_x l_y = 12$, which implies that N varies in the $[300, 6000]$ range. Three different oscillation amplitudes are considered, $A_f \equiv \tilde{A}_f/\tilde{d} \in \{0.4, 1.0, 4.0\}$. This allows us to compare with previous results, obtained for $A_f = 4.0$, as also to extrapolate to lower amplitudes, where the vibrating bottom wall can be considered as a spatially fixed source of energy (i.e. a temperature boundary condition).

The dimensionless gravity timescale is given by $t_g \equiv \tilde{t}/\tilde{t}_g$, with $\tilde{t}_g \equiv (\tilde{d}/\tilde{g})^{1/2}$. Correspondingly, the dimensionless oscillation frequency ω_f is scaled as $\omega_f \equiv \tilde{\omega}_f\tilde{t}_g = \tilde{\omega}_f(\tilde{d}/\tilde{g})^{1/2}$. Nevertheless, it is almost always more meaningful to measure time in periods of box oscillations, $\tilde{T} = 2\pi/\tilde{\omega}_f$, and thus we use $t \equiv \tilde{t}/\tilde{T}$. In order to compare simulations with different energy injection parameters the dimensionless shaking strength is used, $S \equiv \tilde{A}_f^2\tilde{\omega}_f^2/\tilde{g}\tilde{d} = A_f^2\omega_f^2$. Finally, the mass scale $m = \tilde{m}/\tilde{m}_p$ is set to unity by taking \tilde{m} as the mass of one particle, $\tilde{m} = \tilde{m}_p$.

Simulations are generally run for $10^5 T = 10^5(2\pi/\omega_f)$, unless otherwise stated. Particles are initially arranged in a low density hexagonal crystalline packing, with significant perturbations on the positions with regard to the perfect crystal and randomized initial velocities, in order to avoid any relevant correlation. We confirmed that this initial configuration has no influence on the steady dynamics by running a few simulations using the end state of the previous simulation as the initial configuration. Contrary to the experiments realised in [71], where the frequency of shaking is continuously increased, the energy injection parameters are kept fixed during any given simulation.

PHASE SPACE

In order to validate our simulations, and explore further previous research, we first focus on the $A_f = 4.0$ case, where the comparison with previous experiments and soft-particle simulations undertaken by Eshuis et al. [71] is straightforward. Event-driven simulations are able to reproduce all previously observed states, as can be seen in the phase diagram in the $\{l_x, S\}$ space presented in Figure 2.2. Furthermore, a quantitative comparison is possible by looking at the transition points in the $l_x = 100$ case, where the experiments were realised. There is excellent quantitative agreement, within 5%, for the bouncing bed-undulations and the Leidenfrost-convection transition points, but a 30% error in the undulations-Leidenfrost one. The deviations could in part be explained by the nature of the transitions, as they are not sharp and are seen to present wide ranges of metastability. This makes it harder to define a precise transition point value, and motivates the use of transition regions, which we show in gray.

As can be seen from Figure 2.2, for $l_x > 20$, and as S is increased (keeping $A_f = 4.0$), the system goes through a sequence of different non-equilibrium stable states: bouncing bed, bursts, undulations, Leidenfrost, convection and gaseous ($S > 400$, not shown). Some of these states disappear or appear as l_x and A_f are varied, but their relative order remains. Our study is focused on the Leidenfrost and convective states, where LFOs take place; nevertheless, in what follows a brief description of the other states is given.

The bouncing bed state originates when the maximum acceleration of the moving box is high enough for the bed of grains to detach from the bottom and go through a period of gravity driven free-flight. The granular bed slightly expands during this period, until it collides again with the moving bottom plate, compresses, and moves together with the box, completing the cycle at the next detachment point. That is, the dynamics of the whole bed is analogous to that of a solid with coefficient of restitution zero [60]. The sudden loss of energy due to the impact with the bottom wall has been referred to as granular damping [120]. In this state, the movement of most of the particles is directly coupled with the box oscillation, and no horizontal inhomogeneity is observed beyond the expected fluctuations.

As S is increased, the bouncing bed state becomes unstable to periodic perturbations in the horizontal direction, leading to the bursts and undulations states. In these states high density regions expand and collapse every one or two oscillation cycles, alternating between valleys and peaks at fixed positions. These standing wave patterns oscillate at twice the shaking period, and are therefore usually referred to as $f/2$ waves [71]. In both cases the phenomena is produced by shock-waves triggered by the sudden dilation of the bed as it hits the moving bottom boundary. High density regions expand and propagate until they collide with another shock-wave going in opposite direction. The main difference between the two states is the phase at which the high density regions impact the moving bottom, which leads to distinct pattern shapes. Undulations present overall less density inhomogeneities in the horizontal direction, while for bursts the contrast is higher, producing stronger shock-waves and thus sharper peaks.

Increasing the energy input further leads to a density inverted, horizontally homogeneous state referred to as granular *Leidenfrost* state. Its name comes from the analogous liquid-over-vapour phenomena, where a thin layer of vapour over a hot surface significantly slows the evaporation of the droplet above it, by keeping it floating over the hot surface [74]. Figure 2.3 shows the packing fraction ϕ and the granular temperature T_g as a function of z , for different amplitudes and frequencies of oscillation, all in the Leidenfrost state. The granular temperature is defined as twice the fluctuating kinetic energy per degree of freedom: $T_g = \frac{2}{3} \sum_i (\vec{v}_i - \vec{V}(r_i))^2$, where r_i is the position of particle i , v_i its velocity, and V the average velocity field. Indeed, a low temperature, high density region is suspended over a low density, high temperature one. Notice that the difference in density between the solid and gaseous regions is greater for higher ω_f (blue vs. red), but lower for higher A_f (solid

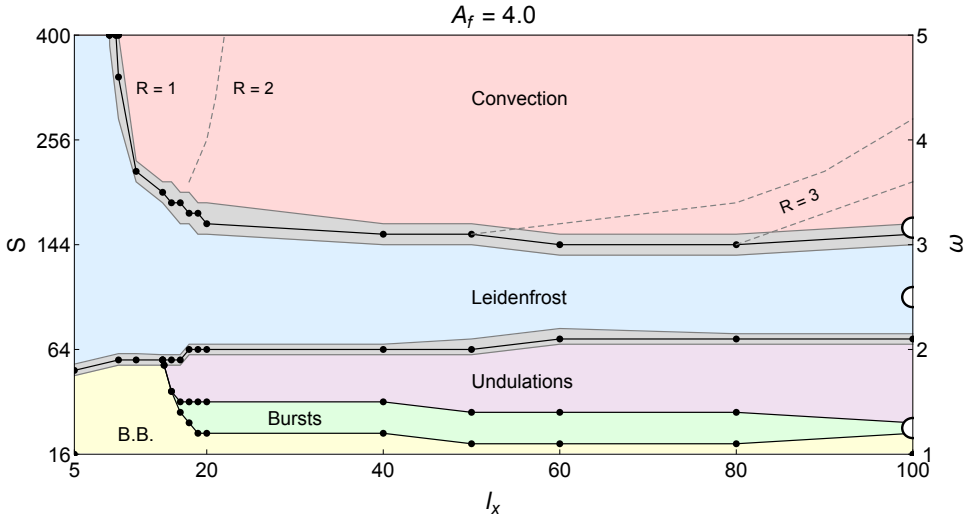


Figure 2.2: Phase diagram of the vertically vibrated system in the dimensionless container width (l_x) and shaking strength (S) space, for fixed box oscillation amplitude $A_f = 4.0$. The equivalent box oscillation frequency (ω_f) is shown on the right axis. All previously reported states are seen: bouncing bed (b.b, yellow), bursts (green), undulations (purple), Leidenfrost (blue) and convection (red). Transition regions are shown in gray, and are defined by the regions of bistability of every pair of states. Transition points from previous experimental work are shown as white dots for $l_x = 100$. The borders between different numbers of convective rolls ($R = 1, 2, 3$ and 4) is also delimited (dashed lines).

vs. dashed): these features will be relevant in our model discussion for the validity regions of a density profile approximation.

When S is further increased, the density of the solid region is seen to progressively decrease, leading to a buoyancy driven convective state (see Figure 2.1). Horizontal homogeneity is lost, leading to low density regions where particles go up and circulate around high density regions, where particles agglomerate and move mainly in the horizontal directions, towards the low density regions. The number of convection rolls (R) diminishes with increasing ω_f , until the energy input is so high that particle motion is essentially uncorrelated and the system enters the gaseous state ($S > 400$, data not shown).

We now turn our attention to the lower amplitude regions. Figure 2.4 shows a phase diagram again in the $\{l_x, S\}$ parameter space, for different shaking amplitudes A_f . As observed previously [71], and confirmed here for a wider range of parameters, the dimensionless shaking strength S is a better parameter than the dimensionless acceleration, $\Gamma \equiv \tilde{A}_f \omega_f^2 / \tilde{g} = A_f \omega_f^2$ for the characterisation of the Leidenfrost-convection transition. On the other hand, the transition points of bouncing bed-Leidenfrost (or undulations-Leidenfrost for $A_f = 4.0$) vary significantly with S , but

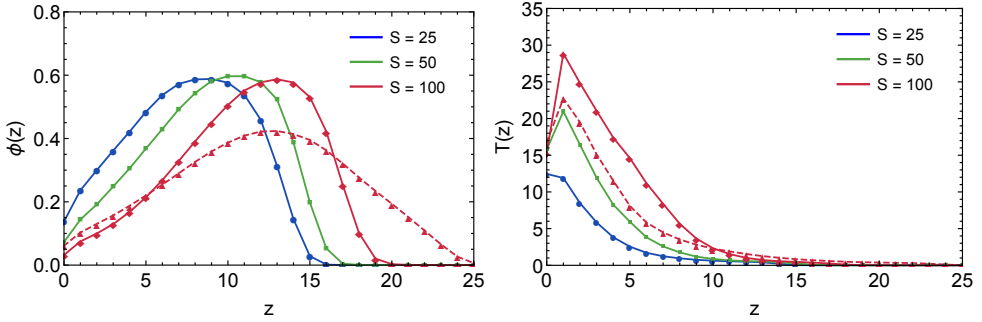


Figure 2.3: Packing fraction ϕ (left) and granular temperature T_g (right) vertical profiles, for the exemplary frequencies shown in the inset, and $l_x = 50$, for $A_f = 1.0$ (solid) and $A_f = 4.0$ (dashed). All cases are in the Leidenfrost state.

stay within 5% when compared in Γ . In general terms, the most significant influence of reducing A_f is the disappearance of the bursts and undulations states; the large amplitude of the box oscillation plays a dominant role in the dynamics of these states.

We briefly remark that simulations were done until $l_x = 400$, and no new states were observed, except for the coexistence of convection and Leidenfrost states for $l_x \geq 200$. The possibility of this coexistence provides new insight into the nature of the Leidenfrost-convection transition; further details are given in Chapter 4.

If the length is reduced further, below the $l_x = 20$ limit, the frequency needed to trigger convection progressively increases, until at $l_x \sim 10$ (a value slightly dependent on A_f , see Figure 2.4) no convection was observed even for $S = 10^4$. For $A_f = 4.0$, undulations and bursts are also frustrated by the small size of the container. It is in this geometry that it becomes possible to observe the Leidenfrost state for higher S , where low-frequency oscillations (LFOs) can be directly observed and eventually, as S is increased, dominate the collective dynamics of the system.

LOW-FREQUENCY OSCILLATIONS (LFOs)

Finally, we reach the column limit, where $l_x = l_y = 5$. In order to study LFOs the evolution of the vertical centre of mass of the particles is considered, $z_{cm}(t)$. Figure 2.5a shows $z_{cm}(t)$ for fixed $A_f = 1.0$ and several different S . For comparison, non-stroboscopical and stroboscopical $z_{cm}(t)$ are shown for the $S = 64$ and $S = 400$ cases: the distinct high and low frequencies become immediately recognisable. The amplitude of the oscillations is seen to increase from the $\Delta z_{cm} \approx 1$ to the $\Delta z_{cm} \approx 10$ order, and present an appreciable regularity in time. While at $S = 64$ both oscillations are comparable in amplitude, and thus very hard to identify from direct observation, at $S = 400$ they have become clearly differentiable. Although LFOs are seen to be

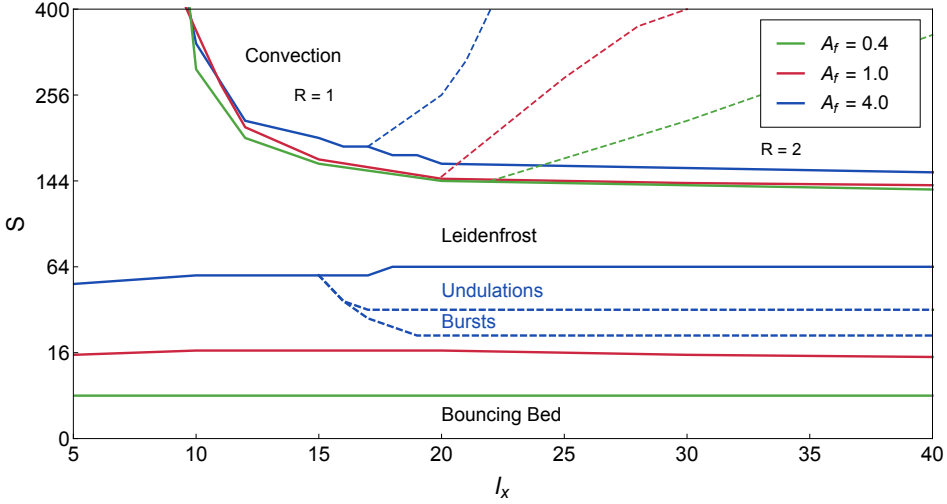


Figure 2.4: Phase diagram of the vertically vibrated narrow box in the shaking strength (S) and container width (l_x) space, for different oscillation amplitudes, as shown in the legend.

fairly chaotic (recall that there are only 300 particles in the column geometry, hence fluctuations play a leading role), we characterise them by a constant amplitude A_0 and a single frequency ω_0 , as an initial first order description.

First, let us focus on the frequency of the LFOs, ω_0 , which is clearly recognisable from the power spectra of $z_{cm}(t)$, presented in Figure 2.5b. The spectra are obtained by taking the discrete fast Fourier transform of $z_{cm}(t)$ over $20000T$ after an initial transient of $1000T$, with a sampling rate of $0.05T$. An average is then taken over 10 simulations with identical parameters but different initial conditions; although the shape and peaks are already recognisable from single simulations, the ensemble averaging reduces the noise considerably. The time window, the sampling rate and the transient time were varied and no significant differences were observed.

All spectra present two main features: the expected delta-like peak at ω_f and its harmonics, and a broad peak one to two orders of magnitude lower, corresponding to the LFOs. The LFO frequency, ω_0 , is defined as the frequency of the maximum of this broad peak. After observing the different spectra it becomes evident that ω_0 depends on the energy injection parameters. Figure 2.6a shows $\omega_0(S)$ for different l_x and A_f , remarkably scaling all LFO data. Notice that ω_0 decreases as S increases, i.e., the collective grain movement becomes slower as the shaking gets faster. The decay is faster than inverse linear, and can be fitted by a $-\frac{1}{3}$ power with a 5% error (not shown). Let us also notice that the length of the container makes no discernible difference, as long as the system stays in the Leidenfrost state; the decreased data in the $l_x = 20$ case are due to the Leidenfrost-convection transition. The collapse of the

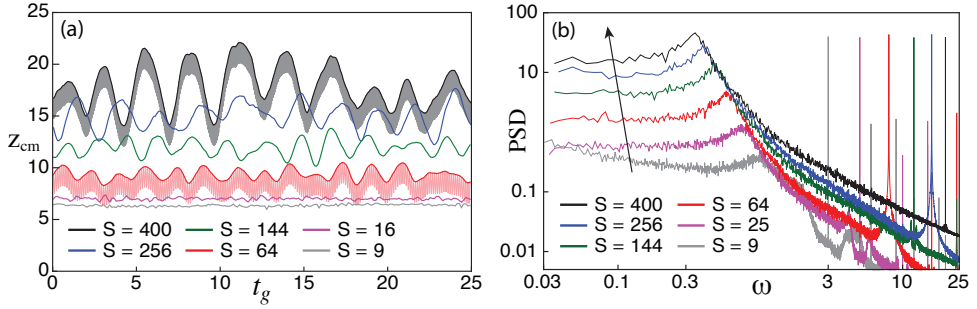


Figure 2.5: (a) Centre of mass evolution, $z_{cm}(t)$, for $A_f = 1.0$ and different dimensionless shaking strengths $S = \omega_f^2$, as a function of time in gravity timescale units $t_g = \tilde{t}(\tilde{g}/\tilde{d})^{1/2}$. The light colour data are taken with sub-period resolution, while dark colour data are taken every oscillation cycle at the point of maximum wall amplitude. (b) Fast Fourier transform of the centre of mass of the particles, $z_{cm}(t)$, for $A_f = 1.0$ and several different S . The arrow indicates the direction of increasing S . Different amplitudes, not shown, present the same qualitative behaviour.

different amplitude curves is very good for $A_f = 0.4$ and $A_f = 1.0$, while for $A_f = 4.0$ data slightly deviates. We interpret this decrease as the influence of the undulations state in the Leidenfrost regime; notice that for $S \sim 64$ and $A_f = 4.0$ the system is almost at the boundary between both states (see Figure 2.2).

In order to quantify the relevance of the LFOs, we define the relative intensity of the ω_0 peak, I_0 , as the normalised distance from the low frequencies asymptotic limit to the maximum of the broad peak. Figure 2.6b shows $I_0(S)$ for different l_x and A_f . Although the dependency is not straightforward, it can be seen that LFOs become increasingly distinguishable from other movements until $S \sim 144$, after which there is a decline, except for the highest amplitude case. Already at $S = 25$ oscillations should be discernible in the spectra as a peak twice as big as the low-frequency asymptotic limit. A_f is seen to have a pronounced effect on I_0 ; higher amplitudes of oscillation lead to more pronounced LFO peaks.

Finally, we define the amplitude of the LFOs, A_0 , as the standard deviation of $z_{cm}(t)$: $A_0 \equiv \sigma(z_{cm}(t))$. Data is considered only after $t = 1000$, to disregard transient states. Figure 2.6c shows $A_0(S)$ increasing in an almost linear way. The curves coincide, within their error, for $A_f = 0.4$ and $A_f = 1.0$, while for all other cases A_0 is consistently smaller. Nevertheless, S makes all curves comparable, further confirming its relevance for this system.

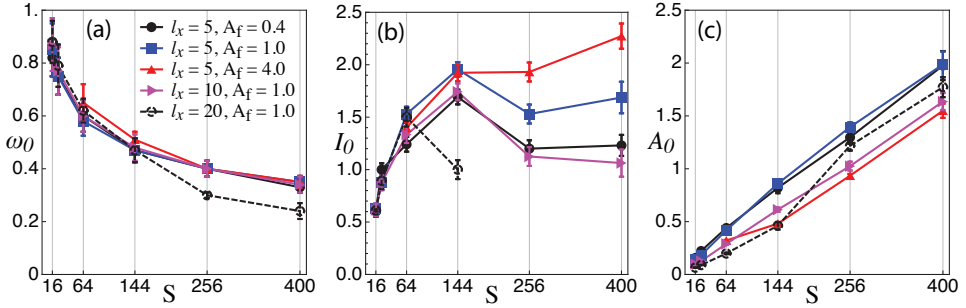


Figure 2.6: (a) LFO frequencies, ω_0 , as a function of S , for different container lengths l_x , and shaking amplitudes A_f , as given in the inset. (b) Intensity of ω_0 , I_0 , defined as the height from the asymptotic low-frequencies value of the $z_{cm}(t)$ spectra to the broad peak, for the same data as (a). (c) Amplitude of the LFOs, defined as the standard deviation of $z_{cm}(t)$, as a function of S , for the same data as (a).

LFO'S IN CONVECTIVE STATE

We now consider in detail the peculiar change of behaviour of $\omega_0(S)$ and $A_0(S)$ for $S \sim 144$ in the $l_x = 20$ case. This is a sign of the Leidenfrost-convection transition, still present at this container length (see Figure 2.2). During convection, z_{cm} becomes a less relevant quantity, as there is no longer horizontal homogeneity. Nevertheless it is still possible to identify LFOs, even if the oscillations are entangled with the convective flow. The presence of LFOs in the convective regime should not be surprising if one notices that it also presents the essential feature of the Leidenfrost state: a high density, low temperature region suspended over a low density, highly agitated one, although there is an additional low density, highly convective zone above. Our model, derived in Section 3 below, suggests that when density inversion is present, LFOs exist. Figure 2.7 presents several different fields and snapshots that show that, indeed, density inversion is present in the convective regime, in addition to the horizontal inhomogeneity. All data is taken from the same simulation, and fields are time-averaged over $100T$ after an initial transient of $1000T$, with data taken every $0.05T$. The average velocity field, Figure 2.7a, clearly shows the presence of convective flow, with a small downwards band and a wider upwards region. Particles agglomerate at the bottom of the downwards flux side, as can be seen from the average density field (Figure 2.7b), and the two snapshots (Figures 2.7d and 2.7e). This happens when downwards and upwards particles collide, leading to a high granular temperature region (Figure 2.7c). Note, then, that both sides correspond to low density, high temperature regions sustaining high density, lower temperature ones, although the density and temperature profiles vary considerably from left to right. The profile is more similar to the Leidenfrost case in the upwards flow region (left in the shown figures), as in the downwards flow region the high density area presents

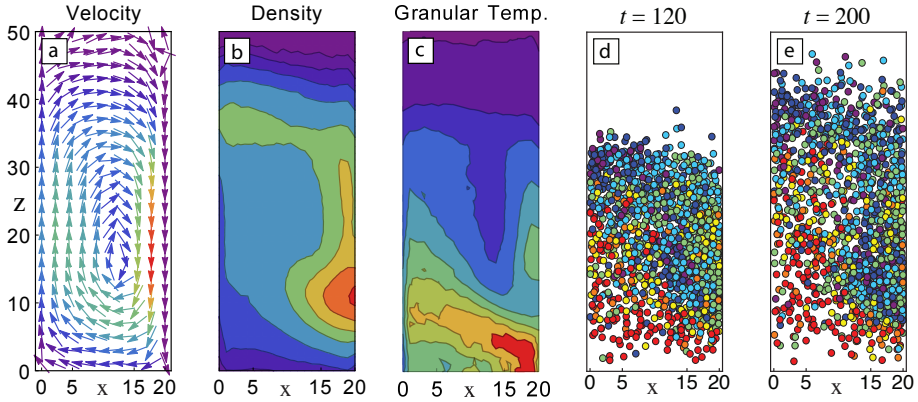


Figure 2.7: (a) Averaged velocity field of an $l_x = 20$ system in the convective state, for $A_f = 1.0$ and $S = 144$ ($\omega_f = 12$). The colour of the arrows corresponds to the average speed, increasing from blue, green, yellow, until red. (b) Average density field of the system in (a). Colour scale from blue (low densities) to red (high densities). (c) Average granular temperature field, as defined in main text. (d, e) Two snapshots of the system taken at the minimum (d) and maximum (e) of a low-frequency oscillation. Colour corresponds to the particles kinetic energy.

a comparable, although lower temperature to the low density region below.

SUMMARY

Having possible experimental realisations in mind, the general picture is that LFOs are easier to observe for higher amplitude and frequencies of oscillation of the box, while keeping $l_x = l_y$ small; it is at these configurations that LFOs have the highest amplitudes and better defined frequencies, as quantified by A_0 and I_0 , respectively. Let us now remember that at this limit we also observed the most clear phase separation in the Leidenfrost state, with distinct low and high density regions. In our model, presented next, the separation of the phases and the confinement of the system to a one-dimensional geometry implies the existence of LFOs, and the frequency is essentially determined by the ratio of the low and high densities.

2.3 CONTINUUM MODEL

After observing the collective movement of the particles in the column geometry, an oscillator-like description naturally comes to mind. The two coexisting frequencies observed in the spectra suggest a forced oscillator model, with clearly defined forcing and response frequencies. In the following we derive such frequency behaviour from a continuum description of the granular media. We begin by consider-

ing Cauchy's equations for mass and momentum conservation:

$$D_t \rho + \rho(\nabla \cdot \vec{u}) = 0, \quad (2.1)$$

$$D_t(\rho \vec{u}) = \nabla \cdot \hat{\sigma} - \rho g \hat{z}, \quad (2.2)$$

where ρ corresponds to the material density, $\vec{u} = \{u, v, w\}$ is the velocity vector, $\hat{\sigma}$ the stress tensor and g the gravitational acceleration in the downwards direction, $-\hat{z}$. Furthermore, the material derivative is defined as $D_t \equiv \partial_t + \vec{u} \cdot \nabla$. We consider the same scaling as in simulations, with length scales in units of particle diameters \bar{d} , time units given by gravity $\bar{t}_g = (\bar{d}/\bar{g})^{1/2}$, as also $\bar{\rho}_p$, taken as the mass density of a single particle, $\bar{\rho}_p = \bar{m}_p/\bar{V}_p$, with $\bar{V}_p = \frac{1}{6}\pi\bar{d}^3$.

As has been observed in simulations, the dynamics of the system in the column limit is effectively one-dimensional. This immediately suggest the consideration of $\rho = \rho(z, t)$, $\vec{u} = w(z, t)\hat{z}$ and $\hat{\sigma} = \sigma_{zz}(z, t)$. Substituting in (2.1) yields

$$\partial_t \rho + w \partial_z \rho + \rho \partial_z w = 0. \quad (2.3)$$

Furthermore, expanding (2.2), and using (2.3), one reaches a one-dimensional momentum conservation equation

$$\rho \partial_t w = \partial_z \sigma_{zz} - \rho g. \quad (2.4)$$

TWO PHASES APPROXIMATION

In order to solve (2.4) it would be necessary to know both the density and the velocity profiles, $\rho(z, t)$ and $w(z, t)$. Our approach consists in eliminating the z -dependence from (2.4) by integrating in the vertical direction, and taking a first order approximation of the density profile $\rho(z, t)$, and average values for the vertical velocity profile $w(z, t)$. We begin by integrating (2.4) in the vertical direction

$$\int_{b(t)}^{s(t)} \rho \partial_t w \, dz = \int_{b(t)}^{s(t)} \partial_z \sigma_{zz} \, dz - g \int_{b(t)}^{s(t)} \rho \, dz, \quad (2.5)$$

with the bottom boundary, $b(t)$, and top boundary, $s(t)$, dependent on time, due to the movement of the bottom wall and the free surface at the top.

The approximation of $\rho(z)$ consists in dividing the system in two separate, constant density regions, inspired by the measured Leidenfrost state density profile. Let us remember that this approximation becomes increasingly better as S increases and A_f decreases, as shown in Figure 2.3. Consequently, a low density region is defined where $\rho(z, t) = \rho_g(t)$, for $z < \xi$; and a high density region where $\rho(z, t) = \rho_s(t)$, for $z > \xi$, with $\xi = \xi(t)$ the position of the interface between the two regions. Figure 2.8 shows a schematic representation of this approximation, and the origin of its motivation. It then follows that the first integral in (2.5) can be expanded as

$$\int_{b(t)}^{s(t)} \rho \partial_t w \, dz = \rho_g \int_{b(t)}^{\xi(t)} \partial_t w \, dz + \rho_s \int_{\xi(t)}^{s(t)} \partial_t w \, dz. \quad (2.6)$$

Analogously, the third integral in (2.5) becomes

$$g \int_{b(t)}^{s(t)} \rho dz = g\rho_g \int_{b(t)}^{\xi(t)} dz + g\rho_s \int_{\xi(t)}^{s(t)} dz = g\rho_g h_g + g\rho_s h_s, \quad (2.7)$$

with $h_g(t) \equiv \xi(t) - b(t)$ the height of the gaseous region, and $h_s(t) \equiv s(t) - \xi(t)$ the height of the solid region.

Notice that the second integral in (2.5), corresponding to the stress term, is a perfect integral, and thus only the stress boundary conditions are needed for its evaluation. We assume the stress through the system to be continuous in z , and thus it is not necessary to evaluate σ_{zz} at the interface position $\xi(t)$. Thus, from (2.5) we finally obtain:

$$\rho_g \int_{b(t)}^{\xi(t)} \partial_t w dz + \rho_s \int_{\xi(t)}^{s(t)} \partial_t w dz = \sigma_{zz}(z=s) - \sigma_{zz}(z=b) - g\rho_g h_g - g\rho_s h_s. \quad (2.8)$$

BOUNDARY CONDITIONS

It now becomes necessary to specify the boundary conditions. The shaking of the container implies that $b(t) = \hat{A}_{f_m} \sin(\omega_{f_m} t)$, with \hat{A}_{f_m} and ω_{f_m} the amplitude and frequency of energy injection in the model. At the top, $s(t)$, we consider a free surface, and thus the kinematic boundary conditions are given by

$$w(b(t), t) = v_b = \hat{A}_{f_m} \omega_{f_m} \cos(\omega_{f_m} t) \quad (2.9)$$

$$w(s(t), t) = \partial_t s \quad (2.10)$$

Furthermore, the stress at the bottom and top of the granular media are needed. The free surface at the top is straightforward: $\sigma_{zz}(z=s) = 0$. At the bottom, on the other hand, we divide the stress contribution in two: mean (σ_b^0) and fluctuating (σ_b) terms, where the mean term is straightforward: $\sigma_b^0 = Mg/\eta$, with M the total mass of the system, $M = Nm$; and η the area of the base of the container, $\eta = l_x l_y$.

For the fluctuating part of the stress, σ_b , we first consider the force applied to the granular medium by the moving bottom:

$$\sigma_b = \frac{F_b}{\eta} = d_t(m_b v_b) \quad (2.11)$$

with m_b the mass being pushed by the bottom wall. In order to obtain m_b , let us consider a moving platform of surface area η pushing an ideal, incompressible gas of density ρ_g , in analogy to the moving box and the low density region observed in our system. Accordingly, the mass pushed by the box in time is given by $dm_p = \rho_g \eta v_b dt$. Notice that this is valid for high S , where gravity effects on the dynamics of the particles can be ignored. Integrating, we directly get that $m_p = \rho_g \eta \hat{A}_{f_m} \sin(\omega_{f_m} t)$. Substituting in (2.11):

$$F_b = d_t(m_p v_b) = \rho_g \eta \hat{A}_{f_m}^2 \omega_{f_m}^2 \cos(2\omega_{f_m} t). \quad (2.12)$$

Notice that we have naturally obtained $\hat{A}_{f_m}^2 \omega_{f_m}^2 \equiv S_m g$ as the amplitude of the force applied by the oscillating bottom, further suggesting that the shaking strength is the relevant parameter for the system in the high S limit. It then follows, from (2.11), that:

$$\sigma_b = g \rho_g S_m \cos(2\omega_{f_m} t). \quad (2.13)$$

Finally, substituting the stress boundary values in (2.8), we obtain:

$$\rho_g \int_{b(t)}^{\xi(t)} \partial_t w \, dz + \rho_s \int_{\xi(t)}^{s(t)} \partial_t w \, dz = g \rho_g S_m \cos(2\omega_{f_m} t) + g \frac{M}{\eta} - g \rho_g h_g - g \rho_s h_s. \quad (2.14)$$

HEIGHT AVERAGING

The remaining two integrals in (2.14) involve the velocity profile, $w = w(z, t)$, which varies in the vertical direction. In order to solve these integrals we height-average, that is, for a given quantity $f(z)$, we consider its average value

$$\bar{f} \equiv \frac{1}{h} \int_{b(t)}^{s(t)} f \, dz = \frac{1}{h_g} \int_{b(t)}^{\xi(t)} f \, dz + \frac{1}{h_s} \int_{\xi(t)}^{s(t)} f \, dz. \quad (2.15)$$

Notice that, from the first integral in (2.14), f would correspond to $\partial_t w$. Thus, before applying (2.15), we express the integral as a total time derivative. Considering that the boundaries are time dependent, it becomes necessary to use Leibniz integration rule, and thus the first integral in (2.14) can be expressed as

$$\int_{b(t)}^{\xi(t)} \partial_t w \, dz = g S_m \cos^2(\omega_{f_m} t) - w(z = \xi) d_t \xi + d_t \int_{b(t)}^{\xi(t)} w \, dz \quad (2.16)$$

Analogously, the second integral in (2.14) becomes, after using (2.10),

$$\int_{\xi(t)}^{s(t)} \partial_t w \, dz = w(z = \xi) d_t \xi - (d_t s)^2 + d_t \int_{\xi(t)}^{s(t)} w \, dz, \quad (2.17)$$

Substituting (2.16) and (2.17) in (2.14), and using (2.15), we finally obtain:

$$\begin{aligned} -\rho_g w(z = \xi) d_t \xi + \rho_g d_t (h_g \bar{w}_g) + \rho_s w(z = \xi) d_t \xi - \rho_s (d_t s)^2 + \rho_s d_t (h_s \bar{w}_s) = \\ \frac{1}{2} g \rho_g S_m (3 \cos(2\omega_{f_m} t) + 1) + g \frac{M}{\eta} - g \rho_g h_g - g \rho_s h_s \end{aligned} \quad (2.18)$$

Based on the behaviour observed in simulations, we now assume that the high density region is incompressible. This implies that $d_t h_s = 0$, as also that the velocity of the continuum media at the interface position is equivalent to the velocity of the interface, and hence to the velocity of the surface, that is, $w(z = \xi) = \bar{w}_s = d_t s = d_t \xi$. Thus (2.18) becomes

$$\begin{aligned} -\rho_g (d_t \xi)^2 + \rho_g d_t (h_g \bar{w}_g) + \rho_s h_s d_{tt} \xi = \frac{1}{2} g \rho_g S_m (3 \cos(2\omega_{f_m} t) + 1) \\ + g \frac{M}{\eta} - g \rho_g h_g - g \rho_s h_s. \end{aligned} \quad (2.19)$$

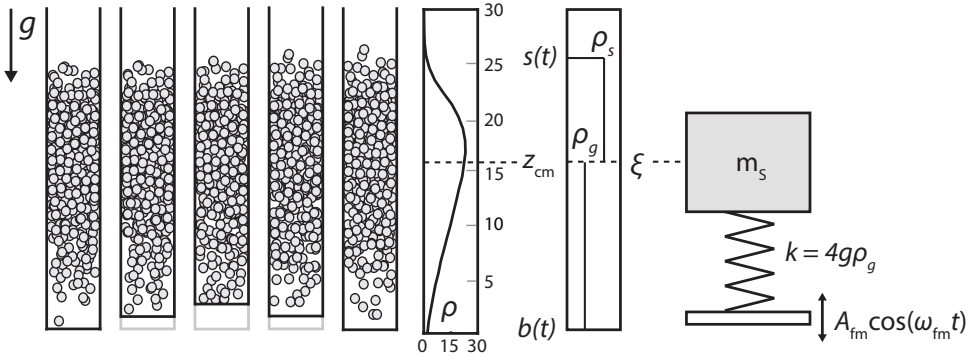


Figure 2.8: From left to right, snapshots from simulations showing an LFO period, at phases 0 , $\pi/2$, π , $3\pi/2$ and 2π ; the corresponding time averaged density profile, a representation of the two phases approximation made for the continuum equations, and finally a schematic representation of the model. The dashed line shows the position of the centre of mass, z_{cm} , which in the model corresponds to the position of the interface between the two phases, ξ , which also corresponds to the position of the mass of a forced harmonic oscillator.

Furthermore, we now use the fact that $h_g(t) = \xi(t) - b(t)$. Thus, substituting and dividing by ρ_s , we obtain

$$\begin{aligned}
 & -\frac{\rho_g}{\rho_s} (d_t \xi)^2 + \frac{\rho_g}{\rho_s} d_t (\xi \bar{w}_g) - \frac{\rho_g}{\rho_s} d_t (\hat{A}_{f_m} \sin(\omega_{f_m} t) \bar{w}_g) + h_s d_{tt} \xi = \\
 & \frac{g \rho_g}{2 \rho_s} S_m (3 \cos(2 \omega_{f_m} t) + 1) + \frac{g M}{\eta \rho_s} - \frac{g \rho_g}{\rho_s} \xi + \frac{g \rho_g}{\rho_s} \hat{A}_{f_m} \sin(\omega_{f_m} t) - g h_s
 \end{aligned} \quad (2.20)$$

FIRST ORDER APPROXIMATIONS

It now becomes relevant to consider the relative importance of each of these terms, in the region of phase space where simulations show that LFOs are present, that is, for $S \gg 1$. First, we consider that $\rho_g/\rho_s \sim \mathcal{O}(\epsilon)$, a condition that holds better for $S \gg 1$ and low A_f , as shown in Figure 2.3. On the other hand, $\xi \sim 10 \sim \mathcal{O}(1/\epsilon)$, as can be seen from Figure 2.5. Furthermore, we measure from simulations that $\delta_t \xi \sim 0.2 \sim \mathcal{O}(\epsilon)$ and $\delta_{tt} \xi \sim 0.1 \sim \mathcal{O}(\epsilon)$, meaning that the dynamics of the LFOs are considerably lower than the typical velocity of grain diameters per gravity timescale, as can also be deduced by the previously obtained frequencies ω_0 . Let us also notice that $h_s \sim h_g \sim 8 \sim \mathcal{O}(1/\epsilon)$, again, from Figure 2.3. Finally, from simulations we obtain that $\bar{w}_g \sim 0.2 \sim \mathcal{O}(\epsilon)$, and $d_t \bar{w}_g \sim 0.02 \sim \mathcal{O}(\epsilon^2)$. Taking into account all these considerations, it becomes straightforward to see that the first term in (2.20) is $\mathcal{O}(\epsilon^3)$, the second term is at most $\mathcal{O}(\epsilon^2)$, the third is then $\mathcal{O}(\epsilon)$, and the fourth term is $\mathcal{O}(1)$. Moreover, all terms on the right side are $\mathcal{O}(1)$, except for the fourth term, which is $\mathcal{O}(\epsilon)$. Thus, disregarding small terms in (2.20), after dividing by h_s , we obtain

$$d_{tt}\xi + \frac{g\rho_g}{m_s}\xi = \frac{g\rho_g}{2m_s}S_m(3\cos(2\omega_{f_m}t) + 1) + g\frac{m_g}{m_s} \quad (2.21)$$

where we have defined the mass of the solid region per unit base area η , $m_s \equiv h_s\rho_s$, and the equivalent of the gaseous region, $m_g = h_g\rho_g$. Equation (2.21) corresponds to a forced harmonic oscillator equation of the form:

$$d_{tt}\xi + \omega_{0_m}^2\xi = F_0\cos(2\omega_{f_m}t) + C, \quad (2.22)$$

with natural frequency

$$\omega_{0_m}^2 = \frac{g\rho_g}{m_s}, \quad (2.23)$$

amplitude of forcing $F_0 = \frac{3}{2}g\rho_g S_m/m_s$, and constant $C = \frac{1}{2}g\rho_g S_m/m_s + gm_g/m_s$.

MODEL AND SIMULATIONS COMPARISON

We have shown that, considering Cauchy's equations for continuum media, and making assumptions in concordance to the observed granular Leidenfrost state, the system becomes equivalent to a simple forced harmonic oscillator, expressed by (2.22). In this case, ξ is the displacement of the centre of mass around the equilibrium position at 0, ω_{0_m} the natural frequency of the system, and F_0 and ω_{f_m} the amplitude and frequency of the forcing. The analogy of the forcing with the granular column is straightforward: ω_{0_m} and A_{0_m} would be equivalent to ω_0 and A_0 , respectively. Furthermore, we choose ξ to correspond to z_{cm} , in order to directly compare with previous measurements.

Notice that the natural frequency ω_{0_m} does not explicitly depend on the forcing frequency ω_{f_m} , as can be seen in (2.23). The implicit dependence comes from the variation of ρ_g and m_s with ω_{f_m} , as observed in simulations, where, for fixed S , ρ_g/ρ_s increases with ω_f , giving the correct inverse proportionality of ω_{0_m} with ω_{f_m} . Therefore, in order to obtain a frequency from the model, only ρ_g and m_s need to be specified, which we measure from simulations.

Both quantities can be obtained from $\rho(z)$, the density in the granular column as a function of height. In order to obtain an accurate average, we consider $\rho^* \equiv \rho(z - z_{cm}(t), t)$, which makes all profiles directly comparable. This is analogous, in the model, to centering the profiles at the interface between the two distinct regions. It is then straightforward to compute ρ_g as the average value of the density for $z < z_{cm}$. On the other hand, m_s we take as the total mass for $z > z_{cm}$, taking care not to count particles that are in free flight above the solid region, as they do not have influence on the oscillator dynamics. This implies that although the center of our profiles is z_{cm} , m_g is not equal to m_s .

The comparison between the frequencies obtained in simulations and from the model is presented in Figures 2.9a-c. For low amplitudes, $A_f \leq 1.0$, and high frequencies, $S \geq 144$, the agreement between the frequencies is within the error bars.

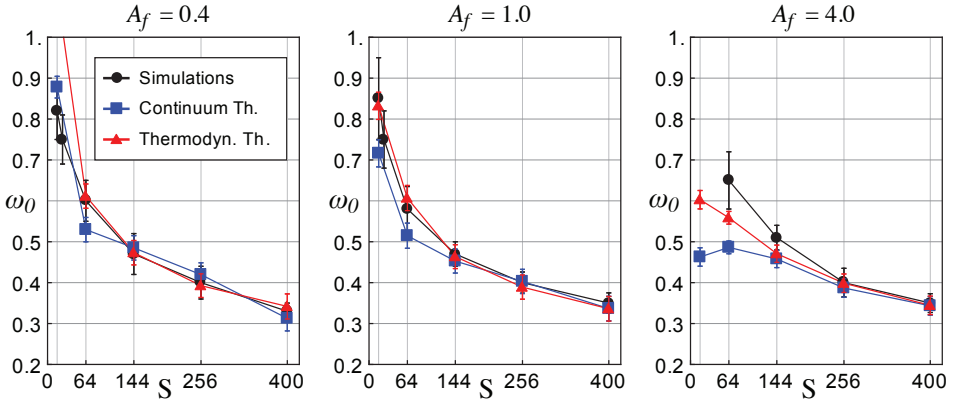


Figure 2.9: Low-frequency oscillation frequencies ω_0 , as a function of the dimensionless shaking strength S , for different box oscillation amplitudes: $A = 0.4$ (a), $A = 1.0$ (b) and $A = 4.0$ (c). All systems have $l_x = 5$, $F = 12$. Simulation (black) corresponds to frequencies obtained from fast-Fourier transform of the simulation data, while continuum and thermodynamic/kinetic theory data points (blue and red, respectively) are obtained from models presented in sections 2.3 and 2.4, respectively, using data acquired from simulations.

For lower S , or higher amplitudes, the assumption of two distinct phases, as also the approximation of $\xi \sim 1/\epsilon$, become less justified, resulting in the model consistently underpredicting the frequencies, with more than 50% disagreement at the point of the bouncing bed-Leidenfrost transition for $A = 4.0$. We believe that the prediction could be improved by considering more complex density profiles, as also by including terms of lower orders, although this exceeds the scope of our work. In general terms, the resulting one-dimensional model turns out to be a remarkable well approximation for high ω_f and low A_f , showing that this many-particle, out-of-equilibrium system actually behaves as a regular forced harmonic oscillator when confined in a column, in the corresponding energy injection region.

2.4 THERMODYNAMIC MODEL

Remarkably, it is possible to obtain another accurate expression for ω_0 using a completely different approach, considering basic concepts from thermodynamics. Assuming a spring-like behaviour, the natural frequency of our medium is given by $\omega_0^2 = k/m_s$, with k the stiffness constant of the spring-like medium, and m_s the mass sustained by the spring. We also know that $k = \eta B/h_g$, with B the bulk modulus, η the area of the spring, and h_g it's height at rest. Assuming an adiabatic ideal gas, it is possible to relate the bulk modulus with the pressure, $B = \gamma P_0$, with γ the adiabatic index. Notice that the ideal gas approximation is being used only for the gaseous

region of the Leidenfrost regime, where densities are low and no significant correlation of the particles is observed. We then obtain:

$$\omega_0^2 = \frac{\gamma \eta P_0}{h_g m_s}. \quad (2.24)$$

The pressure P_0 is taken as the force caused by the solid mass the spring sustains, m_s , divided by the area of the container: $P_0 = m_s g / \eta$. Thus, we finally reach:

$$\omega_0^2 = \frac{\gamma g}{h_g}. \quad (2.25)$$

This significantly simple expression is remarkably accurate when compared with simulation measurements. Figures 2.9a-c also show $\omega_0(S)$ for this model, taking h_g to be the same as in the previous section, z_{cm} . The adiabatic index is considered as $\gamma = 1.67$, the theoretical value for an ideal monoatomic gas. The agreement is again within error bars for high frequencies, and deviates considerably for lower frequencies, except for the $A = 1.0$ case, where low frequencies are also captured. Essentially, we have calculated the natural frequency of a vertical spring-mass system where the spring is actually an ideal gas, a situation analogous to that existing in the Leidenfrost state. We have assumed here that P_0 is constant, a situation that in our case is possible only by heating the gaseous region (due to the loss of energy through collisions), but it is not necessary to know the form of energy injection to compute the natural frequency ω_0 . Relating the two obtained LFOs frequencies, equations (2.23) and (2.25), one obtains $\gamma = m_g / m_s$; the interpretation of this result remains a challenge.

2.5 CONCLUSIONS

A vertically vibrated bed of grains presents low-frequency oscillations (LFOs) due to the decoupling of the driving frequency and the dynamics of a high density region suspended by a lower density one. The relevance of these oscillations increases as the distinction between the two densities increases, that is, proportional to the frequency and inversely to the amplitude of oscillation of the system container. The LFO frequencies are inversely proportional to the driving frequency, and follow a common power law for a range of amplitudes. The amplitude of the oscillations, on the other hand, increases in an almost linear way with the frequency.

Event-driven simulations give an overall excellent qualitative and quantitative agreement with experiments and soft-particle simulations done in wider systems, although they show discrepancies in some critical transition values. We remark that the hard-sphere approximation can be meaningful even in systems with very high-density regions, as present in the Leidenfrost state. The considerable speed advantage makes it extremely useful, and sometimes the only means to systematically study high dimensional parameter spaces.

Starting from Cauchy's equations for conservation of mass and momentum, integrating in the vertical direction and assuming two distinct low and high constant density regions, it is possible to reproduce the frequency behaviour observed in simulations. That is, a forced harmonic oscillator, with the natural frequency proportional to the ratio of the densities. This simple model is able to predict the natural LFO frequency for high excitation frequencies, where in fact the two phases are well separated. The non-linear terms, discarded in our analysis, should provide the necessary corrections for lower frequencies, as well as the consideration of a more realistic density profile. A second approach, using thermodynamic arguments, also gives a remarkably accurate expression for the frequencies, although in this case just a simple mass-spring system behaviour was assumed. The quantitative agreement of both models is nevertheless remarkable, taking into account the low number of particles involved, and the presence of very high and low density regions.

Further insight could be gained by appropriately coarse graining the granular medium in order to obtain stress fields, which would directly relate both models. A point of interest, not studied here, is how well do kinetic theory predictions hold in such a system, taking into account the reduced container size, the small number of particles and the presence of considerably different densities. Current work is being done on verifying the consistency of macroscopic fields obtained by theoretical arguments and coarse-grained simulational data.

We suggest that LFOs, here shown to be ubiquitous to vertically vibrated density inverted systems, could play a fundamental role in the Leidenfrost-convection transition. More specifically, LFOs could be the primary source of density fluctuations observed before convection is triggered, when one region of the system oscillates at a different phase than another. Understanding this will need further simulation and experimental research.

APPENDIX: COLLISION LAW

Let us consider the collision between two perfectly hard and spherical particles. Hard-spheres interactions can be understood by a Heaviside potential energy function with its limit set by the particles radius. Known are the initial position of both particles \vec{r}_i (with $i = \{1, 2\}$ the index of the respective particle), the lineal velocities \vec{v}_i , the angular velocities $\vec{\omega}_i$, the masses m_i and the diameters d_i . Considering linear and angular momentum conservation, $\vec{p}' = \vec{p} + \Delta\vec{p}$, $\vec{L}' = \vec{L} + \Delta\vec{L}$, with primed variables denoting post-collision quantities, the linear and angular velocities are then given by:

$$\vec{v}'_1 = \vec{v}_1 + \Delta\vec{p}/m_1 \qquad \vec{\omega}'_1 = \vec{\omega}_1 - \frac{d_1}{2I_1} \hat{n} \times \Delta\vec{p} \qquad (2.26)$$

$$\vec{v}'_2 = \vec{v}_2 - \Delta\vec{p}/m_2 \qquad \vec{\omega}'_2 = \vec{\omega}_2 - \frac{d_2}{2I_2} \hat{n} \times \Delta\vec{p} \qquad (2.27)$$

with $\hat{n} = (\vec{r}_1 - \vec{r}_2)/|\vec{r}_1 - \vec{r}_2|$ the unitary vector in the direction defined by both particles centers, I_i the moment of inertia of the particles ($I_i = q_i m (d_i/2)^2$, with $q = 2/5$ for spheres), and $\Delta\vec{p}$ the change of momentum of particle 1 due to the collision. In general, a collisional model is an specification of $\Delta\vec{p}(\vec{v}, \vec{\omega}, m, d)$. In what follows we give the specific forms used in this work. The problem can be greatly simplified by decomposing the vectorial quantities in normal and tangential directions with respect to \hat{n} , such that $\vec{p} = \vec{p}^{(n)} + \vec{p}^{(t)}$.

In the normal direction, the change of momentum is taken to be

$$\Delta\vec{p}^{(n)} = -m_{12}(1 + \epsilon_n)\vec{v}_c^{(n)}, \quad (2.28)$$

with ϵ_n the normal restitution coefficient ($\epsilon_n = v_c^{(n)}/v_c^{(n)}$), $m_{12} = m_1 m_2 / (m_1 + m_2)$ the reduced mass, and \vec{v}_c the relative velocity at the contact point,

$$\vec{v}_c = \vec{v}_1 - \vec{v}_2 - \left(\frac{d_1}{2} \vec{\omega}_1 + \frac{d_2}{2} \vec{\omega}_2 \right) \times \hat{n}. \quad (2.29)$$

That is, energy loss is taken to be proportional to the velocity of impact. For simplicity, we consider ϵ_n to be independent of the relative velocity of impact or, what is equivalent, we take ϵ_n to be the average of the in reality broad distribution of ϵ_n in the space of impact linear and rotational velocities. We expect that this first-moment approximation is valid in the highly fluidized cases we consider.

The tangential component of the change of momentum, $\Delta p^{(t)}$, can be obtained by Coulomb's law in its momentum form, $|\Delta\vec{p}^{(t)}| \leq \mu_s |\Delta\vec{p}^{(n)}|$. The condition is implemented by computing:

$$\Delta\vec{p}^{(t)} = \begin{cases} m_{12} \left(\frac{q}{1+q} \right) (1 + \epsilon_t) \vec{v}_c^{(t)} & |\Delta\vec{p}^{(t)}| \leq \mu_s |\Delta\vec{p}^{(n)}| \\ \mu_d \vec{v}_c^{(n)} & |\Delta\vec{p}^{(t)}| > \mu_s |\Delta\vec{p}^{(n)}| \end{cases} \quad (2.30)$$

where the first expression is computed and then the condition tested. With $\Delta\vec{p}$ known, the post-collisional velocities can now be computed. The set of variables needed is $\{\vec{r}_i, \vec{v}_i, \vec{\omega}_i, m_i, I_i, d_i\}$, and the parameters are $\{\epsilon_n, \epsilon_t, \mu_s, \mu_d\}$.

LOW-FREQUENCY OSCILLATIONS AND CONVECTIVE PHENOMENA IN A VIBRATED GRANULAR SYSTEM¹

Low-frequency oscillations (LFOs) are thought to play an important role in the transition between the Leidenfrost and convective states of a vibrated granular bed. This work details the first experimental observation of LFOs, which are found to be consistently present for a range of driving frequencies and amplitudes, with particles of varying material and using containers of differing material properties. The experimentally acquired results show a close qualitative and quantitative agreement with both theory and simulations across the range of parameters tested. Strong agreement between experimental and simulational results was also observed when investigating the influence of sidewall dissipation on LFOs and vertical density profiles. This chapter additionally provides evidence of two phenomena present in the Leidenfrost state which are previously unobserved in experiment, simulation or theory: a circulatory motion over extended time periods in near-crystalline configurations, and a Leidenfrost-like state in which the dense upper region displays an unusual 'inverse' thermal convection.

1. Based on: C.R.K. Windows-Yule, N. Rivas, D.J. Parker, A.R. Thornton, Physical Review E, 90 (6), 062205, 2014.

3.1 INTRODUCTION

Granular materials, large collections of discrete, macroscopic particles, have been the subject of considerable research for over two centuries, due largely to their ubiquity in nature and industry [1], and the plethora of interesting phenomena they exhibit [28, 29]. They can exist in numerous states, many of which are analogous to those of a molecular material. Examples include convection [121], phase separation [38, 40], Faraday-like patterns [61], and the granular Leidenfrost state [15], wherein a dense region of grains is supported from below by a dilute, energetic gaseous region, in direct analogy to the eponymous state observed in classical fluids [74]. Although the vertically vibrated narrow box geometry has been extensively studied [60, 79, 71, 122], recent simulational and theoretical work [123] has suggested the presence of a previously unobserved phenomenon: low-frequency oscillations (LFOs). This term refers to the periodicity observed in the motion of a granulate in a density-inverted state, i.e. in the Leidenfrost or convective regimes. The name LFO comes to the fact that the frequency of this oscillatory motion is considerably lower than that of the vibrating plate exciting the granular bed.

In this chapter we provide experimental evidence of the existence of LFOs in a vibrofluidised granular bed. In addition to our confirmation of previous theoretical and simulational results, presented in the previous chapter, we also report the observation of two new phenomena which are, to the best of the authors' knowledge, previously unobserved either in experimental *or* simulated granular systems. The role of dissipation at the horizontal boundaries of the system is also explored; side-walls have previously been shown to significantly affect the behaviour of both two-[124] and three-dimensional [119] systems, and as such are likely to have a significant impact on the phenomena observed in the quasi-one-dimensional (quasi-1D) and laterally constrained three-dimensional systems such as those used here.

The chapter is structured as follows: we begin by describing our basic experimental setup, specifying the manner in which data is extracted from the system and how this setup is recreated in simulations, before briefly summarising the continuum model introduced in Chapter 2 [123]. We then proceed to present our major results, firstly comparing our experimental findings to the predictions of the existing theoretical and simulational models, before presenting two previously unobserved convective phenomena, and discussing the possible underlying mechanisms thereof. A summary of our major results and their implications is provided in the last section.

3.2 SYSTEM DETAILS

EXPERIMENTAL SETUP

In order to experimentally observe the Leidenfrost state, a granular bed consisting of 12 square-packed layers of glass or steel spheres is housed in a cuboid container

of dimensions $l_x \times l_y \times l_z = 25 \times 25 \times 250$ mm and vibrated sinusoidally in the vertical direction. A simplified representation of experimental setup may be seen in Figure 3.1. A range of vibrational frequencies, $\omega \in (88, 572)$ Hz, and peak amplitudes, $A \in (0.8, 6.0)$ mm, are used to excite the system. The significant variation in ω and A , and hence the dimensionless shaking strength, $S = \omega^2 A^2 / g d$, allows us to explore a variety of differing dynamical states.

The height l_z of the container is adequate to ensure an effectively ‘open’ system. Spheres of diameter $d = 1, 2, 3$ and 5 mm are used, giving the system a range of dimensionless widths, $\tilde{l}_x = l_x / d \in (5, 25)$. The lower limit of this range corresponds to the situation of a ‘granular column’, wherein horizontally inhomogeneous states are suppressed and, therefore, the system can be considered quasi-1D. This frustration of collective motion facilitates the clear observation of LFOs. The base and sidewalls of the container are steel, giving an effective particle-wall coefficient of restitution $\epsilon_w = 0.70$. This value is an average over a wide distribution which includes kinetic energy losses due to rotations and different impact velocities [125]. The use of a steel walls ensures rigidity, and also removes the possibility of static charges affecting the system. A single opposing pair of sidewalls can be replaced with perspex ($\epsilon_w = 0.33$), allowing the effects of sidewall dissipation to be investigated.

Experimental data is acquired using Positron Emission Particle Tracking (PEPT), a non-invasive technique whereby a single particle, physically identical to the others in the system, is ‘labelled’ with a β^+ -emitting isotope. The back-to-back pairs of γ -rays emitted due to the rapid annihilation of positrons with electrons within this ‘tracer particle’ are detected using a dual-headed gamma camera, and can be used to triangulate its position with millimetre precision and millisecond time resolution [126]. A simple illustration of this process may be seen in Figure 3.1. The time averaged motion of this single particle can then be used to give information pertaining to the system as a whole. For instance, in PEPT data may be used to create one-dimensional density profiles. This is achieved by subdividing the computational volume into a series of thin horizontal segments, each of height dz . The fraction of time spent by the tracer in each of these segments may then be recorded. Due to the ergodicity of the system under investigation, this residence time fraction is directly proportional to the local packing density within each region allowing, for adequately small segments, a vertical density profile to be reproduced. An example of such profile may be seen in Figure 3.2, where it is compared with a simulation equivalent. The overall shape and qualitative features of both cases coincide, although the discrepancies in the low-density region are significant. These may originate from the experiment underestimating the packing fraction of the gaseous region due to the high velocities, and thus low residency times, near the bottom, moving boundary. Furthermore, the hard-sphere approximation used in simulations, as detailed in the next section, may lead to overestimations of the overall dissipation in the gaseous region.

In order to ensure reliable statistics, all experiments are conducted over a period

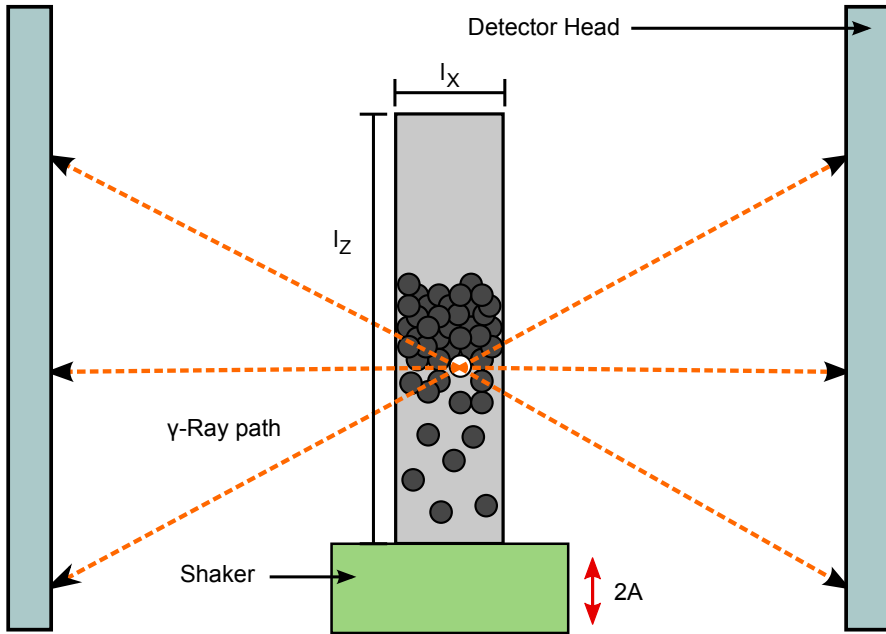


Figure 3.1: Schematic representation of the experimental system, showing a granular bed in the density-inverted Leidenfrost state. Although in reality the radioactive tracer particle is physically identical to all others in the system, for the sake of clarity this particle is here highlighted in white. Dotted orange arrows represent the paths taken by the γ -rays emitted by the tracer, while the solid red arrow represents the direction of vibration.

of between 45 and 120 minutes, dependent on the density of the system under investigation and the strength with which it is driven. Since denser and/or more weakly excited systems exhibit slower dynamics, the run duration must be accordingly increased in order to allow the tracer particle to fully explore the entire system, including both the dense and dilute phases. For further information regarding PEPT, see references [126, 127].

EVENT-DRIVEN SIMULATIONS

Simulations are performed using an event-driven (ED) molecular dynamics [86]. The algorithm uses a hard-sphere model, assuming binary collisions with no overlap and no long-range forces between particles. This is the same simulation code as used in Chapter 2 and [123], where a more detailed description of the algorithm can be found. Collisions between particles are modelled by normal and tangential velocity-

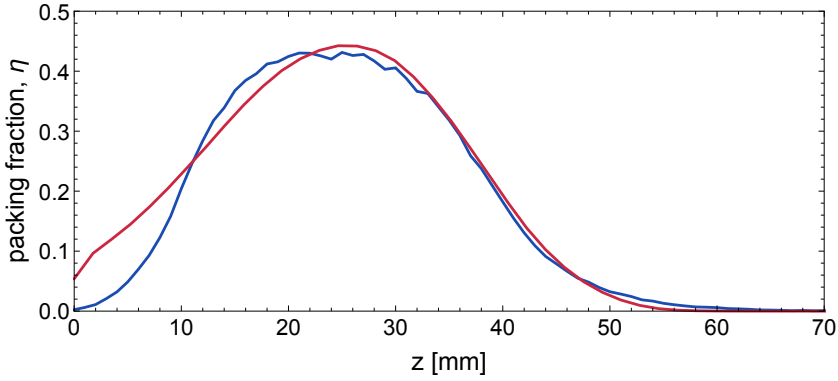


Figure 3.2: Experimentally (blue) and simulationally (red) acquired one-dimensional vertical packing fraction profile, demonstrating the general form expected for a granular bed in the density-inverted Leidenfrost state. In this image, we clearly see a particle-dense region resting atop a considerably more dilute, gaseous phase. The data presented correspond to a bed of 1 mm diameter glass particles excited via vibration at a constant frequency $\omega = 157$ Hz and amplitude $A = 4$ mm.

dependent restitution coefficients, following the expression in [128]

$$r(v) = \begin{cases} 1 - (1 - r_0) \left(\frac{v}{v_0}\right)^{1/5} & v \leq v_0 \\ r_0 \left(\frac{v}{v_0}\right)^{-1/4} & v \geq v_0. \end{cases}$$

Material properties were chosen such that, at a typical particle velocity $v_0 = 0.3\text{ms}^{-1}$, the relevant coefficients of restitution, r_0 , are $r_0 \sim 0.90$ and $r_0 \sim 0.95$ for glass and stainless steel particles respectively. These particular are in accordance with previous experimental measurements [129, 117]. The use of a velocity-dependent r_0 ensures that dissipation is not over-estimated at high particle densities, as can occur when using constant coefficients [130]. Static and dynamic friction coefficients (μ_s and μ_d , respectively) are also considered, and held constant at $\mu_s = \mu_d = 0.05$. For particle-wall collisions the value $r_0^w = 0.7$ was used for glass, and $r_0^w = 0.75$ for steel particles, while $\mu_s^w = \mu_d^w = 0.15$. Although no specific values are known for these type of collisions, it is expected that particle-wall collisions have a considerably lower restitution coefficient than particle-particle collisions. Although it was verified that these values are not critical to the observation of the phenomena, the system is quantitatively sensitive to them. Finally, we remark that in simulations walls are considered infinitely massive, and thus their movement unaffected by the particles' impact, an effect which could be relevant in experiments.

CONTINUUM MODEL

An expression for the frequency of the LFOs can also be obtained from a continuum model (described in detail in Chapter 2), given the vertical density profile. In this model, a granulate in the Leidenfrost state is considered to have two distinct phases: a dense, solid-like region of density ρ_s and mass per unit area in the horizontal plane, m_s , and a gaseous region of density ρ_g . The periodic vertical motion of the dense region can be described as a forced harmonic oscillator, allowing the frequency of LFOs, ω_0 , to be simply calculated as:

$$\omega_0 = \sqrt{\frac{g\rho_g}{m_s}} \quad (3.1)$$

3.3 RESULTS AND ANALYSIS

Although the existence of LFOs in density inverted systems was shown in simulations and predicted theoretically in [123], their presence has not, until now, been confirmed experimentally². Figure 3.3 shows a typical example of the evolution of the tracer particle's vertical position, $z(t)$, for both experimental and simulation data. Low-frequency oscillations can be observed when looking at short time-windows as a slight movement of the particles' position, superimposed in a slower up-and-down migration through the granular bed. The nature of the second effect will be studied later. Furthermore, we show the corresponding fast Fourier transforms (FFT) in Figure 3.4. To minimise noise, $z(t)$ is split into a series of 10s traces, each containing approximately 3×10^4 data points, and the corresponding FFTs averaged. The presence of LFOs can be identified by a broad peak in the power spectrum at a frequency ω_0 one or two orders of magnitude lower than the driving frequency ω_f . Thus, the existence of a clearly-defined low-frequency peak in Figure 3.4 evidences the existence of LFOs in an experimental system. It should be noted that Figure 3.4 is indeed a *typical example*: LFOs are observed over a wide range of driving frequencies, $\omega_f \in (94, 503)$ Hz, and amplitudes, $A \in (1, 5)$ mm (the upper values being limited by the maximum obtainable velocity of the shaker used to drive the system). Monodisperse beds composed of both steel and glass particles also exhibit LFOs over a range of particle sizes $d \in (2, 5)$ mm, and for both steel- and acrylic-walled systems, showing it to be a robust and easily-reproducible phenomenon. In the following discussion, we initially focus on glass beads of 3 mm and 5 mm diameter, in order to avoid the presence of bouyancy driven convection, which typically dominates the system dynamics for smaller particle sizes. Figure 3.5 shows data in the S - A phase space for these two cases. Remarkably, all experimental data sets for which the system exists in the Leidenfrost state are seen to exhibit low-frequency

² Behaviour suggestive of the presence of LFOs may be observed in the data of Folli *et al.* [131]. However, due to considerable disparities between their system and the current setup, it is not possible to confirm that this is the same phenomenon.

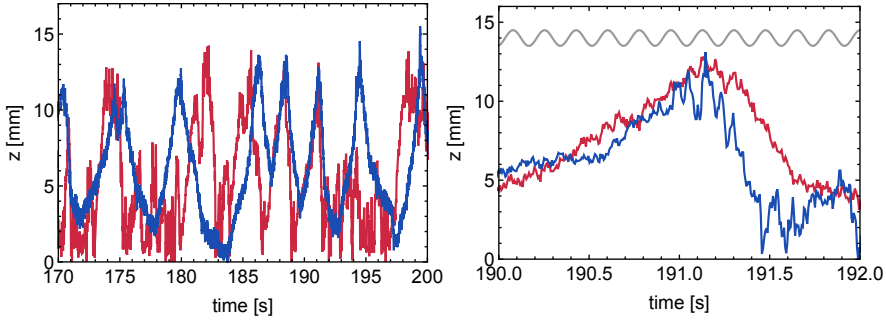


Figure 3.3: Vertical position, $z(t)$, of a single particle in experiments (blue) and simulations (red), for a system of 3mm glass spheres with $\omega = 327$ Hz and $A = 2$ mm. Data is shown for larger (left) and smaller (right) time windows. For comparison, the frequency of the low-frequency oscillations is shown in the left figure (gray).

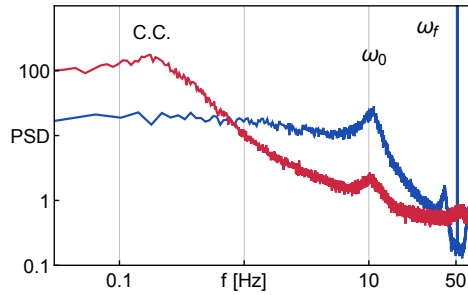


Figure 3.4: Power spectra of $z(t)$, for experimental (blue) and simulation (red) data, showing ω_f and ω_0 , the driving and LFO frequency respectively, as well as the crystalline convection frequency, C.C.

oscillations. Thus, the phase diagrams presented provide a clear indication of the ranges of parameters for which one may expect to observe LFOs.

From the FFTs of $z(t)$ we are able to obtain the dominant LFO frequency. Figure 3.6 shows ω_0 for experiments, simulations, and the value computed from the model. A good agreement is observed between three cases, in the case of the model increasing with the energy input. This is to be expected, as the model is formally only valid in the large shaking amplitude limit [123]. For all other particle numbers and sizes, wall and particle inelasticities and driving parameters explored, the experimentally obtained values of ω_0 agree with those produced by both the ED and continuum models to within 10%. The persistent presence of LFOs across such a broad range of parameter space, including the highly elastic limit at which the behaviour of granular systems approaches that of classical, molecular systems, sug-

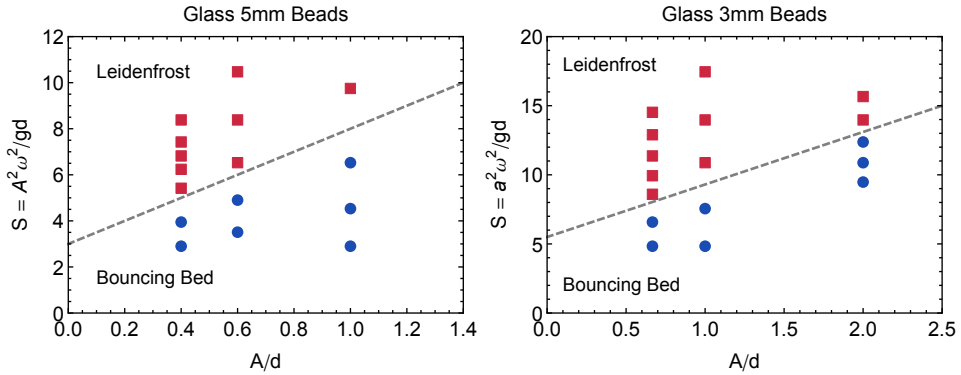


Figure 3.5: Phase space for 5mm (left) and 3mm (right) glass beads. As the magnitude of the energy injection, S , increases, the system goes from the bouncing bed (blue dots) to the Leidenfrost (red squares) state. The transition region is roughly delimited by the horizontal dashed gray line.

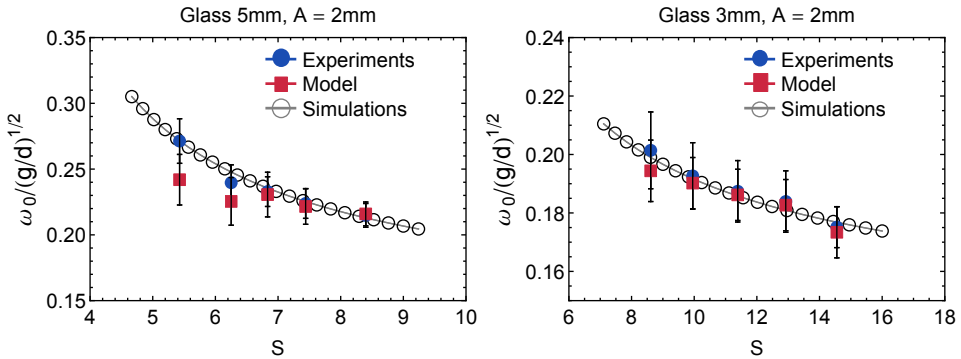


Figure 3.6: Experimental, simulational and theoretical values of the characteristic frequency of the low-frequency oscillations, ω_0 , as a function of the shaking strength $S \equiv A^2 \omega_f^2 / gd$. Data for $d = 5\text{mm}$ (left) and $d = 3\text{mm}$ (right) glass particles, for $A = 2\text{mm}$.

gests that an analogous phenomenon may also be present in classical fluids.

THE EFFECT OF SIDEWALL DISSIPATION

In a constrained system, such as the one described here, we expect the dissipation of the walls to significantly affect the dynamics of the bed. Thus, to further explore the generality of our results, the material of a single pair of sidewalls is altered, hence altering r_0^w . Notice that, even in constrained systems, if a system's packing fraction is large, r_0^w is typically considered unimportant, as particle-particle collisions are expected to be the leading contributors the overall dissipation. Thus, the

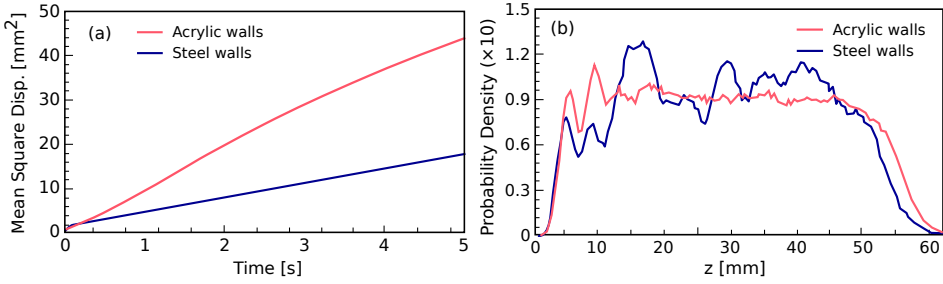


Figure 3.7: (a) Experimental mean squared displacement, $M(t)$, for particles in the dense upper region of the system for steel (blue, dark grey) and acrylic (red, light grey) sidewalls. For both cases, $\omega = 327$ Hz, $A = 2$ mm and $l_x = 5$. (b) Normalised vertical packing profiles corresponding to the same system parameters.

current set-up allows us to explore the competing effects due to lateral confinement and packing density. Comparison of data acquired from otherwise identical systems with steel ($\epsilon_w = 0.7$) and acrylic ($\epsilon_w = 0.33$) sidewalls shows the increased dissipation caused by the less elastic sidewalls to considerably affect even highly dense systems, even with all other parameters held constant. This observation is illustrated by the residence time distributions shown in Figure 3.7b. It should be noted, however, that LFOs are still found to be present for both sidewall materials. It is additionally worth specifically noting that we do not expect the inclusion of the acrylic walls to introduce any appreciable effects due to triboelectric charging, due both to the relatively large sizes and masses of the particles concerned, as well as the frequent collisions experienced by particles and the system's two remaining steel sidewalls and base, which will act to rapidly dissipate charge. In both of the profiles presented in Figure 3.7b, we see the existence of multiple 'peaks' and 'valleys', indicative of the presence of crystalline structure within the bed. However, these local maxima and minima are considerably more pronounced in the acrylic-walled system than its steel-walled counterpart, indicating a significantly increased degree of crystallisation in the former. This makes sense, as higher wall dissipation will clearly lead to a decrease in the fluctuating component of the kinetic energy (granular temperature). Figure 3.7a shows the typical mean squared displacement of particles in the upper region of the system for both sidewall types. The markedly reduced mobility of particles in the acrylic-walled system again demonstrates the heat-sink-like effect of the dissipative system boundaries.

It is interesting to note the marked differences between the density profiles presented in Figure 3.7b and that shown in Figure 3.2, another clear demonstration that LFOs exist for a variety of system parameters and dynamic states, and also coexist with various other phenomena.

CRYSTALLINE CONVECTION IN THE LEIDENFROST STATE

Analysis of $z(t)$ and the corresponding power spectra for denser, less-fluidised systems shows evidence of an extremely slow, pseudo-periodic motion, with a frequency approximately two orders of magnitude lower even than the previously discussed LFOs (see Figures 3.3a and 3.4). This slow migration of particles was also observed in simulations, as illustrated in Figure 3.3a. However, in order to obtain the periodic behaviour observed in experiments, it was necessary to modify the frictional and elastic coefficients of the collision model for particle-wall interactions, indicating a strong influence of the side-boundaries on this phenomenon. Although a somewhat similar phenomenon has been previously reported in a multiphase system [132], this is, to the best of the authors' knowledge, the first time such behaviour has been observed in a monodisperse granular bed. It is possible, on an adequately long time scale - $\mathcal{O}(10^3)$ s - to observe dynamics reminiscent of convective motion within the densely packed crystalline phase of the upper region. Specifically, grains are seen to move, on average, upward in the central region of the domain and downward in the vicinity of the lateral boundaries. This motion is distinct from the conventional, continuous convective flow previously observed [118]. Here, the bed maintains a crystalline structure, with the migration of particles occurring in sudden, discrete motions separated by periods of inactivity. The mean flow rate associated with this 'crystalline convection' is typically $\mathcal{O}(0.1)$ mm/s, compared to the values of ≈ 3 mm/s for reverse convection and ≈ 6 mm/s typical of the 'normal' convection observed within the system. Further study of this state may give insight into the origins of the transition of a granular system between a mechanically stable solid-like state and a disordered, fluid-like state, a matter on which there is no general consensus, despite significant research in the area [133]. Such research could also lead to an improved understanding of the Leidenfrost-convection transition.

REVERSE CONVECTION IN THE LEIDENFROST STATE

In a system such as the one detailed here, a granular bed may exhibit thermal or buoyancy-driven convection [121]. In systems with dissipative side-boundaries, one may observe a 'wall-enhanced' thermal convection, whereby a region of increased density near the sidewalls leads to the formation of a pair of convection rolls reminiscent of Rayleigh-Bénard cells [67]; the rolls move downward in a thin stream near the walls, where increased dissipation leads to a locally higher density and lower energy, and upward in the centre of the container where the density is, accordingly, reduced [134]. It should be noted that this form of convection is distinct from the frictionally-driven convection observed in less strongly-excited systems than those discussed here [135]. For data sets where $\tilde{l}_x > 5$, such wall-induced convection is indeed observed. However, for certain combinations of ω and A , with $\tilde{l}_x = 25$, one observes a density-inverted state in which the denser upper region displays convective motion whose sense is opposite to the expected (see Figure 3.8). Previously, reverse

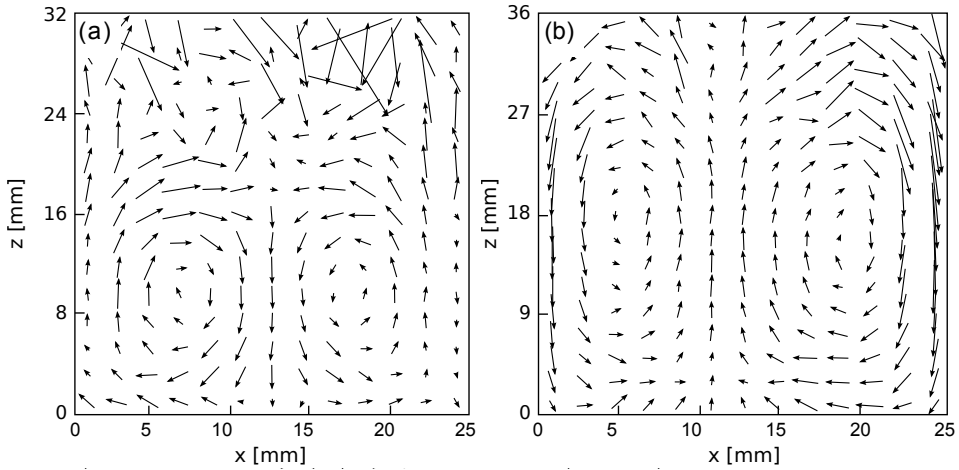


Figure 3.8: (a) Velocity field for the dense upper region of a system of 1mm particles in a density-inverted state, driven at $A = 4\text{mm}$, $\omega = 157\text{Hz}$. The arrows, whose lengths and orientations are representative of the magnitude and direction of the average velocity through a section of the field, show a net downward motion in the centre of the system and a net upward motion near the side-boundaries. (b) Velocity plot showing, for comparison, typical wall-enhanced convection. The driving parameters for this case are $A = 1\text{mm}$ and $\omega = 509\text{Hz}$.

convection had only been observed in *frictionally* driven systems [48]; the inversion of *buoyancy-driven* convection is, to the best of the authors' knowledge, a previously unobserved phenomenon in experimental systems. We propose a tentative explanation for this effect: sidewall dissipation is more influential in lower-density regions [136], where the ratio of particle-wall to particle-particle collisions is higher. Thus, in the dilute lower region of the Leidenfrost state, a pronounced increase in density and decrease in temperature will occur near the walls of the system, leading to a decreased pressure in this region [9]. Conversely, for the upper region of the bed, one observes an increased relative density in the central region of the bed (see Figure 3.9). This greater compaction near the centre may be due to the increased pressure acting on the upper bed due to the relatively energetic gas in the central region below. At the interface between the upper and lower regions of the bed, collisions from particles in the energetic lower region will break the structure of particles in the dense region, creating a localised volume of more energetic, lower density particles which will tend to rise through the bed. These relatively mobile particles are likely to be pushed radially outward from the centre of the container due to the pressure gradients in the dilute region below, increasing the probability that upward motion will occur near the side-boundaries of the container. Moreover, the slightly decreased density in the upper bed near the sidewalls means that the upward transit of the

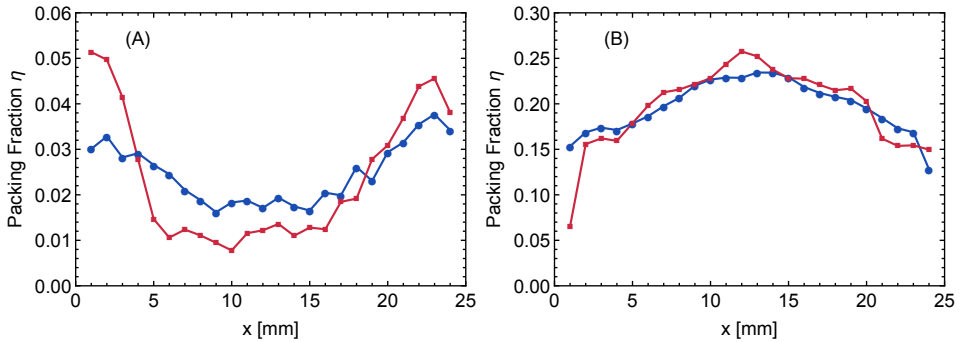


Figure 3.9: Packing fraction, η as a function of horizontal position for (a) the lower, gaseous region of the system and (b) the dense upper region, for steel (blue, dark grey) and acrylic (red, light grey) sidewalls, for $A = 2\text{mm}$, $\omega = 320\text{Hz}$, and glass particles of $d = 5\text{mm}$.

energetic particles is less likely to be impeded. Due to conservation of mass flux, this will naturally result in a pair of inversely-oriented convection rolls within the system. The combination of ω and A at which this new phenomenon is observed suggests that it may be representative of a transitional state between the Leidenfrost state and the *Faraday wave* state [16]. It should be noted that the behaviour detailed above was found to be reproducible, and was still observed when the system's sidewall material was altered, although differences in the convective flow rate and the specific densities of each phase were observed for the two cases. Specifically, as the sidewall coefficient of restitution was decreased from 0.70 to 0.33, the convective flow rate of the system was found to increase from $\approx 2.5\text{mm/s}$ to $\approx 3.7\text{mm/s}$. The authors believe this phenomenon to be worthy of further study.

3.4 CONCLUSIONS

Analysis of the motion of a single particle in a granular bed, acquired using positron emission particle tracking, has been used to provide, for the first time, strong experimental evidence of low-frequency oscillations in density-inverted, vibrofluidised granular systems. The experimentally observed frequencies of these oscillations, and the variation of these frequencies with numerous system parameters, were found to correspond closely to simulation and continuum theory. The observation of LFOs over a wide range of parameters supports the hypothesis that they are a fundamental feature of the Leidenfrost state, meaning that future study of these oscillations could prove crucial to the understanding of the transition of a granular system between the Leidenfrost and convective regimes. The findings of this study also suggest the existence of two new phenomena, the further study of which may provide valuable insight into transitions involving the Leidenfrost state.

FROM THE GRANULAR LEIDENFROST STATE TO BUOYANCY-DRIVEN CONVECTION¹

Grains inside a vertically vibrated box undergo a transition from a density inverted and horizontally homogeneous state, referred to as the granular Leidenfrost state, to a buoyancy-driven convective state. We perform a simulational study of the precursory states of such a transition, and quantify their dynamics as the bed of grains is progressively fluidized. The transition is preceded by transient convective states, which increase their correlation time as the transition point is approached. Increasingly correlated convective flows lead to density fluctuations, as quantified by the structure factor, which also shows critical behaviour near the transition point. The amplitude of the modulations in the vertical velocity field are seen to be best described by a quintic supercritical amplitude equation with an additive noise term. The validity of such an amplitude equation, and previously observed low-frequency oscillations of the bed of grains, suggests a new interpretation of the transition analogous to a coupled chain of vertically vibrated damped oscillators. Increasing the size of the container shows metastability of convective states, as well as an overall invariant critical behaviour close to the transition.

1. Based on: N. Rivas, A.R. Thornton, S. Luding, D. van der Meer, Physical Review E, Submitted.

4.1 INTRODUCTION

Granular materials—collections of macroscopic, dissipative particles—are an archetypal study case of complex dynamical systems. Decades of research have revealed many novel non-equilibrium phase transitions and collective behaviours [61, 38, 137, 28, 138, 29], the study of which not only has a fundamental physical interest, but is also relevant for many industries [139, 140, 141]. Many of these behaviours show a striking similarity with molecular fluids or solid phenomena [121, 111, 142, 143], and some have even been successfully described by equilibrium theories [30]. Studying the origin of these agreements advances our understanding of far-from-equilibrium states, and explores the limits of continuum descriptions of discrete systems. Furthermore, the low number of constituents, when compared to molecular counterparts, makes granular materials particularly suited for the study of noise effects in spatially extended transitions, a subject of increasing physical interest due to the ubiquitous presence of fluctuations in natural phenomena [33, 137, 34, 36, 144].

In order to keep granular media fluidized it is necessary to provide energy to the system. Previously this has been done in several distinct ways, as for example electromagnetically [145, 146], by shearing [147], or by boundary forces such as rotating a drum [148] or vibrating the grains' container [63]. In vertically vibrated systems several complex collective dynamic behaviours have been observed, such as segregation [58, 149], pattern formation [29] and phase separation [38]. One particular case of the latter is the granular Leidenfrost state, where a dense, solid- or fluid-like region is sustained by a highly agitated low density gaseous region in contact with the vibrated bottom wall [15, 79]. It is so called because of the clear analogy with the water-over-vapour phenomenon observed in molecular fluids in contact with a high temperature surface [115]. If the vibration strength is increased, the Leidenfrost state evolves to a buoyancy-driven convective state [150], in analogy to Rayleigh-Bernard convection. Recently, it was shown that granular hydrodynamics is able to quantitatively capture the critical points of this instability, by performing a linear stability analysis of perturbations over the Leidenfrost state [150, 80].

In the following chapter we study the precursor states of the transition from the granular Leidenfrost to the buoyancy-driven convective state in the context of bifurcations and critical theory. The transition is observed as the energy input is increased and the bed of grains goes from a steady and homogeneous Leidenfrost state to a buoyancy-driven convective phase. After specifying the system and simulation methods, we begin by characterizing the two states involved in the transition, and determining the phase space of the system by means of a convection intensity order parameter. With this, we are then able to study time-dependent transient convective states, that are present far below the transition and show a critically increasing correlation time as the transition is approached. Furthermore, the static structure function allows us to study the evolution of the relevant length-scale in this pattern formation scenario, and see its behaviour prior to the transition. Finally,

it is observed that the amplitude of the critical pattern follows a growth ratio that is consistent with a quintic supercritical bifurcation, associated with parametrically driven spatially extended systems [36, 151, 152]. We suggest that the agreement with this universality class comes from the presence of collective semi-periodic oscillations, so called low-frequency oscillations (LFOs), present in density inverted systems [123]. All results are presented for different boundary conditions and sizes of the container, allowing us to observe the influence of confinement and variations of the total number of particles.

4.2 SYSTEM AND SIMULATIONS

The setup consists of a quasi-two-dimensional rectangular box with open top, vibrated in the vertical direction. Two different box widths are considered, defining the *narrow* system, with $l_x = 50$, and the *wide* one, with $l_x = 400$. The depth of the container, on the other hand, is kept constant, $l_y = 5$; a schematic representation of the studied geometries is shown in Figure 4.1. Here, and in what follows, we use dimensionless quantities with d as lengthscale and $\sqrt{d/g}$ as timescale, and thus $\sqrt{g/d}$ as velocity units; when necessary, dimensional quantities will be distinguished by a tilde, i.e. $\tilde{l}_x = l_x d$. Grains are considered to be perfectly spherical, frictionless and monodisperse in size and mass. Their total number N is determined by the number of filling layers $F \equiv N/(l_x l_y)$, which we fix at $F = 12$. Previous studies show that both the Leidenfrost and the buoyancy-driven convective states are observable for this number of layers [71]. The whole box (base and side walls) is vertically vibrated in a bi-parabolic, quasi-sinusoidal way with a given frequency ω and amplitude A . The use of a quadratic interpolation instead of a sine function gives a considerable speed advantage in simulations, as the collision times with the moving walls can be predicted analytically. Previously, test simulations have been done using a sine function for exemplary cases, and no significant difference was observed [123, 118]. The amplitude of oscillation is kept fixed, $A = 0.1$, and thus the energy injection is controlled by the angular frequency ω . The low amplitude is chosen to reduce as much as possible the effects of the moving boundary, and approximate the limit of a temperature boundary condition [153]. Higher driving amplitudes lead to a coupling of the bottom boundary movement with the number density field, creating shock waves that propagate through the granular medium [24]. Moreover, low amplitudes eliminate other inhomogeneous states for lower energies, such as undulations [71], which are not the object of this study. Overall, our selection of parameters is based on previous experimental setups where the transition was previously reported [71, 150].

The system is simulated using an event-driven (ED) hard-sphere algorithm. The advantage of using ED simulations over regular time-stepping methods is straightforward: computational speed. Even though the number of particles is relatively low ($\sim 10^4$), the high frequencies and very long simulation times make the use of discrete particle methods (DPM) infeasible. In DPM simulations time-steps are constant and

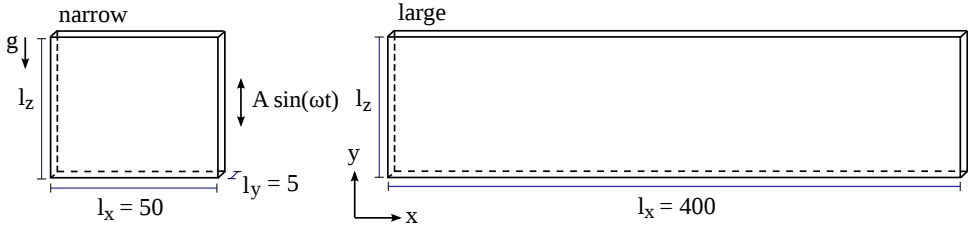


Figure 4.1: Schematic representation (not to scale) of the setup. Two different geometries are considered: narrow (left) and wide (right). Lengths are given in units of particle diameters d .

should be at least one order of magnitude lower than the lowest relevant time-scale, $T = 2\pi/\omega$ [154]. Thus, for the high frequencies considered in our study, the small time-step prohibits to simulate in a practical time the long transients involved near a transition. On the contrary, the average time-step in ED is determined mainly by the density of the system, and not directly dependent on the frequency of oscillation of the container.

Collisions between particles are modelled by a normal restitution coefficient, $r_p = 0.9$ [116]. We disregard rotational degrees of freedom, and any other physical effect that is not captured by the hard-sphere model, with the goal of keeping the model as simple as possible. This particular value is in accordance with collisions of glass or stainless steel particles [117]. In order to avoid inelastic collapse, the TC model is used, where particle collisions are considered elastic if they occur within a given time, which we take as $t_c = 10^{-5}$ [87]. This essentially sets a lower limit for physically relevant velocities, as also slightly decreases the packing fraction of high density regions; possible relevant effects will be noted when appropriate.

Regarding boundary conditions, we consider both cases of periodic (PBC) and solid boundary conditions, with either elastic or dissipative walls (EBC and DBC, respectively). The different boundary types are only applied in the x -direction, as we would like to investigate the effects they have on the transition independent of other factors, as increased overall dissipation or free-volume; setting dissipative or periodic boundaries also in the y -direction would make the comparison less straightforward, as the overall dissipation would decrease considerably. Dissipative walls are set with the same restitution coefficient as between particles, $r_w = 0.9$. The effects of dissipative walls on convective states have already been studied in similar setups, both experimentally and numerically [119]. Here we are interested in the effects of walls on the excitation or suppression of the modes relevant in the transition. Elastic walls (EBC) are used in order to see the influence of excluded volume effects near the sidewalls when comparing with periodic walls PBC, as also to facilitate the analysis of fluctuations by fixing a reference frame. Furthermore, PBCs are used to study the dynamics of the bed of grains without confinement.

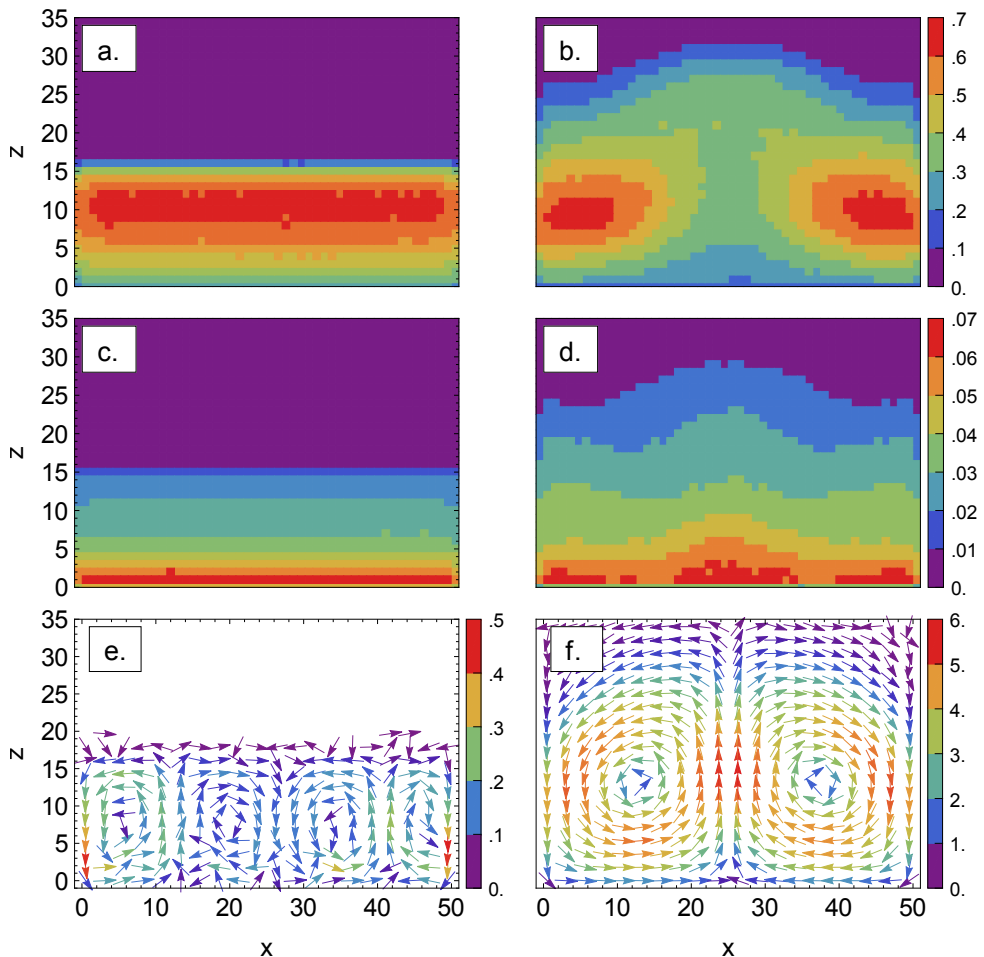


Figure 4.2: In the narrow system, time averaged number density of particles $\langle n(x,z) \rangle_t$ (top), granular temperature $\langle T(x,z) \rangle_t$ (middle) and velocity field $\langle \vec{v}(x,z) \rangle_t$ (bottom), for systems in the granular Leidenfrost state (left) and in the buoyancy-driven convective state (right).

4.3 RESULTS

MACROSCOPIC DESCRIPTION

The most evident difference between the granular Leidenfrost and buoyancy-driven convective states is the level of horizontal homogeneity. Figure 4.2 shows time averaged number density $\langle n(x,z) \rangle_t$, granular temperature $\langle T(x,z) \rangle_t$ and velocity fields $\langle \vec{v}(x,z) \rangle_t$ in each state, for narrow systems with EBC. The fields are obtained by binning the system in squares of size d . Time averages, $\langle \rangle_t$, are always taken for at least

$10^5 \sqrt{d/g}$, which in dimensional terms for $d = 1\text{mm}$ would correspond to experiments of about fifteen minutes. The granular temperature is defined as the kinetic energy of the fluctuating velocity, $3k_B T \equiv m(\langle v^2 \rangle - \langle v \rangle^2)$. The fields clearly show that in the Leidenfrost state, both ρ and T are homogeneous in the x -direction, while in the convective state the profiles are modulated by a dominant mode k_c . That is, the transition is *morphogenetic* [155], as a pattern or new relevant length-scale arises from a homogeneous state. The convective mode defines the typical size of the convective cell, λ_c ; in the case shown in Figure 4.2, $\langle \lambda_c \rangle_t \approx 50$, that is, $k_c = 1/\lambda_c \approx 0.02$. An important condition of the system states that $k_c l_x = n$, with n an integer or half-integer; the consequences of this requirement will be elaborated further along.

It is important to remark that the buoyancy-driven convective state is also density inverted (see Figure 4.2b), and thus this characteristic is not a sufficient condition to define the Leidenfrost state. We demand two further properties for the system to be considered in this state: (a) higher density regions present distinct dynamics to the lower density ones (gas/fluid or gas/solid), to distinguish it from completely gaseous states [72]; and (b) the system remains horizontally homogeneous, to differentiate it from the convective state. The different phases mentioned in (a) can be quantitatively distinguished by, for example, the pair correlation function and its characteristic decay for each phase. In short, we define the granular Leidenfrost state as a density inverted, phase coexisting, horizontally homogeneous state.

As the energy input increases, the bed of grains in the dense region progressively loses its horizontal homogeneity, giving rise to convection; this is what we refer to as the granular Leidenfrost to buoyancy-driven convection transition or, in short, the LBC transition. In the following we define an order parameter based on the evolution of the velocity field, and observe its behaviour through the transition.

CONVECTION INTENSITY

For the study of critical behaviours it is of fundamental importance that the transition region between the two states is accurately measured. The different states can be easily distinguished by looking at the time-average velocity fields, which suggest the use of the convection intensity order parameter, defined as

$$C \equiv \frac{1}{2} \max_z (\max_x (v_z(x, z)) - \min_x (v_z(x, z))). \quad (4.1)$$

Here $v_z(x, z)$ is the scalar field of velocities in the z -direction, and the maxima are taken first over z and then over x . In words, C corresponds to half the highest difference of the vertical velocities at a particular height of the container. In a convective state C is expected to be significantly higher than in a random flux case, due to the presence of stable upwards and downwards flux regions (as can be seen in Figure 4.2f). Even though the average vertical velocity is expected to scale with $A\omega$, the localization of the energy fluxes in the convective states is what produces a higher deviation, and thus a higher C . The time averaged convection intensity,

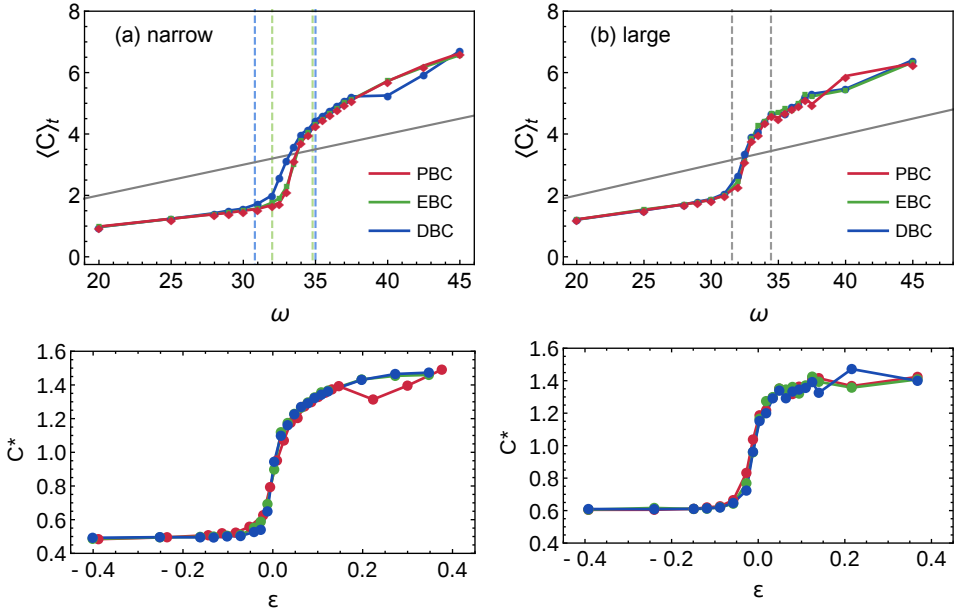


Figure 4.3: (top) Time averaged convection intensity $\langle C \rangle_t$, defined in the main text, as a function of the angular driving frequency ω , for the narrow (left) and large (right) containers with the boundary conditions indicated in the labels. Dashed lines indicate the transition region for the corresponding BC, as specified in the main text. The thick grey line corresponds to $A\omega$, the characteristic shaking velocity. (bottom) Convection intensity normalized by the driving frequency, $C^* \equiv \langle C \rangle_t / A\omega$, as a function of the bifurcation parameter $\varepsilon \equiv (\omega - \omega_c) / \omega_c$, for the same systems as in the top figures.

$\langle C \rangle_t$, captures the transition as a rapid increase with ω , as shown in Figure 4.3 for all considered systems.

In the Leidenfrost state $\langle C \rangle_t$ increases linearly with ω , and is lower than the characteristic velocity of energy injection, $A\omega$. This is followed by a transition region, where $\langle C \rangle_t$ increases sharply and superlinear on $A\omega$, eventually surpassing the $A\omega$ line. Finally, the growth of $\langle C \rangle_t$ saturates as the system enters the stable buoyancy-driven convective state. Quantitatively, we define the limits of the transition region by looking at the intersection of the initial and final linear behaviours with the increasing transient behaviour, the two points defining the width of the transition, $\delta\omega$, and their average the critical frequency ω_c , which coincides within measurement error with the condition $\langle C \rangle_t = A\omega$. For the narrow container, this results in critical frequencies and widths of transition $\omega_c = 33.4 \pm 0.1$, $\delta\omega = 0.22 \pm 0.01$ for EBC and PBC, and $\omega_c = 32.9 \pm 0.1$, $\delta\omega = 0.26 \pm 0.01$ for DBC, with the error given by the resolution of the simulations in ω . That is, elastic boundary conditions have no measurable influence when compared to periodic boundaries, which suggests that

excluded volume effects due to the presence of walls can be disregarded already for $l_x = 50d$. Dissipative boundaries, on the other hand, have the quantitative effect of decreasing ω_c , while increasing $\delta\omega$; even though overall the system presents more dissipation compared to the EBC case, inelastic sidewalls slightly reduce the energy needed to trigger the transition compared to elastic boundaries.

Boundary conditions in the wide container become irrelevant, with all cases given by $\omega_c = 33.0 \pm 0.1$ and $\delta\omega = 0.29 \pm 0.02$. Quantitatively, the critical points are slightly lower and the transitions wider, which we believe is due to the influence of the confinement in the narrow container. It is worthy to remark that the amount of energy needed for the creation of the convective cells is practically invariant on l_x or, equivalently, the number of convective rolls, suggesting that the interaction between rolls has no influence on their creation. Nevertheless, we notice that when EBC or DBC are used, convection cells are seen to appear first at the boundaries, and the boundary rolls are more stable when compared to the bulk of the system. This, nevertheless, happens at the same ω_c as with PBC, suggesting that solid boundaries have no relevant influence on the flux ($n\vec{v}$) strength, but do promote the appearance of convective cells near them.

When normalized by $A\omega$, we can recognize in $C^* \equiv \langle C \rangle_t / \omega$ a shape characteristic of a supercritical pitchfork bifurcation, as shown in the insets of Figure 4.3. The second branch of the ideal pitchfork supercritical bifurcation would correspond to taking the minimum in x , instead of the maximum, in (4.1). When the bifurcation parameter $\varepsilon \equiv (\omega - \omega_c) / \omega_c$ is used as control parameter, all three boundary condition cases coincide for all system sizes considered. This suggests that the transition presents universal behaviour, independent of the amount of dissipation. It is also a confirmation that the critical points are well defined. With the phase-space determined, next we characterize the precursor states of the transition by looking first at correlations of the velocity field, and then at density fluctuations by means of the static structure factor.

TIME-DEPENDENT FLUCTUATING CONVECTIVE FLOWS

Far below the transition point in the Leidenfrost state, starting from $\varepsilon > -0.5$, time-dependent fluctuating convective flows can be observed. These are analogous to the precursor fluxes present in the classical fluid Rayleigh-Bénard convection transition [156], which were theoretically predicted and relatively recently observed by careful experiments in gaseous media [157]. In our case, the convective rolls can be easily identified when observing the evolution of the short-time-averaged transient velocity fields, as shown in Figure 4.4. The cells are constantly generated anywhere in the container, but more frequently next to walls, this of course when they are present, i.e. in the EBC and DBC cases. Two fundamental aspects differentiate such a transient state from the fully developed buoyancy-driven convective state above $\varepsilon = 0$. First, the circulation of particles is not associated with mean density or temperature

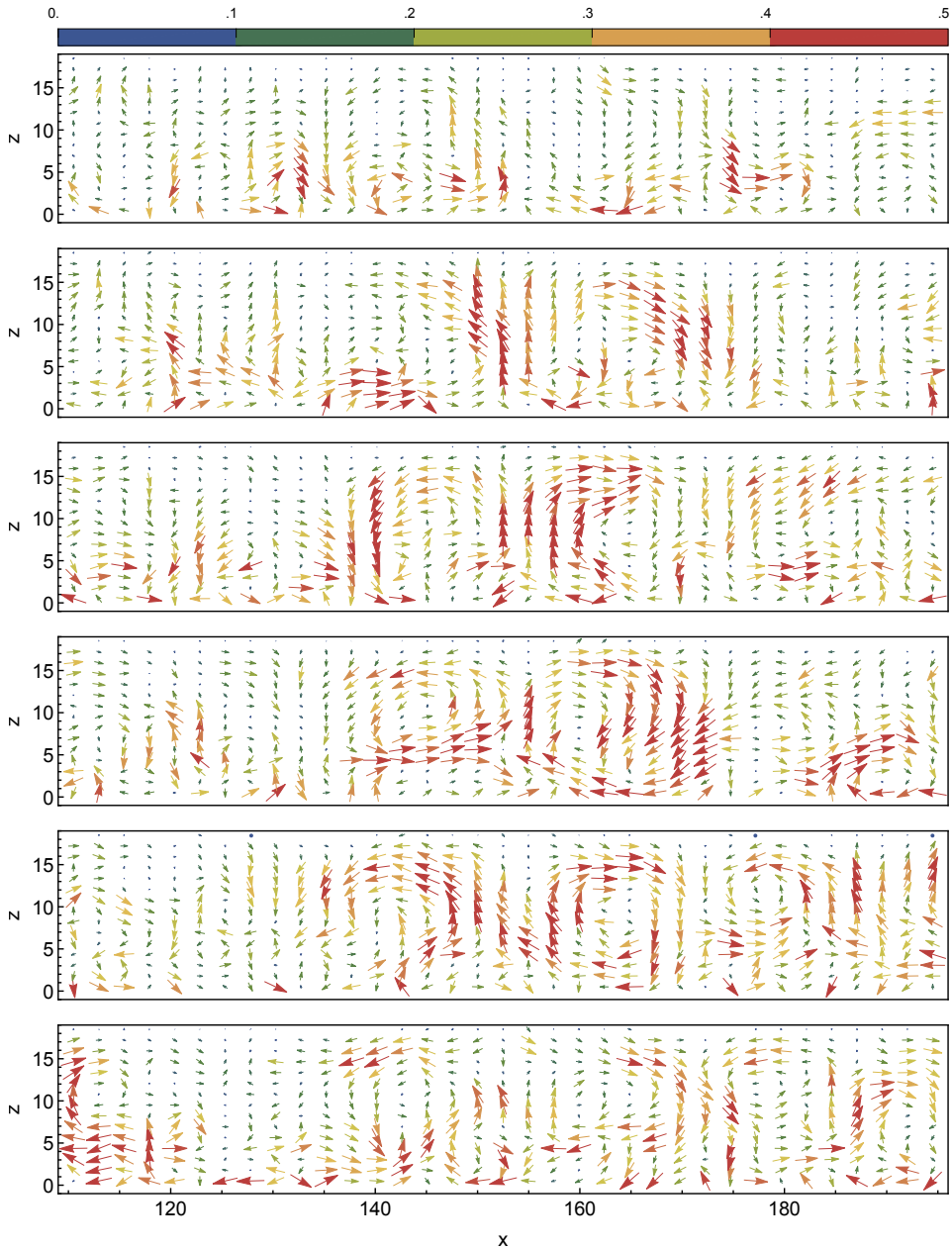


Figure 4.4: Transient velocity fields, each averaged over 5 oscillation periods, showing the emergence and decay of a fluctuating convective cell in a section of a wide container. From blue to red, the colour and size of the vectors corresponds to their norm.

inhomogeneities (it is time-dependent). That is, $\langle n(x, z) \rangle_t$, $\langle T(x, z) \rangle_t$ and $\langle \vec{v}(x, z) \rangle_t$ remain homogeneous in \hat{x} . Second, the convective velocity field is present only as an average, and thus is not correlated with the instantaneous velocity of the particles. That is, the velocities of the fluctuating convective flows are much smaller than the amplitude of the fluctuating velocities (\sqrt{T}), in contrast to the buoyancy-driven convection case, where they are comparable (see Figure 4.2). This has the consequence that, as there is no localization of the fluxes, their effect is not reflected in $\langle C \rangle_t$.

In order to characterize the stability of the transient convective cells, the self-correlation of the fluctuating velocity field is computed,

$$F_v(\tau) = c_F \langle \delta \vec{v}(\vec{x}, t + \tau) \cdot \delta \vec{v}(\vec{x}, t) \rangle_x$$

with $\delta v = \vec{v}(\vec{x}, t) - \langle \vec{v}(\vec{x}, t) \rangle_t$, and c_F a normalization constant such that $F_v(0) = 1$. Figure 4.5a shows $F_v(\tau)$ for characteristic cases of ω . In the following we focus only on EBC and DBC, as they considerably simplify the computation of self-correlation functions by impeding the convective rolls to drift in the x -direction, as they do with PBC. Visual inspection and preliminary analysis of the PBC case suggest that the results can be generalized to this case as well. All correlations present a common shape: an initial quick, power-law-like decay followed by a slower exponential decrease. The rapid decorrelation at short time-scales confirms that the particles' instant velocities are mostly fluctuating, and do not present a high time correlation. On the other hand, for longer times the correlation is comparatively lower, but still considerable, and decays slower. This is a signal of long-term average preferred fluxes. As expected by the critical slowing down of fluctuations near the transition, the overall correlation of this region increases as the critical point is approached, as can also be seen in Figure 4.5a. The characteristic time of decorrelation τ_v is obtained by considering $F_v \sim \exp(-\tau/\tau_v)$. Figure 4.5b shows $\omega\tau_v$ as a function of ε , from where we find a powerlaw $\tau_v \sim \varepsilon^{-\xi}/\omega$ with exponent $\xi \sim 0.51 \pm 0.02$. Closer to the critical point the measurement error becomes significant. The data is presented for the whole range in ω where the Leidenfrost state is present, which is one and a half decade in ε .

Wide systems present the same overall features as the narrow container; τ_v can be determined with a higher precision –as noise is reduced with a higher number of particles–, and presents the same critical exponent ξ as in the narrow case. That is, transient convective flows are independent of the size of the container.

Also visible in $F_v(\tau)$ are wide peaks at regular intervals, signals of a quasi-periodic time-scale of correlation. By observing the evolution of the centre of mass, and computing its fast-Fourier transform, it was verified that this periodic correlation corresponds to the recently reported low-frequency oscillations, present in density inverted agitated systems [123, 158] (see Chapters 2 and 3). The quasi-periodic movement is coupled with a breathing behaviour of the dense bed of grains, which increases and decreases its granular temperature. Here we do not analyse this further; for a detail study of the phenomena we refer the reader to Chapter 2.

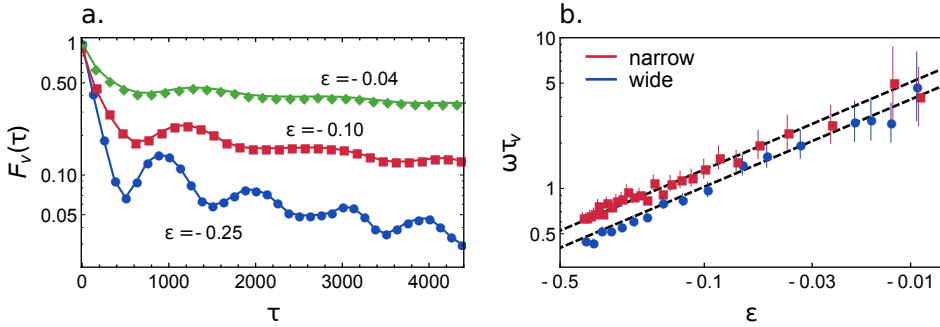


Figure 4.5: (left) Velocity correlation functions F_v for several ω and EBC in the narrow container. (right) Characteristic time-scale of fluctuating convection τ_v , corresponding to the exponent of the long term exponential decay of the self correlation function F_v , as a function of the bifurcation parameter ε . The dashed lines indicate best fits of the form indicated in the main text.

STATIC STRUCTURE FUNCTION

As energy input increases, for $\varepsilon > -0.1$, density fluctuations arise, clearly recognizable as modulations in the surface of the bed of grains. To analyse their behaviour we compute the static structure function,

$$S(k) = \frac{1}{N} \left\langle \left| \hat{n}(k, t) - \langle \hat{n}(k, t) \rangle_t \right|^2 \right\rangle_t, \quad (4.2)$$

with \hat{n} the Fourier components of the depth-averaged number density field in the x -direction,

$$\hat{n}(k, t) = \sum_j^{l_x/\delta_x} n(x_j, t) e^{i2\pi k n(x_j, t)}. \quad (4.3)$$

Notice that we define $k = 1/\lambda$, for a more straightforward comparison between wave number k and wavelength λ . The position x_j is given by regular intervals, $x_j = \frac{1}{2}\delta x + j\delta x$, with $\delta x = 0.1$ the coarse graining length. Notice that instead of considering the particles' position in the definition of \hat{n} we use the averaged density profiles, as it significantly increases the speed of computation. This approximation holds only for low wave-numbers, that is, $1/k \gg \delta x$, which is the region we are interested in. Test cases were done with the usual definition with particles positions, and no significant differences were observed.

Transient modulations of the bed are captured in $S(k)$ by the appearance and steady increase of a narrow peak at $k \approx 0.02$, as shown in Figure 4.6 for both the narrow and wide containers. This implies that the number of convection rolls is proportional to the system size, as their size is roughly constant. We define the

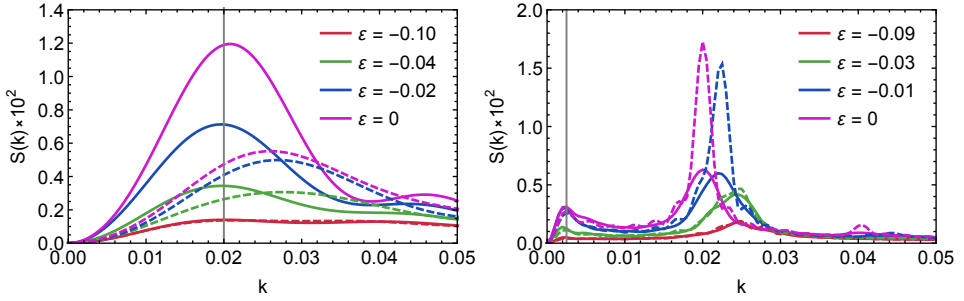


Figure 4.6: Structure factor, $S(k)$, for narrow (left) and wide (right) containers for the bifurcation parameters specified. Dashed lines correspond to PBC, while solid lines have EBC. The vertical solid line indicates the $1/l_x$ point.

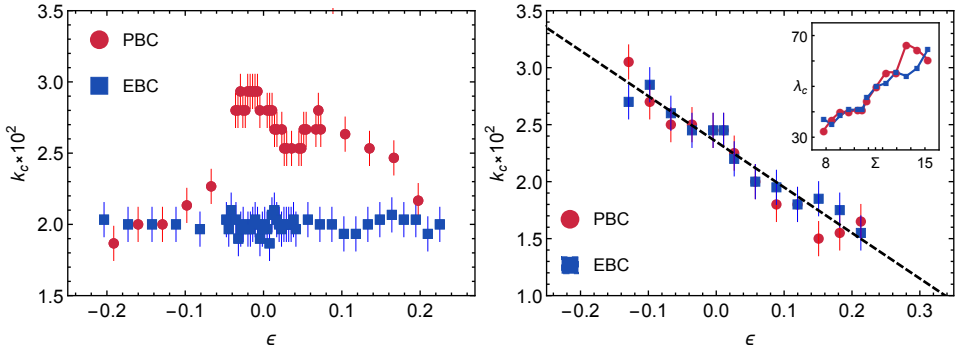


Figure 4.7: The most unstable mode k_c , defined by the maximum of the structure factor $\max(S(k)) \equiv S(k_c)$, as a function of the bifurcation parameter, for narrow (left) and wide (right) containers and the boundary conditions specified.

critical mode k_c by the position of this maximum, that is $S_m \equiv \max(S(k)) \equiv S(k_c)$. Thus, the associated wavelength at the transition point, $\lambda_c^* \approx 50$, corresponds to the size of the smallest stable convection roll, seen to be independent of l_x for $l_x > \lambda_c^*$. What other factors may affect λ_c^* is not studied further here, although we notice that previously realized stability analysis of the granular hydrodynamic equations have found an expression for λ_c^* as a function of the constitutive relations, which are in themselves dependent on the particle properties [80].

Notice from Figure 4.6 that for $\varepsilon = -0.1$ the correlation of the transient convective flows was significant, but $S(k)$ has no relevant maximum. This confirms that fluctuating convective flows take place in a stable homogeneous Leidenfrost state, and are not accompanied by any relevant excitation of the critical mode in the density (and temperature) field.

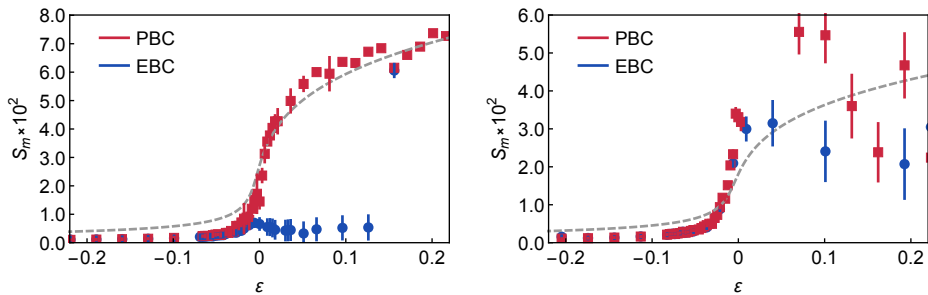


Figure 4.8: Structure factor maximum, S_m , as a function of the bifurcation parameter ε , for EBC (blue) and PBC (red) in narrow (left) and wide (right) containers. As reference, the best fit for the amplitude of the critical mode is included (dashed gray, see main text).

Previous simulational and experimental works have stated that λ_c scales linearly with the shaking strength $\Sigma \equiv \tilde{A}^2 \tilde{\omega}^2 / g d = A^2 \omega^2$ [64, 150]. The inset of Figure 4.7 shows $\lambda_c(\Sigma)$ for the wide container and confirms that this is indeed the case. In contrast, in the narrow container solid walls fix k_c , while with PBC the behaviour is not clear, roughly increasing before the transition point and then decreasing in a non-monotonic way; the uncertainty in the measurements does not allow a more accurate conclusion in this case. The marked difference between both boundary condition cases suggests that, even though EBC and PBC had equal critical points, as measured by $\langle C \rangle_t$, they do have an influence on the modes that are being perturbed. In most of the studied range k^* is consistently higher with PBC, showing that solid boundaries can have the originally unexpected effect of increasing the critical convection roll size. This is due to excluded volume effects near the wall, which decrease the density and thus have the effect of exciting a lower mode, in our case for $\lambda \approx 25$. On the wide container wall effects become negligible, and thus k^* coincides for both types of boundary conditions.

By taking into account that k_c in the wide container is not constant, we interpret the LBC transition for $l_x > \lambda_c^*$ as a series of transitions between energetically similar states. Inherent fluctuations are strong enough to allow the constant switching between contiguous k_c . In terms of the relevant scales, this is a conflict between λ_c , which depends on our control parameter ω , and l_x , which is fixed. As λ_c^* is independent of the container size, the critical behaviour for $|\varepsilon| \sim 0$ is still expected to be universal.

Indeed, $S_m(\varepsilon)$ shows critical-like behaviour for $\varepsilon < 0$, as shown in Figure 4.8. In the narrow container, both types of boundary conditions show the same qualitative growth for $\varepsilon < 0$, although with consistently lower amplitudes in the EBC case, as previously discussed. For $\varepsilon > 0$ the PBC case shows a growth reminiscent of the critical amplitude of a supercritical bifurcations. In this case, S_m is directly related

to the amplitude of the critical mode, as the lack of a fixed reference frame makes $\langle n(x, t) \rangle_t$ homogeneous even in the buoyancy-driven convective state. On the contrary, the EBC case immediately decays for $\varepsilon > 0$. In the wide container both cases coincide within error for $\varepsilon < 0$, showing that the discrepancy between both cases in the small container is indeed a size-effect. S_m again loses significance for $\varepsilon > 0$, and the behaviour is erratic due to metastability of the transient region in the wide systems.

DYNAMICS OF TRANSIENT STATES

The buoyancy-driven convective state may present complex time evolutions. These are heavily dependent on the l_x/λ_c ratio, based on the constraint that the number of convective rolls has to be an integer number. Half-integer values are possible only with solid wall boundary conditions. This implies that non-integer values of l_x/λ_c lead to metastable states, as the number of convective cells n_c presents intermittent behaviour between the two closest values of k_c , as also between convection rolls at different sides of the container, if walls are present. As an example, Figure 4.9a shows the temporal evolution of $n(x)$ for a system with $l_x = 80$, that is, $l_x/\lambda_c^* \approx 1.6$. For a value of ω just after the transition point, the convective cell constantly switches between metastable states; it is possible to identify two-rolls and one-roll configurations at either side of the system, alternating with no clear periodicity. We believe this to be an important factor to take into account on any study of the dynamics of the granular convective state: the size of the container has no influence on the critical point of the transition, but plays a determining role in the dynamics. In our case, l_x for the narrow and wide containers was chosen a posteriori to diminish the effects of metastability, considerably facilitating the study of precursor states.

As l_x/λ_c is increased further, a new state becomes possible at the transition region in which convective cells coexist with regions effectively in the Leidenfrost state. Figure 4.9b shows a period of coexistence, as two pair of convective cells emerge in a confined region of the system while the rest remains in the Leidenfrost state. Notice how the Leidenfrost region is roughly $200d$ wide, far larger than λ_c^* . We interpret this phenomena as the emergence of a localized state in a non-linear system, a subject of increased scientific interest [159].

CRITICAL MODE AMPLITUDE

It has been shown that both the correlation of the fluctuating velocity field and the unstable mode of the density fluctuations present critical-like behaviour near the transition. We now look at the overall transition behaviour in the context of bifurcation theory, by following the amplitude in the emergent pattern of the critical mode, A_c . The emergent pattern is more evident and measured from the vertical velocity field $v_z(x, t)$. A_c is the amplitude of the mode k_c in $v_z(x, t)/\omega$, with k_c determined by

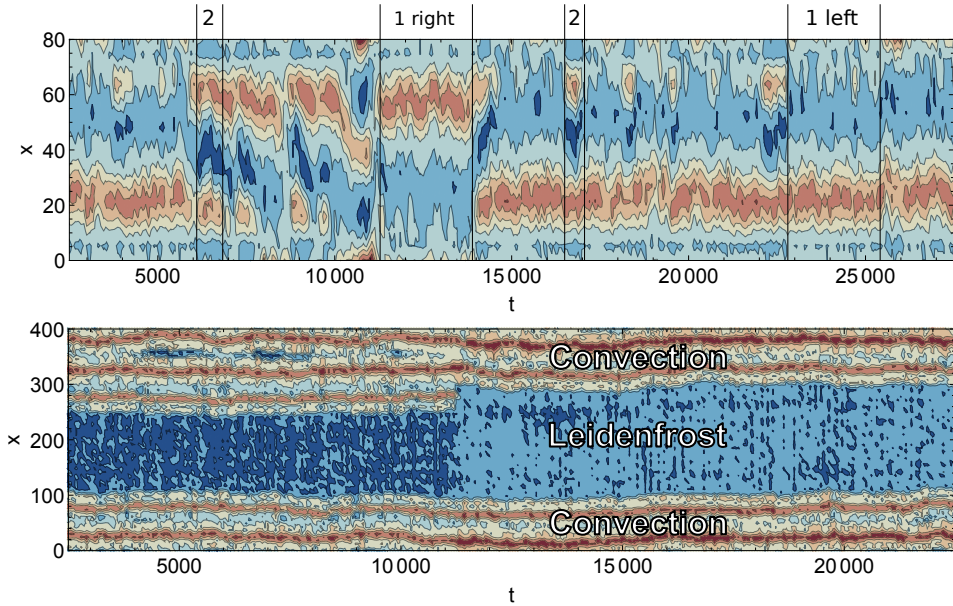


Figure 4.9: Spatio-temporal density plot of the number of particles field, $n(x,t)$, for $l_x = 80$, $\omega = 35$ and SBC (left) and $l_x = 400$, $\omega = 35$ and PBC (right). High density regions are shown in red.

the structure factor maximum. The final value of $\langle A_c \rangle_t$ is obtained by averaging over the whole simulation time.

In the seminal work of Swift and Hohenberg, hydrodynamic fluctuations were studied for a molecular fluid near the thermal convection instability [160], and a simple model for the Rayleigh-Bénard instability was derived. In the following we apply the Swift-Hohenberg model to the LBC transition, inspired by the evident similarities of both phenomena; in terms of bifurcation theory, both transitions correspond to spatial-mode selecting bifurcations. Nevertheless, we expect the discrete nature of our granular system to have a considerable effect close to the transition, manifested as fluctuations arising from the finite number of particles. Thus, we consider that the universal behaviour of the fluctuating vertical velocity $w(z,t) = v_z(x,t) - \langle v_z(x,t) \rangle_t$ close to the transition is given by the Swift-Hohenberg model for pattern formation with an stochastic term [144],

$$\partial_t w = \varepsilon' w - w^3 - (\partial_{xx} + k_c^2)^2 w + \sqrt{\eta'} \zeta(x,t), \quad (4.4)$$

with the control parameter ε' , and the bifurcation parameter given by $\varepsilon' - k_c^4$. In our system $\varepsilon' - k_c^4 \approx \varepsilon$ (as $k_c \ll 1$), and thus in what follows we take $\varepsilon' = \varepsilon$. Fluctuations are modelled by the last term, where ζ is a Gaussian white noise, that is $\langle \zeta(x,t) \zeta(x',t') \rangle = \delta(x-x') \delta(t-t')$; and η' is the parameter of noise intensity [161]. In our system the

zero correlation of ζ is justified by assuming the gaseous phase close to the moving plate to be the main source of fluctuations, and to behave strictly as an ideal gas, that is, lacking temporal or spatial correlations of the particles.

It is known that in (4.4) the base state $w(x, t) = 0$ is stable for $\varepsilon' < 0$, and presents a supercritical spatial instability for $\varepsilon' = 0$, which leads to the appearance of a pattern, in our case corresponding to convective cells, for $\varepsilon' > 0$. Following [161, 36], and confirmed by our measured velocity profiles, solutions for the critical mode k_c can be assumed to be of the form

$$w = \frac{a(\tau)}{\sqrt{3}} e^{ik_c x} + \frac{\bar{a}(\tau)}{\sqrt{3}} e^{-ik_c x} + U(a, \bar{a}, x) \quad (4.5)$$

with a the amplitude of the pattern with mode k_c , dependent on the slow time $\tau \equiv \varepsilon t$, and U a general function containing higher order terms in a . Substituting (4.5) into (4.4) one reaches the amplitude equation corresponding to a stochastic cubic supercritical spatial bifurcation:

$$\partial_\tau a = \varepsilon a - |a|^2 a + \sqrt{\eta} \zeta(\tau) \quad (4.6)$$

with $\eta \equiv 3\eta'$. A solution for the probability function of a , $P_s(|a|, \varepsilon, \eta)$, can be found from (4.4) and (4.5), as shown in [161, 36]. From the shape of P_s the expectation value can be obtained [161], given by

$$|a_{\max}| = \sqrt{\frac{\varepsilon + \sqrt{\varepsilon^2 + 2\eta}}{2}}. \quad (4.7)$$

In our case $|a_{\max}| = \langle A_c \rangle_t$. Our measurements are consistent with this form for $|\varepsilon| \ll 1$, as shown in Fig 4.10 for narrow and wide systems with PBC and EBC. The best agreement is found for noise intensity $\eta = 10^{-4}$, a free parameter. Nevertheless, (4.7) does not capture the shape of $\langle A_c \rangle_t(\varepsilon)$ for higher values of ε , deviating considerably already for $\varepsilon \sim 0.05$.

A higher level of agreement can be obtained by considering an stochastic quintic supercritical bifurcation [36]:

$$\partial_\tau a = \varepsilon a - |a|^4 a + \sqrt{\eta} \sqrt{h} \zeta(\tau), \quad (4.8)$$

with h quantifying the strength of the quintic non-linear term [36]. This type of bifurcation may be more relevant for our system, as it has been previously associated with parametrically driven spatially extended systems, as Faraday patterns [151] and vertically vibrated series of coupled pendula [152]. The former can be considered closer to our present system than the Rayleigh-Bénard scenario, taking into account that the bed of grains is also a vertically vibrated medium with a free surface. The latter case, on the other hand, could be related to the already mentioned low-frequency oscillations [123]. Previously it was shown that density inverted granular

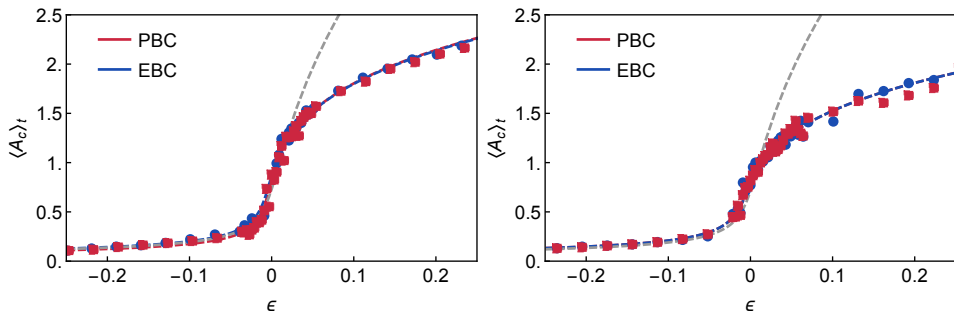


Figure 4.10: Amplitude of the critical pattern of the vertical velocity field $v_z(x, t)$, A_c , as a function of the bifurcation parameter ϵ , for EBC (blue) and PBC (red) in narrow (left) and large (right) containers. The grey dashed lines correspond to fits given by the Swift-Hohenberg model with a stochastic term (see main text), with noise level $\eta = 10^{-4}$. The coloured dashed lines correspond to fits based on a quintic supercritical bifurcation, for noise intensity $\sigma = 8 \times 10^{-4}$ in the small container systems, and $\sigma = 10^{-3}$ for the wide cases.

states in a quasi-one-dimensional container ($\tilde{l}_x \sim \tilde{l}_y \sim d$) behave approximately as harmonic oscillators. It can thus be inferred that for wider containers, as the ones considered in this study, the dynamics are analogous to a series of coupled oscillators.

Following a similar method as the previous analysis, an expression for the expected value of the amplitude of the unstable mode can be obtained (for details of the derivation we again refer the reader to [36]),

$$|a_{\max}| = \sigma^{1/6} \sqrt{\beta/\Omega + \Omega/3} \quad (4.9)$$

with $\Omega \equiv (3/4)^{1/3} (9 + \sqrt{3(27 - 16\beta^3)})^{1/3}$ and $\beta \equiv \epsilon/\sigma^{2/3}$, with $\sigma \equiv \eta\sqrt{h}$ the only fitting parameter. The shape of (4.9) is also shown in Figure 4.10, now in good agreement for higher ϵ in all cases.

All systems present the same overall shape of $A_c(\epsilon)$, with the most significant difference being lower amplitudes for $\epsilon > 0$ in the wide containers. More importantly, there is no significant difference in the noise intensity for all cases, except for the narrow container with EBC, where the noise term is lower, $\sigma = 6 \times 10^{-4} \pm 10^{-5}$. In the narrow container with PBC $\sigma = 8 \times 10^{-4} \pm 2 \times 10^{-4}$, and $\sigma = 10^{-3} \pm 2 \times 10^{-4}$ for the wide container with any boundary condition. The independence of the noise intensity on N suggests that the relevant quantity for the critical dynamics is the amount of particles per surface area, which in our cases remains constant.

4.4 CONCLUSIONS

We have studied the granular Leidenfrost to buoyancy-driven convection transition, characterized the precursor states and proposed a new interpretation of its universal dynamical behaviour. The overall picture is of a continuously fluidized bed of grains which goes from homogeneous Leidenfrost configurations to increasingly velocity correlated convective states, until flows are strong enough to sustain the density inhomogeneous buoyancy-driven convective state. From a bifurcation theory perspective, the convection transition can be understood as a pattern formation phase-transition, with the emergence of convective cells with a critical length-scale independent of the domain size, which is consistent with previously realized hydrodynamic stability analysis of the Leidenfrost state [80].

The time-dependent fluctuating convection state can be characterized by the correlation time of the fluctuating velocity field, which shows critical-like behaviour with an exponent of approximately 0.51. From the self-correlation it is also possible to observe the influence of low-frequency oscillations [123] in the fluctuating velocity field.

The static structure factor shows the emergence and growth of the pattern dominant length-scale. The amplitude of the critical mode is also seen to show critical behaviour, consistent with a supercritical bifurcation. By following the most unstable mode throughout the transition in wide systems it was possible to confirm that the size of the convective cells is indeed proportional to the frequency of energy injection.

In the transient state of wider systems the Leidenfrost and buoyancy-driven convective states can coexist. The convective state in this region is constantly evolving, presenting metastability between states with different number of rolls. As energy increases the stability of the convective cells increases, although their number is determined by the amount of cells that can be fitted in the container. Further increasing the energy leads to a comparatively slower process of merging of convective cells. The rich dynamics of merging and splitting of convective cells in coexistence with the Leidenfrost state in the wide systems calls for further research.

Elastic walls and periodic boundaries present the same critical points, disregarding any significant confinement effects for containers bigger than 50 particle diameters. Slightly dissipative side-walls, on the other hand, have the effect of decreasing the amount of energy needed to trigger the transition, showing that the excitation of the unstable mode at the boundaries has a more significant effect than the added dissipation. In the wide systems all boundary conditions become equivalent.

The amplitude of the critical mode of convection is seen to be coherent with a quintic supercritical amplitude equation. The agreement is much better than with a cubic supercritical bifurcation, associated with the Swift-Hohenberg equation. This suggests a new interpretation of the transition, closer to spatially extended parametrically driven systems than to Rayleigh-Bénard convection. We hypothesize that the

source of the parametric driving is not the vibration of the container (which has too low amplitude and high frequency to couple with the bed dynamics), but the low-frequency oscillations present in a density inverted bed of grains, i.e. the granular Leidenfrost state. In general, we remark that the universal behaviour of the density field can only be captured by considering a noise term in the corresponding amplitude equation which quantifies the finite-number effects. The noise intensity is seen to be independent on the system size, except in the confined small container. This suggests that the transition in wider systems is a local phenomenon, with the size of the critical convective cell as relevant length-scale. What factors determine the critical convective length-scale remains an open question. Furthermore, a derivation of the quintic supercritical amplitude equation from a series of coupled oscillators with the form proposed in [123] would be a way of confirming the proposed description.

ON CREATING MACROSCOPICALLY IDENTICAL GRANULAR SYSTEMS WITH DIFFERENT NUMBER OF PARTICLES¹

Granular hydrodynamics is known to successfully describe various complex granular flows. It is nevertheless unknown under which circumstances the continuum hypothesis holds for granular media. In the following chapter we investigate to what extent it is possible to create identical hydrodynamic states with significantly different number of particles, with the goal of studying density fluctuations in granular dynamics. A definition is given of macroscopically equivalent systems, and the dependency of the conservation equations with the particles' size is studied. In certain cases, and by appropriately scaling the microscopic variables, we are able to compare systems with significantly different number of particles that present the same macroscopic phenomenology. We use the found scaling laws in simulations of the density inverted granular Leidenfrost effect and its transition to a buoyancy-driven convective state, present in vertically vibrated setups. This allows us to quantify the effects that density fluctuations have in the collective oscillations that take place in the Leidenfrost state. The amplitude of the oscillations is deduced to be driven by density fluctuations, while their oscillation frequency converges to a finite value. Furthermore, the transition to buoyancy-driven convection is studied, showing a strong dependency on the particle size, although a possible convergence for large number of particles.

1. Draft for: N. Rivas, S. Luding, D. van der Meer, Europhysics Letters.

5.1 INTRODUCTION

Granular flows often show a remarkable similarity with those of molecular fluids [121, 111]. The success of granular hydrodynamic theories in predicting many complex granular behaviours indicates that such a relation is not only superficial [12, 13, 14, 28, 15, 16, 18]. But despite continued development, the defining properties of granular materials, such as the dissipative nature of the particles' interactions, still present a challenge for continuum theories, specially for high packing densities or dissipations [6, 7, 8]. An additional fundamental difficulty stems from the enormous difference in the total number of constituents between granular and molecular systems; while in granular media macroscopic fields may vary in distances of the order of a few particle diameters, in molecular systems the microscopic relevant length-scale is orders of magnitude smaller than the macroscopic one. The low number of constituents involved in granular flows immediately imply the existence of inherently large density fluctuations, which can drastically modify the global dynamics, specially near transitions [137, 34]. Deepening our understanding of the role played by these fluctuations is thus of fundamental importance for the development of a successful continuum description of granular media.

In the following chapter we study the possibility of constructing macroscopically identical granular systems with significantly different number of particles. The final goal is to analyse the influence of finite-number-driven fluctuations. Macroscopic states are defined by the set of conserved hydrodynamic fields, as determined by the granular hydrodynamics equations. The microscopic states, on the other hand, are given by the particles' positions and velocities, and evolve according to the particles' interaction laws. The link between the two scales is mediated by the grain properties, present in the transport coefficients on the macro scale, and in the collision rules in the microscopic scale. Moreover, boundary conditions usually relate effective hydrodynamic fields with microscopic attributes, such as dissipation coefficients or energy injection parameters. Using previously obtained expressions for the transport coefficients, we derive the dependency with particle size of all terms of the conservation laws. As the particle size is directly related to the total number of particles, we essentially see the dependency of the macroscopic states on the total number of particles of the system. We demonstrate that in general the granular hydrodynamic equations are not particle-size invariant. Nevertheless, we will show that it is possible to construct invariance in steady, no flux states, via carefully chosen scalings of the particles' properties and boundary conditions. The key difference from usual scaling analysis is that in our case a microscopic quantity (the size of the particles) is chosen as control parameter, and the rest of the microscopic variables are modified as a function of this control parameter such that the macroscopic description of the system remains invariant.

The obtained scaling relations are verified by simulations of the granular Leidenfrost state and its transition to buoyancy-driven convection. By computing the

coarse-grained fields of equivalent systems we are able to observe the influence of finite-number effects in the macroscopic scale. Fluctuations are seen to have a determinant effect on the oscillatory behaviour previously observed in the same setup, as also intermediate states driven mainly by fluctuations are seen to disappear in the hydrodynamic limit. The source of disagreements in non-steady states is also studied by increasing the energy injection and analysing the transition from the granular Leidenfrost state to a buoyancy-driven convective state. Although the scalings are not expected to be valid in non-steady states, the transition shows interesting dependencies as the number of particles is increased. Overall, we believe that the methodology presented in what follows could be applied to other granular systems, providing a clear way of studying intrinsic fluctuations driven by the number of particles, and finite-particle-size effects.

5.2 GRANULAR HYDRODYNAMICS PARTICLE-SIZE DEPENDENCIES

In the following we study the particle-size dependency of the two-dimensional granular hydrodynamic equations. The analysis is made for two dimensions mainly due to the simplicity and wider acceptance of the form of the constitutive laws, when compared to three dimensional ones. Our goal is to recreate equivalent hydrodynamic states with significantly different total number of particles N which, as will be proven, is equivalent to that of finding particle-size invariant states. Two hydrodynamic states are considered equivalent if the conserved macroscopic fields are the same in all space and time. As conserved fields we consider the packing fraction, $\phi(\vec{x}, t) = mn(\vec{x}, t)/\rho_p$, with m and $\rho_p = m/\pi(d/2)^2$ the mass and density of the particles, and $n(\vec{x}, t)$ the number density field, function of the spatial coordinates $\vec{x} = (x, y)$ (for two-dimensional systems) and the time t ; the velocity field $\vec{u}(\vec{x}, t)$; and the fluctuations in velocity, $k_B T(\vec{x}, t)/2m = \langle \vec{u}(\vec{x}, t) \rangle_t^2 - \langle \vec{u}(\vec{x}, t) \rangle_t^2$, with $T(\vec{x}, t)$ the granular temperature field, k_B the Boltzmann constant, and time averages denoted as $\langle \rangle_t$. The condition of invariance can then be expressed as

$$\phi_d(\vec{x}, t) = \phi_{d^*}(\vec{x}, t) \quad (5.1)$$

$$\vec{u}_d(\vec{x}, t) = \vec{u}_{d^*}(\vec{x}, t) \quad (5.2)$$

$$\frac{k_B T_d(\vec{x}, t)}{m_d} = \frac{k_B T_{d^*}(\vec{x}, t)}{m_{d^*}}, \quad (5.3)$$

for all \vec{x} , t , and particle diameters d and d^* , where the d -dependency has been denoted by a subscript.

From the definition of the packing fraction and its condition of invariance (5.1), one immediately obtains that $d^2 n_d(\vec{x}, t) = d^{*2} n_{d^*}(\vec{x}, t)$, which implies that

$$[n]_d = d^{-2}. \quad (5.4)$$

where we have introduced the notation for the dependency on d as square brackets, $[]_d$. It then follows that the number-density is indeed inversely proportional to

d and thus, if the total volume of the system is kept fixed, N also varies with d . That is, the problem of finding equivalent systems with different number of particles is equivalent to that of finding equivalent systems with different particles' size.

From the velocity fluctuations invariance (5.3), we see that k_B should scale as m in order for $T(\vec{x}, t)$ to be invariant. There is still freedom to choose the scaling of m , which we take as

$$[m]_d = d^2, \quad (5.5)$$

such that ρ_p remains invariant. This implies that the temperature field (in k_B units),

$$[k_B T(\vec{x}, t)]_d = d^2. \quad (5.6)$$

The subsequent step consists in investigating if such conditions over the conserved fields also imply invariance of their conservation laws. If both the conserved fields and their laws of evolution are invariant with respect to d , then the same hydrodynamic states are to be expected. As granular hydrodynamic model we consider the two-dimensional compressible Navier-Stokes equations, with an added sink term in the energy equation to account for particle dissipation:

$$m \left(\frac{\partial n}{\partial t} + \vec{u} \cdot \nabla n + n \nabla \cdot \vec{u} \right) = 0, \quad (5.7)$$

$$m n \left(\frac{\partial \vec{u}}{\partial t} + \vec{u} \cdot \nabla \vec{u} \right) = -\nabla p + \nabla \cdot (\mu \tau) + \nabla (\lambda \nabla \cdot \vec{u}) + m n \vec{g}, \quad (5.8)$$

$$n k_B \left(\frac{\partial T}{\partial t} + \vec{u} \cdot \nabla T \right) = \nabla \cdot \vec{J} - p (\nabla \cdot \vec{u}) - I. \quad (5.9)$$

They correspond to the mass conservation equation; the momentum balance equation, with p the pressure, μ the (shear) viscosity, $\tau = \nabla \vec{u} + (\nabla \vec{u})^T$ the strain rate tensor, λ the second viscosity and \vec{g} the acceleration of gravity; and the granular temperature equation, or energy balance, with J the energy-current density (or heat flux), and $-I$ the sink-density of energy. Here we have neglected terms which are quadratic in $\nabla \vec{u}$, particularly in the energy equation the terms $\mu \nabla \vec{u} : \tau$ and $-\mu \nabla \vec{u} : (\nabla \cdot \vec{u})$.

In order for (5.7)-(5.9) to be d -invariant, i.e. independent of the size (and total number) of particles, all terms of any equation should have the same dependency on d . Notice that this is true for the continuity equation just by construction, considering (5.2), (5.4) and (5.5). For the momentum and temperature equations a explicit form of the transport coefficients is needed, as p , μ , \vec{J} and λ , as also the energy sink term, I , are expected to explicitly depend on d . Various forms for these quantities can be found in the literature, varying in ranges of validity and levels of approximations. Here we consider the expressions derived in [26] using the Chapman-Enskog method to solve the Boltzmann kinetic equation. These expressions are known to be useful in describing open vibrated granular systems under the influence of gravity [22], given by the same set of conservation equations (5.7)-(5.9). Nevertheless, we

remark that leading order scalings on d and r are expected to be independent of the particular form of the transport coefficients.

It follows from the definitions (5.1) and (5.2) that the left side of the momentum equation is invariant in d . For the pressure we consider, as a first order approximation, the equation of state of an ideal gas, $p = nk_B T$. Notice then that, by (5.3) and (5.4),

$$[p]_d = d^0. \quad (5.10)$$

Higher order corrections to the equation of state are expected to depend on the packing fraction ϕ , which is itself independent of d , and thus $[p]_d$ is not expected to be modified.

The viscosity μ is equivalent to that given by a system of elastic hard-spheres times corrections due to particle-particle dissipative interactions,

$$\mu = \mu_0(T)\mu^*(r) = \frac{1}{2d\sqrt{\pi}} (mk_B T)^{1/2} \mu^*(r). \quad (5.11)$$

The specific form of $\mu^*(r)$ can be found in [22]; here we only remark that, as expected, $\mu^*(r) = 1$ as $r \rightarrow 1$. Considering (5.3) and (5.5), (5.11) results in

$$[\mu]_d = d, \quad (5.12)$$

where we have assumed that $[r]_d = d^0$, and thus $[\mu^*(r)]_d = d^0$. Further along we will elaborate on the consequences of relaxing this condition.

The second viscosity can be immediately obtained by using the Stokes approximation $\lambda = -\frac{2}{3}\mu$. In that case

$$[\lambda]_d = d. \quad (5.13)$$

Finally, for the gravity term we choose $[\vec{g}]_d = d^0$, and thus the last term in (5.8) becomes d -invariant.

We now consider the terms in the energy equation (5.9). As expected, the left-hand side terms of (5.9) are independent on d , as can be readily seen from (5.5) and (5.6). Furthermore, the second term on the right-hand side of (5.9) is also d -invariant, as it follows directly from (5.2) and (5.10). For the energy-density flux we consider Fourier's heat law,

$$\vec{J} = \kappa k_B \nabla T. \quad (5.14)$$

with κ the coefficient of thermal conductivity. As derived in [22], the form is analogous to that of μ ,

$$\kappa = \kappa_0(T)\kappa^*(r) = \frac{2}{d\sqrt{\pi}} \left(\frac{k_B T}{m} \right)^{1/2} \kappa^*(r). \quad (5.15)$$

which results in

$$[\kappa]_d = d^{-1}, \quad (5.16)$$

where, as before, we have considered $[\kappa^*(r)]_d = d^0$.

The last term in (5.9) quantifies the loss of energy due to the inelastic interaction between particles. According to [22],

$$I = pnk_B T \frac{I^*(r)}{\mu_0(T)}, \quad (5.17)$$

where $I^*(r)$ is a function only of r . Considering (5.10) and (5.12), we see that

$$[I]_d = d^{-1}. \quad (5.18)$$

Summarizing, all terms involving the transport coefficients κ , μ and λ scale as d , while the energy dissipation term I scales as d^{-1} , and the rest of the terms are d -invariant. It is important to remark that higher density corrections to the transport coefficients and the equation of state are expected to be functions of ϕ , and thus also d -invariant. This implies that (5.8) and (5.9) are not d -invariant, as not all terms scale in the same manner with d . In other words, it is not possible to obtain macroscopically equivalent systems for different number of particles in the most general dynamic case, considering the conservation laws given by (5.7)-(5.9). Even though the previously derived relations depend on the specific form of the transport coefficients, we expect all of them to present the same leading-order dependency on d , and thus the previous results to be valid for general granular flows.

Notice that in the limit of $d \rightarrow 0$ all d -dependent terms in (5.7)-(5.9) vanish, except for the dissipation density I , which diverges. This is to be expected, as if $n(\vec{x}, t)$ increases with $d \rightarrow 0$, and $nk_B T(\vec{x}, t)$ remains constant, the collision rate is expected to increase, and with it the total dissipation per volume. Nevertheless, the divergence can be avoided by considering a d -dependent coefficient of restitution. In the case that $[r]_d \neq d^0$, as we have seen, $[I]_d = d^{-1} [I^*(r)]_d$, $[\kappa]_d = d^{-1} [\kappa^*(r)]_d$ and $[\mu]_d = d [\mu^*(r)]_d$. The functions $\mu^*(r)$, $\kappa^*(r)$ and $I^*(r)$ can be expanded in terms of $\varepsilon \equiv 1 - r^2$ [22], which yields

$$\mu^* = 1 + \frac{157}{768} \varepsilon + O(\varepsilon^2), \quad (5.19)$$

$$\kappa^* = 1 + \frac{57}{256} \varepsilon + O(\varepsilon^2), \quad (5.20)$$

$$I^* = \frac{5}{12} \varepsilon - \frac{5}{512} \varepsilon^2 + O(\varepsilon^3). \quad (5.21)$$

We see that, to first order, $[I]_d = d^{-1} [\varepsilon]_d$. This implies that if ε is taken to be at least linear in d , then I does not diverge as $d \rightarrow 0$. As an example as to how to derive an scaling law for ε such that the equations remain invariant, let us consider the the no-flow ($\vec{v} = 0$) and steady state case, where equations (5.7)-(5.9) are reduced to

$$\nabla p = mn\vec{g} \quad (5.22)$$

$$\nabla \cdot \vec{J} = I. \quad (5.23)$$

The invariance of the first equation follows from the condition (5.1) and (5.10). The second equation is not directly d -invariant, as it follows from (5.16) and (5.18). In order to balance $\nabla \cdot \vec{J}$ and I , then

$$[\varepsilon]_d = d^2. \quad (5.24)$$

That is, in the case that the resitution coefficient is modified according to (5.24), equations (5.22)-(5.23) are d -invariant. Fruthermore, in the limit $d \rightarrow 0$, equations (5.7)-(5.9) result in

$$m \left(\frac{\partial n}{\partial t} + \vec{u} \cdot \nabla n + n \nabla \cdot \vec{u} \right) = 0, \quad (5.25)$$

$$m n \left(\frac{\partial \vec{u}}{\partial t} + \vec{u} \cdot \nabla \vec{u} \right) = -\nabla p + m n \vec{g}, \quad (5.26)$$

$$n k_B \left(\frac{\partial T}{\partial t} + \vec{u} \cdot \nabla T \right) = -p(\nabla \cdot \vec{u}). \quad (5.27)$$

which correspond to the equations of a perfect fluid. The resulting equations (5.25)-(5.27) tell us that the macroscopic state of any granular flow is expected to converge as $d \rightarrow 0$, behaving like a perfect fluid, given that $[\varepsilon]_d = d^\alpha$ with $\alpha > 1$.

Having explored the possibility of obtaining macroscopically identical systems with different d or, what is equivalent, N , we now consider a specific granular flow in which the relations can be tested. Even though we have proven that d -invariance is not possible in the most general flow case, the convergence to given macroscopic states of both steady and unsteady flows is studied.

5.3 GRANULAR LEIDENFROST SYSTEM

As test case we consider the granular Leidenfrost state and its transition to buoyancy-driven convection. The granular Leidenfrost state consists of a density inverted and phase separated particle arrangement, where a high temperature, gaseous region near the vibrating bottom sustains a denser, colder bed of grains on top [79, 71]. As the granular Leidenfrost state corresponds to a steady state with no flow, it is expected to be described by (5.22) and (5.23) (with appropriate excluded volume corrections) [79], the case where we have seen that it is possible to construct d -invariance. Nevertheless, as the shaking strength is increased, the granular Leidenfrost state loses its horizontal homogeneity and gives rise to a buoyancy-driven convective state, still a steady state but with $\vec{v} \neq 0$. Granular hydrodynamics was recently proven accurate in predicting the critical modes of this transition [80], confirming its validity for this particular state.

BOUNDARY CONDITIONS

In order for the macroscopic system to be completely defined only the set of boundary conditions rests to be determined. To account for the energy injection through particle-wall collisions (5.23) is integrated over the whole domain, resulting in

$$J_{\text{in}} = \int_0^h I dz, \quad (5.28)$$

where h is the height of the granular bed, and J_{in} the energy-density flux injected to the system through particle collisions with the bottom boundary. We have accounted for the free top boundary by taking $J(z) \rightarrow 0$ as $z \rightarrow \infty$. Notice that as particles have no friction and walls are considered elastic, collisions with the side walls do not inject energy. For the specific form of J_{in} we consider a saw-tooth driving, which leads to

$$J_{\text{in}} = m n(0) u^3 \left(\frac{2k_B T(0)}{m u^2} \right)^{1/2} \quad (5.29)$$

with u the typical velocity of the bottom plate. Even though more complex expressions exist for driving forms closer to sinusoidal functions, it can be shown that all of them converge to (5.29) in the limit of $u \ll \sqrt{T(z=0)}$, which is expected to be valid in the highly agitated granular Leidenfrost state. Therefore, using our previously derived scalings, and imposing that $[h]_d = d^0$, it is straightforward to see that, by (5.28),

$$[u^2]_d = d. \quad (5.30)$$

If the container's shaking is taken to have a characteristic amplitude A_f and angular frequency ω_f , then $u = A_f \omega_f$, and thus $[A_f \omega_f]_d = d^{1/2}$. In our case we use $[A_f]_d = d$, to make sure that the amplitude does not become larger than the particle size in the limit $d \rightarrow 0$. It then follows that

$$[\omega_f]_d = d^{-1/2}. \quad (5.31)$$

As mentioned previously, the total number of particles N is expected to be d -dependent, from (5.4), as long as the total volume is not adequately scaled. The total number of particles is given by

$$N = \int_{\Omega} n(\vec{x}) d\Omega \quad (5.32)$$

where Ω is the domain defined by the particles' container. If the domain is not scaled with the particles' size, $[\Omega]_d = d^0$, then $[N]_d = d^{-2}$. Nevertheless, keeping the size of the container fixed could lead to different macroscopic states, as confined states are expected to change their phenomenology as spatial restrictions are relaxed.

It is then more adequate to maintain the effective dimensionality of the system \mathcal{D}_e independent of d , in which case $[d\Omega]_d = d^{\mathcal{D}-\mathcal{D}_e}$, and thus

$$[N]_d = d^{-\mathcal{D}_e}. \quad (5.33)$$

For example, in the quasi-two-dimensional geometries usually considered in studies of the granular Leidenfrost state, $\mathcal{D}_e = 2$, implying $[N]_d = d^{-2}$.

DIMENSIONLESS QUANTITIES

Several dimensionless numbers are known to be relevant in the dynamics of the granular Leidenfrost state, as also in the transition to buoyancy-driven convection. In the following we derive how do this quantities scale with d . The amount of particles is correctly quantified independent of the systems size by the number of filling layers $F \equiv N/l_x l_y$. Its scaling is observed to be independent of the number of constrained dimensions,

$$[F]_d = d^{-1}. \quad (5.34)$$

The shaking strength $S_f \equiv A_f^2 \omega_f^2 / g d$ is known to be a good control parameter for the transition to buoyancy-driven convection, as it remains roughly constant for different combinations of A_f and ω_f [71]. It follows from (5.30) that

$$[S_f]_d = d^0. \quad (5.35)$$

Finally, the Prandtl number, which quantifies the relative importance of diffusive momentum to energy transfer, $\text{Pr} \equiv \mu/\kappa$, is known to play an important role in the convective dynamics [80]. From (5.12) and (5.16),

$$[\text{Pr}]_d = d^0. \quad (5.36)$$

The invariance of Pr on the particle size implies that the convective dynamics (where $\vec{v} \neq 0$ and thus the conservation laws are not expected to be d -invariant) could retain certain characteristics as d is scaled. In other terms, the differences observed in systems with different d cannot be attributed to variations in the relative importance of viscosity to thermal diffusivity.

5.4 SIMULATIONS

Numerical simulations are performed using an event-driven discrete particle method algorithm [162]. The same algorithm has previously presented excellent agreement with experiments of the granular Leidenfrost state [123] (see Chapter 3). The container as a whole is vibrated in the z -direction, such that the position of the base is given by $z_0(t) = A_f \sin(\omega_f t)$, with A_f and ω_f the amplitude and angular frequency

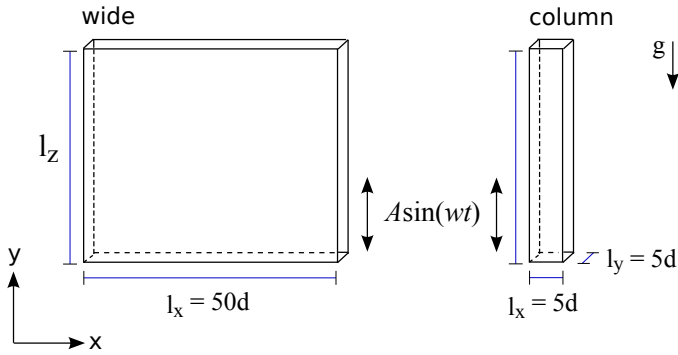


Figure 5.1: The two container geometries studied: *wide*, with $l_x = 50$ and *column*, with $l_x = 5$, while $l_y = 5$ in both cases.

of oscillation, respectively. The sinusoidal function is actually implemented as a bi-parabolic function, as it significantly simplifies the numerics. Previous simulational results using the same algorithm have been tested against the use of an actual sine function, and no relevant differences were observed, aside from the significantly higher computational cost [123]. Furthermore, in order to avoid inelastic collapse we set $r = 1$ if the relative velocity of the particles involved in a collision is less than $10^{-10} \sqrt{dg}$ [87]. We use this particularly low value to avoid any significant influence as $r \rightarrow 1$ or, equivalently, $d \rightarrow 0$.

Two different geometries are studied, shown in Figure 5.1: a wide container, where the base's width (l_x) is much larger than the depth (l_y), and a column container, where $l_x = l_y \sim d$, making the system effectively quasi-one-dimensional. The height of the container is irrelevant, as there is no top lid and side walls are taken to be infinitely tall. Particles are considered perfectly hard, smooth, monodisperse and spherical. Rotational degrees of freedom are disregarded in order to be as close as possible to the theoretical description. For the same reason particle-wall collisions are considered to be perfectly elastic, and thus dissipation only occurs due to particle-particle collisions.

Microscopic systems are determined by 7 physical parameters, all of them functions of d , as given by the scalings previously derived. In order to produce equivalent systems a reference one must be defined, which we take to be the unitary case where $d = 1$. Systems are referred to as

$$\mathbb{S}_d \equiv \{d; N, l_x, l_y, r, \omega_f, A_f\}. \quad (5.37)$$

For simplicity, we use the notation $\xi_{d^*} \equiv \xi(d = d^*)$ for any variable ξ .

In the column geometry $l_{x,1} = l_{y,1} = 5d$, that is, we scale the base with the size of the particles, which implies, from (5.33), $[N]_d = d^{-1}$. Furthermore, we take $\omega_{f,1} = 30\sqrt{g/d_1} = 30$. On the other hand, in the wide container we consider $l_{x,1} = 50$

(fixed), implying that $[N]_d = d^{-2}$, and $\omega_{f,1}$ becomes an additional control parameter, as we want to vary the energy injection to study the transition to buoyancy-driven convection. All other parameters between the two containers remain the same. Following the theoretical analysis, we scale the amplitude proportional to d , $A_f = 0.1d$, and thus $A_{f,1} = 0.1$. The small prefactor is chosen so as to minimize the spatial inhomogeneities induced by higher oscillation amplitudes, and thus approach the limit of an effective fixed temperature boundary condition [163]. Finally, two reference particle-particle coefficients of restitutions will be considered, $r_1 = 0.9$ and $r_1 = 0.99$, referred to as dissipative and quasi-elastic systems, respectively. As we want to compare systems with similar packing fractions, in the quasi-elastic system we consider a higher number of particles, so that $F_1 = 12$ and $F_1^e = 32$.

Particle sizes are varied over two orders of magnitude. The higher limit is set by the scalings: taking as reference \mathbb{S}_1 , r becomes negative for $d = d_1(1 - r_1^2)^{-1/2} \approx 2.3$. The upper limit, on the other hand, is set by the computational capacity. The lowest particle size considered is $d = 1/16$; notice that in the wide case, $N_{1/16} \sim 8 \times 10^5$, a significant number of particles that have to be simulated for long times—due to transient behaviours close to the transition points—, and at very high ω_f . It then becomes of fundamental importance to use an event-driven algorithm, due to its superior speed compared to constant time-stepping approaches.

Macroscopic fields are obtained by binning the container in the vertical direction, with bins of constant size 1, and then time-averaging for at least $t_f = 10^5 \sqrt{d/g}$. We set a limiting time in terms of the gravity given time-scale rather than in terms of the period of oscillation of the base, as for higher frequencies we expect the latter to lose any significance, as the dynamics of the system essentially decouple from the period of the base vibration. These values were selected after observing no significant differences for higher spatial resolutions or longer time windows, although due to the nature of the transition from Leidenfrost to convective states, finite times will always truncate the ideal results. Horizontally homogeneous directions were ignored after verifying that they remain homogeneous in all cases. Thus, in the column case all macroscopic fields are essentially one-dimensional in \hat{z} , while in the wide case the \hat{x} direction is also considered.

COLUMN CONTAINER

In the column container the transition towards the buoyancy-driven convective state is frustrated due to the strict confinement, allowing us to study the dynamics of the Leidenfrost state for high energy inputs. It thus becomes possible to easily observe collective quasi-periodic oscillations of the bed, referred to as low-frequency oscillations (LFOs) [123] (see Chapter 2), due to their characteristic period being orders of magnitude lower than the containers' shaking period. In the following we study the response of such oscillations to the variation of N in macroscopically equivalent systems.

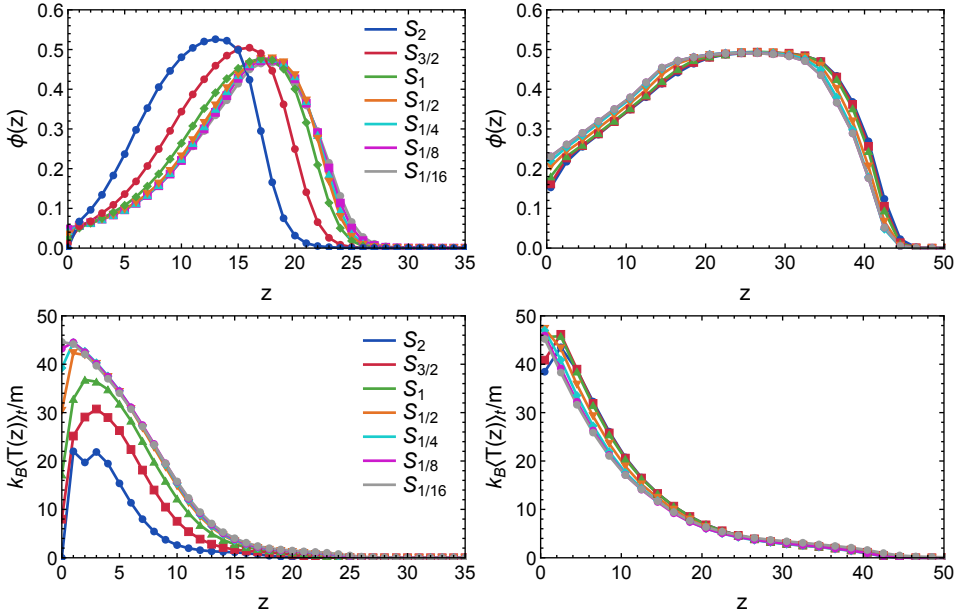


Figure 5.2: Time-averaged vertical packing fraction profiles $\langle \phi(z) \rangle_t$ and temperature profiles $k_B \langle T(z) \rangle_t / m$, for systems shown in the dissipative ($\varepsilon_1 = 0.9$, left) and quasi-elastic ($\varepsilon_1 = 0.99$, right) cases.

The macroscopic states are seen to converge as $d \rightarrow 0$ in the column container. Vertical profiles of the time-averaged packing fraction $\langle \phi(z) \rangle_t$ and the fluctuating velocity $k_B \langle T(z) \rangle_t / m$ are shown in Figure 5.2 for several different S_d . The characteristics of the Leidenfrost state can be readily recognized: low density, high temperature regions near the bottom, below high density, low temperature regions [80]. As $d \rightarrow 0$ the fields are seen to converge to a given d -independent state. The ratio of packing fractions in both regions increases as d decreases, as $\phi(z)$ in the gaseous regions goes from an almost linear increase to a concave curve. It is the gaseous regions that presents the most significant differences with d , although the maximum of $\langle \phi(z) \rangle_t$ also decreases slightly. Variations in the gaseous region are also significant in $\langle T(z) \rangle_t$, which presents a twofold increase as $d \rightarrow 0$, accompanied by an overall increase of the total temperature T_t .

The qualitative aspects of $\langle \phi(z) \rangle_t$ and $\langle T(z) \rangle_t / d$ suggest two sources of disagreement due to finite-size effects. The first one stems from the influence of d on the boundary layers, as the free-volume near solid walls is proportional to d , just due to geometrical factors. This is an effect which cannot be captured by the considered continuum description, but it is expected to become negligible as $d \rightarrow 0$, as the deviations of $\phi(z=0)$ suggest (see Figure 5.2). Secondly, larger particles can lead to

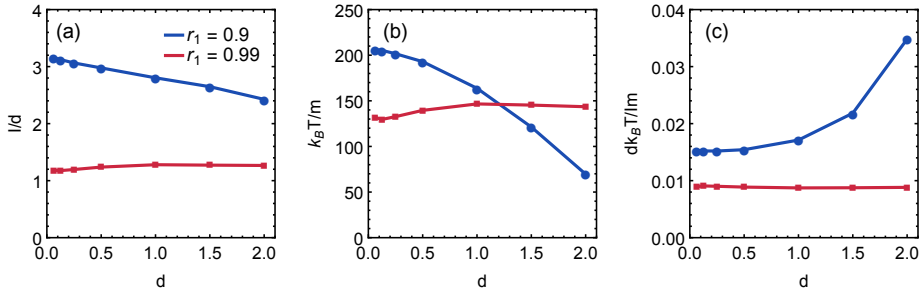


Figure 5.3: (a) Total energy-density dissipation per time normalized by d , I_d/d , for dissipative (blue) and quasi-elastic (red) systems. (b) Total granular temperature per mass $k_B T_t/m$ for the same systems as in (a). (c) Ratio of the two previous quantities, $dk_B T_t/mI_d$.

conflicts between micro- and macroscopic length-scales; notice that in the convergent fields $\langle \phi(z) \rangle_t$, the height of the gaseous region $h_g \approx 10$. That corresponds to $h_g = 5d_2$, and thus an uncorrelated gaseous behaviour can hardly be expected. On the other hand, for $\mathbb{S}_{1/2}$, where the vertical profile is already similar to systems with even lower values of d , $h_g = 20d_{1/2}$.

Beyond finite-size effects, the value of the coefficient of restitution is expected to have a significant influence, as the scalings were derived in the $r \rightarrow 1$ limit. Indeed, quasi-elastic systems show a much higher agreement as d is varied, as shown in Figure 5.2 for $\langle \phi(z) \rangle_t$ and $k_B \langle T(z) \rangle_t/m$. The most significant differences are again observed near $z = 0$, suggesting that these are indeed finite-size, boundary-layer effects.

The convergence of the conserved fields $\langle \phi(z) \rangle_t$ and $\langle k_B T(z)/m \rangle_t$ as $d \rightarrow 0$ suggests that the found scalings do lead to macroscopically equivalent systems with different number of particles. We observe $\sim 5\%$ differences in the macroscopic fields of systems with one order of magnitude difference in N . Interestingly, it is now possible to determine at which point one can expect N -independent states. For dissipative systems, we see a significant change of the convergence rate for $d < 1/4$, which corresponds to $N = 1200$. At this point deviations from an extrapolated limit case are on the 1% range. A comparison with the actual solution of the hydrodynamic equations in this geometry, at this limit, would allow us to see until what extent hard-particle simulations are actually solving the hydrodynamic equations; work is currently being done in this direction (see Chapter 6).

After having studied the convergence of the macroscopic fields, we now turn our attention to how particular quantities vary as N increases. Equation (5.23) predicted that the total energy dissipated per unit time and volume I scales linearly with d . Measurements from simulations show considerable deviations from this linearity, as shown in Figure 5.3a. In dissipative systems deviations are of the order of

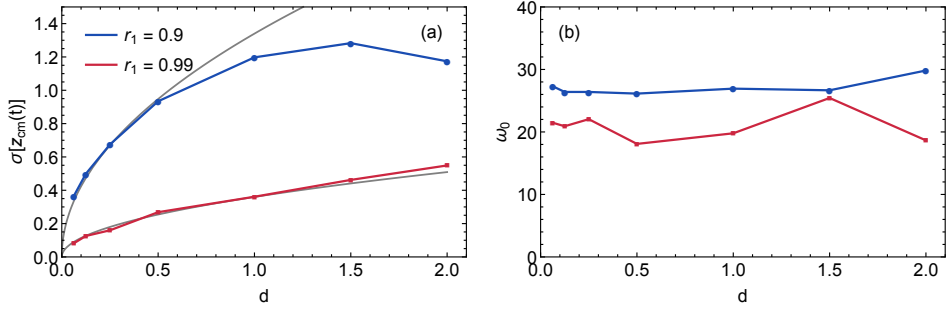


Figure 5.4: (a) Amplitude of the low-frequency oscillations a_0 , defined as the standard deviation of the centre of mass $\sigma(z_{cm}(t))$, for equivalent \mathbb{S}_d . In gray, square root fits. (b) Frequency of oscillation of the column, ω_0 , for the same systems as in (a).

$\sim 20\%$, while in quasi-elastic system it improves considerably to $\sim 5\%$. The improvement for higher r suggests that the deviations stem from neglecting higher order ε dependencies of the transports coefficients. In dissipative systems an almost linear increase of $d \rightarrow 0$ can be observed, suggesting that the coefficient of restitution is being overestimated or, analogously, that ω_f should be higher.

Deviations from the expected constant behaviour of the total temperature per mass, $k_B T_t/m$, are even stronger, specially in the dissipative case, as shown in Figure 5.3b. Again, the quasi-elastic case shows a significant improvement. Interestingly, for both I/d and $k_B T_t/m$ the behaviour with d changes between dissipative and quasi-elastic systems: in the former case quantities increase as $d \rightarrow 0$, while in the later they decrease until $d = 1/4$, after which their behaviour cannot be extrapolated by our data. Convergence to a macroscopic state even when the individual scaling relations derived for an invariant no-flux, one-dimensional steady state ((5.22), (5.23)) are seen to deviate can be explained by the convergence of all systems to the ideal fluid case.

LOW-FREQUENCY OSCILLATIONS

Low-frequency oscillations are clearly identifiable in the column geometry for all \mathbb{S}_d , making it possible to study their properties in equivalent macroscopic systems with different N . Remarkably, their characteristic amplitude, quantified by the standard deviation of the evolution of the vertical centre of mass, $a_0 \equiv \sigma(z_{cm}(t))$, is seen to be proportional to $d^{1/2}$, as shown in Figure 5.4a. On the other hand, the characteristic frequency ω_0 , obtained from the fast Fourier transform of $z_{cm}(t)$, shows a roughly constant behaviour with d , as shown in Figure 5.4b. This $[\omega_0]_d = d^0$ behaviour is in accordance with a previously derived theoretical expression [123] (see Chapter 2). A first approximation of the frequency of oscillation of the granular bed was obtained

by considering general conservation laws for a continuum medium and taking a first-order approximation of the density inverted profile. Disregarding higher order effects, the movement of the bed was shown to be equivalent to a forced harmonic oscillator, with characteristic frequency

$$\omega_0^t = \frac{g\rho_g}{m_s}, \quad (5.38)$$

with ρ_g the density of the gaseous region and m_s the total mass of the solid region. This expression has been found to be in good agreement with both simulations and experiments, specially in the high energy injection limit [123, 158] (see Chapters 2 and 3). In our case, as $\phi(z)$ converges for $d \rightarrow 0$, ω_0^t is expected to become d -invariant, as both ρ_g and m_s are macroscopic quantities determined by $\phi(z)$.

From the decrease of a_0 as $d \rightarrow 0$ we can conclude that, in the limit of $d \rightarrow 0$, LFOs would be unmeasurable, making it an essentially finite-size (granular) phenomena. Moreover, for d small enough, the behaviour of $a_0(d)$ is consistent with a \sqrt{N} law, suggesting that low-frequency oscillations are driven by intrinsic fluctuations due to the low number of particles in the system. As N decreases, the relative strength of the momentum fluctuations given by particles of the gaseous phase hitting the solid/fluid phase increases, and as such the amplitude of the oscillations are bigger. On the contrary, for smaller d , a significant amount of particles in the gaseous phase would have to transfer momentum to the solid phase at the same time to have an equivalent impact, a situation that becomes increasingly improbable as N increases.

It is interesting to notice that even though the amplitude of LFOs becomes negligible, the unstable mode is still present in the macroscopic system, as the $[\omega_0]_d = d^0$ behaviour shows. This further suggests that the unstable mode is an intrinsic characteristic of density inverted states, as argued in [123]. The situation is curious, as the unstable mode is a macroscopic phenomena, but its amplitude is driven by microscopic effects. Furthermore, the evolution of $z_{cm}(t)$ is seen to become less chaotic and closer to a harmonic oscillation with a clearly defined frequency as $d \rightarrow 0$, as increasingly steep peaks in the Fourier transforms show. This is another sign that low-frequency oscillations are governed by intrinsic finite-number fluctuations.

WIDE CONTAINER

In the wide container, as energy injection is increased, the Leidenfrost state eventually loses its stability and gives rise to a buoyancy-driven convective state. Convective flows were not observed in the column container due to the important geometrical constraint. In the following section we study the transition for different \mathbb{S} , while varying $\omega_{f,1}$, now an additional control parameter. All other parameters and the scalings are the same as in the column container, although notice that l_x is now independent of d , and thus $N_d = N_1(d_1/d)^2$.

The convective state is also a steady state although with non zero velocity, in contrast with the Leidenfrost state. This motivates the use of the velocity field for

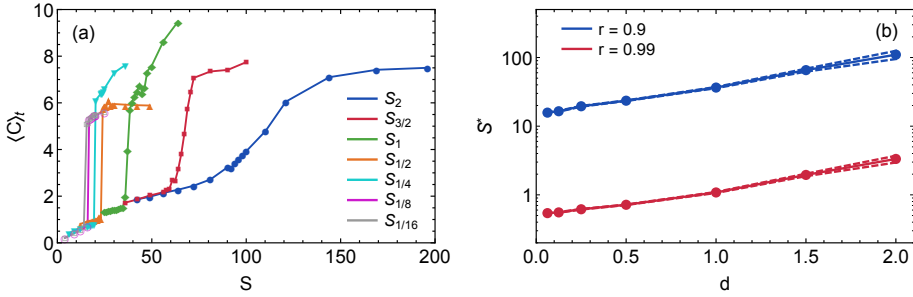


Figure 5.5: (a) Time averaged convection intensity $\langle C \rangle_t$, defined in the main text, as a function of the shaking strength S_f , for the different systems indicated in the labels. (b) Critical transition point S_f^* , for the different systems shown in the (a) figure.

the definition of an appropriate order parameter that captures the transition. We consider the convection intensity,

$$C \equiv \frac{1}{2} \max_z (\max_x (v_z(x, z)) - \min_x (v_z(x, z))), \quad (5.39)$$

where $v_z(x, z)$ is the scalar field of velocities in the z -direction, and the maxima are taken first over z and then over x . Even though the average vertical velocity is expected to scale with $A\omega$, the loss of homogeneity of $v(\vec{x}, t)$ in the convective states results in C growing faster than the energy injection.

The time averaged convection intensity $\langle C \rangle_t$ is shown in Figure 5.5a, as a function of ω_f , for all different dissipative S_d . The transition can be appreciated as a steep increase of $\langle C \rangle_t$ in a small region of S_f ; while this is true for all S_d , the overall shape of the transition varies considerably for different S_d . Transitions for large d present a wider intermediate state, where convective flows are intermittent and highly fluctuating. This is a direct consequence of fluctuations being larger for smaller N . More importantly, it is evident that the critical point of transition S_f^* is not d -invariant, in contrast with (5.35). Figure 5.5b shows S_f^* as a function of d for both dissipative and quasi-elastic systems. The decrease can be fitted by an exponential, $S_f^* \propto \exp(-d)$. It is not clear from our considered range in d if S_f^* eventually saturates at a given value, or goes to zero, as $d \rightarrow 0$.

5.5 CONCLUSIONS

In this chapter we have studied the possibility of creating macroscopically equivalent granular systems with significantly different number of particles. A definition of macroscopic equivalence has been proposed in which all macroscopic, conserved fields must be identical in space, time, and also for different particle sizes d . Considering the Navier-Stokes equations with a energy sink term accounting for particle

dissipation, we have demonstrated that it is not possible to obtain equivalent systems in the most general flow case, as different terms in the equations scale differently with d . Nevertheless, after scaling the restitution coefficient so that heat flux and dissipation are balanced, the limit $d \rightarrow 0$ becomes well defined and leads to a d -invariant set of conservation laws corresponding to a perfect fluid. As a consequence of the dissipation scaling, we have observed that the steady-state, no-flux case equations become d -invariant, disregarding higher order corrections for higher inelasticities.

Simulations of perfect hard-spheres allowed us to test the derived scalings for a considerable range of total number of particles. As test case we considered the granular Leidenfrost state and its transition to buoyancy-driven convection. The granular Leidenfrost state was seen to converge to a given macroscopic state as $d \rightarrow 0$, with the convergence considerably accelerated for lower energy dissipations. Furthermore, the collective oscillatory movement present in the granular Leidenfrost state, LFOs, was deduced to be driven by the intrinsic fluctuations in systems that present a low number of particles. This follows from the decrease of the oscillations amplitude with d for macroscopically equivalent systems, suggesting that in the $d \rightarrow 0$ limit the oscillations would be unmeasurable. Moreover, the frequency of LFOs was observed to remain constant in the range of d studied, in accordance with the previously derived theoretical expression predicting a dependency only on macroscopic features of the Leidenfrost state.

The convergence of flows to the macroscopic states given by the perfect fluid equations as $d \rightarrow 0$ was studied in the transition to buoyancy-driven convection. The intensity of the convective flows, used as an order parameter of the transition, shows behaviour consistent with convergence in the limit $d \rightarrow 0$, although the studied range is not enough to be certain. Further research is currently being carried out for this case.

As a final comment, we would like to remark that the same framework could be used for the study of other out-of-equilibrium granular systems. Macroscopic convergence can be expected as $d \rightarrow 0$, given that the total dissipation and energy injection terms are appropriately scaled, opening the possibility of studying equivalent granular systems with different number of particles.

HYDRODYNAMICS OF THE GRANULAR LEIDENFROST TO CONVECTION TRANSITION¹

We perform a numerical and simulational analysis of the granular Leidenfrost to buoyancy-driven convection transition present in vertically vibrated granular matter. Numerical solutions of the granular hydrodynamic equations in two different approximation limits are compared with discrete particle method simulations (DPM), in order to understand further the relation between microscopic and macroscopic models of granular matter. Finite number effects are studied in the one-dimensional, steady state case, by comparing the hydrodynamic fields with coarse-grained, time-averaged fields obtained from DPM simulations. Macroscopically equivalent particle systems with different particle sizes reveal that finite-size effects are the origin of considerable disagreements in certain parameter regions. In the two dimensional case, the Boussinesq approximation of granular hydrodynamics is considered, and the transition to buoyancy-driven convection is compared with DPM simulations. Overall, the velocity fields present the same qualitative features, although the velocities of the continuum solution are lower, and correspondingly the transition is seen to take place for higher energy injections.

1. Work being done in conjunction with S. Rhebergen and A. R. Thornton.

6.1 INTRODUCTION

Developing a general hydrodynamic model of flowing granular matter has proved to be an enormous challenge. Taking into account the often striking similarity of granular flows to classical fluids [121, 111, 164], it is no surprise that granular hydrodynamic models resemble the Navier-Stokes equations. The main differences reside in the constitutive laws, of which a general form able to reproduce the variety of granular phenomena observed has not yet been recognized. Even the possibility of formulating a general granular hydrodynamic model has been questioned [9, 10]. Nevertheless, significant progress has been made in several scenarios, usually in the low dissipation and packing fraction limits [12, 13, 14, 15, 16, 17, 18]. For more general cases, the difficulties arise from the fundamental characteristics of granular matter: dissipative microscopic interactions, negligible thermal fluctuations, and a lack of separation of scales between the microscopic and macroscopic. These properties usually produce steep inhomogeneities, with regions of high-packing fraction, behaving essentially like solids, coexisting with gaseous like regions, even in the volume of just a few particle diameters. Moreover, fluctuations in granular matter are determinant in the dynamics, due to the usually low number of particles involved in any representative volume [9]. Although the challenge is considerable, the motivations for a continuum theory of granular flows are diverse, as it would be possible to apply the methods of fluid dynamics to granular flows, allowing us to advance our understanding of natural phenomena such as rock slides and avalanches, and improving the handling of granular flows present in many industrial processes.

In the following chapter we present the first results of a numerical study of the granular hydrodynamic equations describing a vertically shaken granular bed. Vibrated granular beds have become an important proving ground in granular research. When vertically agitated, beds of grains exhibit a plethora of different behaviours [60, 61, 64, 65, 68, 71], the study of which has advanced our understanding of out-of-equilibrium steady states in discrete systems. In the following we consider the high energy injection limit, in which grains present density inversion and phase coexistence, a steady state referred to as granular Leidenfrost. The granular Leidenfrost state becomes unstable for higher energy injections, losing its horizontal homogeneity and giving rise to a buoyancy-driven convective state. The transition can be understood as the emergence of a definite length-scale from an homogeneous base state, the scale in this case corresponding to the size of the convective cells. In the following we study the granular Leidenfrost state and its transition to buoyancy-driven convective flows by considering two different limits of a granular hydrodynamics model, in order to distinguish which are the relevant physical effects. We compare our results using discrete particle method (DPM) simulations of a monodisperse collection of perfect hard-spheres.

6.2 SYSTEM AND SIMULATIONS

The setup under study consists of a two-dimensional rectangle container of variable width l_x and high enough so that grains never collide with the top, filled with perfectly and monodisperse hard disks with no friction. In previous experimental and numerical realisations [79, 158] the whole container is shaken in the vertical direction (parallel to gravity), such that grains gain energy through collisions with the bottom boundary and through friction forces with the walls. Here we model the vibrations by considering the bottom wall to have a constant temperature T_0 , as the use of a fixed instead of a moving boundary considerably simplifies the numerical solution of the hydrodynamic equations. This is known to be a good approximation of the low-amplitude and high-frequency shaking case [163], a limit in which we have verified both the granular Leidenfrost and the buoyancy-driven convection state exist (see Chapter 5).

Numerical simulations are performed using an event-driven DPM algorithm, well suited for the simulation of hard-disk collections. The same algorithm has previously been used for studies of similar systems, with excellent agreement with experiments and continuum theories [123, 158] (see Chapters 2 and 3). Collisions between grains are dissipative and modelled by a single parameter, the restitution coefficient r , which quantifies the amount of kinetic energy lost at every collision. The total number of particles N is chosen so that the number of filling layers $F = Nd/l_x = 12$, with d the diameter of the particles. The temperature boundary condition is implemented such that the normal component of the velocity of any colliding particle is set to a random quantity taken from a Maxwellian distribution with temperature T_0 . In order to avoid inelastic collapse, a dissipation-driven effect where the number of particle collisions diverges in a finite time, we set $r = 1$ if the relative velocity of the particles involved in a collision is less than $10^{-5}\sqrt{dg}$ [87], with g the acceleration of gravity.

6.3 GRANULAR HYDRODYNAMICS MODEL

As a model for granular flows we consider the two-dimensional granular hydrodynamic equations obtained through the Chapman-Enskog solution of the Boltzmann kinetic equation [24]. These are: the equation of continuity, or mass balance; the Navier-Stokes equation, or momentum balance; and the granular temperature equa-

tion, or energy balance:

$$\frac{\partial n}{\partial t} + \vec{u} \cdot \nabla n + n \nabla \cdot \vec{u} = 0, \quad (6.1a)$$

$$m n \left(\frac{\partial u}{\partial t} + \vec{u} \cdot \nabla \vec{u} \right) = -\nabla p + \nabla \cdot (\mu \tau) + m n \vec{g}, \quad (6.1b)$$

$$n k_B \left(\frac{\partial T}{\partial t} + \vec{u} \cdot \nabla T \right) = \nabla \cdot (\kappa \nabla T) - p (\nabla \cdot \vec{u}) + \mu \tau : \nabla \vec{u} - I. \quad (6.1c)$$

Here $n(\vec{x}, t)$ is the number density field; m the mass of the particles; $\vec{u}(\vec{x}, t) = (u, v)$ the velocity vector; p the pressure; μ the shear viscosity; $T(\vec{x}, t)$ the granular temperature field, with $k_B T \equiv \frac{1}{2} m (\langle u^2 \rangle - \langle u \rangle^2)$ and k_B the Boltzmann constant; κ the thermal conductivity; the strain rate tensor $\tau = (\nabla \vec{u} + \nabla \vec{u}^T)$ and I the dissipation due to inelastic particle collisions.

A closed set of hydrodynamic equations, with the transport coefficients μ , κ , η , p and the dissipation term I given as functions of the conserved quantities, can be obtained in the low-density, low-dissipation limit, as shown in [26]. We use these expressions even though the Leidenfrost state may contain regions of high packing fraction, as they have already been successful in describing the transition to the convective state [80]. First, let us consider a simple state equation, which takes into account the divergence of the pressure as the packing density of the grains approaches the close packing value,

$$p = n k_B T \frac{n_c + n}{n_c - n}, \quad (6.2)$$

where n_c is the maximum close packing number density, $n_c = 2/(\sqrt{3}d^2)$ in two-dimensions, with d the particles' diameter. Furthermore, from [80], the thermal conductivity is given by

$$\kappa = \frac{n(\alpha l + d)^2}{l} \left(\frac{k_B T}{m} \right)^{1/2}, \quad (6.3)$$

with the mean free path

$$l = \frac{1}{\sqrt{8} n d} \frac{n_c - n}{n_c - a n}, \quad (6.4)$$

with $a = 0.39$, defined by fitting low-density and high-density approximations of the mean free path [165]; and $\alpha = 0.6$ a free parameter, the value taken to be the same as previous hydrodynamic models of equivalent systems [15, 80]. The viscosity is determined by the Prandtl number, $\text{Pr} = \mu/\kappa$, with Pr a free parameter expected to be of order 1 from previous descriptions of the same system [80]. Finally, the energy-density dissipation is taken as [80]

$$I = \frac{\epsilon}{\gamma_c l} n k_B T \left(\frac{k_B T}{m} \right)^{1/2}, \quad (6.5)$$

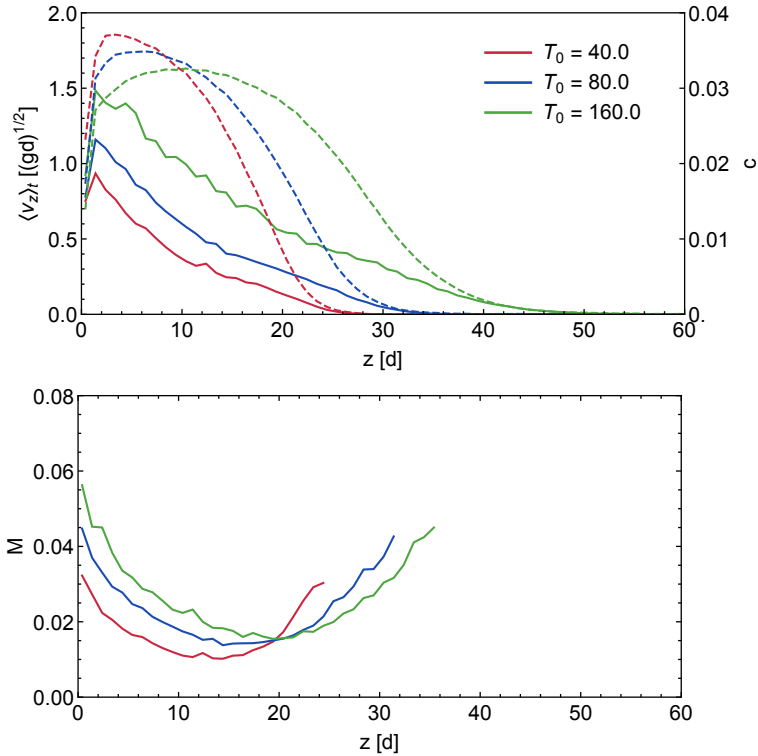


Figure 6.1: (top) Time-averaged vertical velocity profile, $\langle v_z \rangle_t(z)$ (solid), and the speed of sound c (as defined in the main text; dashed), for systems with the base temperatures indicated. (bottom) Mach number, $M \equiv \langle v_z \rangle_t(z)/c$, for the same systems than the top figure.

with $\epsilon = 1 - r^2$, r the coefficient of restitution for particle-particle collisions, and $\gamma_c = 2.26$ again taken from previous similar studies [165].

The numerical solution of (6.1) presents a significant numerical challenge, specially with elaborate transport coefficients that further depend on T and n . In addition, computing the Mach number M reveals that the flow in the granular Leidenfrost state is highly incompressible. We consider

$$M \equiv \frac{v_m}{c}, \quad (6.6)$$

with v_m the speed of the object moving through a medium with speed of sound c . In our case, v_m is taken as the vertical component of the time-averaged coarse-grained velocity field, $\langle v_z(z) \rangle_t$. Here, and in what follows, time averages are taken for $10^5 \sqrt{d/g}$. In order to determine the speed of sound the relation $c^2 = \partial p / \partial \rho$ is

used; from (6.2),

$$c^2 = k_B T \left(\frac{n_c^2 + 2nn_c - n^2}{(n - n_c)^2} \right). \quad (6.7)$$

Simulations allow us to obtain $n(z)$, $T(z)$ and $\langle v_z(z) \rangle_t$, and thus to compute M . Figure 6.1 shows $\langle v_z(z) \rangle_t$ and $\langle c(z) \rangle_t$ for different base temperatures T_0 and $r = 0.95$. We see that $\langle c(z) \rangle_t$ presents a maximum at roughly the location of the highly-packed region, and then decays exponentially until the free surface, while $\langle v_z(z) \rangle_t$ decays monotonically, similar to the temperature field. This results in $M \in (0.01, 0.06)$, as shown in Figure 6.1, values in a range far too low to consider compressible numerical schemes. The low Mach numbers imply that the incompressible flow approximation must be taken, $\nabla \cdot \vec{v} = Dn/Dt = 0$. With this, (6.1) results in

$$\nabla \cdot \vec{v} = 0, \quad (6.8a)$$

$$mn \left(\frac{\partial \vec{u}}{\partial t} + \vec{u} \cdot \nabla \vec{u} \right) = -\nabla p + \nabla \cdot (\mu \tau) - mn \vec{g}, \quad (6.8b)$$

$$nk_B \left(\frac{\partial T}{\partial t} + \vec{u} \cdot \nabla T \right) = \nabla \cdot (\kappa \nabla T) - I. \quad (6.8c)$$

As the general solution of (6.8) with non-linear constitutive laws presents a significant numerical challenge, especially in the high energy injection limit, we consider two limits of distinct physical approximations: a one-dimensional steady state case, and a two-dimensional granular model under the Buossinesq approximation. In what follows we study until what extent these situations are able to reproduce the observed granular phenomena by comparing with analogous DPM simulations.

6.4 ONE-DIMENSIONAL STEADY STATE

The granular Leidenfrost state consists of a no-flux, steady state, with inhomogeneities occurring only in the direction of gravity. Therefore, we consider an equivalent limit in the hydrodynamic equations, by taking $\vec{u} = 0$ and the one-dimensional case in (6.8):

$$-\frac{\partial p}{\partial z} = mng, \quad (6.9a)$$

$$\frac{\partial}{\partial z} \left(\kappa \frac{\partial T}{\partial z} \right) - I = 0. \quad (6.9b)$$

The set of equations (6.9), plus the equation of state (6.2), have already been studied for models of density inverted granular systems [15, 79]; here we explore further the ability of these equations to capture particle simulations. As we have taken the one-dimensional limit, it is not possible in this case to capture the transition to convective states, allowing us to study the granular Leidenfrost state for a wider range of parameters. For these three equations three boundary conditions are

needed, accounting for the free surface at the top and the energy injection at the bottom. For the free surface we consider zero pressure, $p_{z=\infty} = 0$, and zero energy flux, $(\partial_z T)_{z=\infty} = 0$. The bottom boundary comes directly from our considered system, $T_{z=0} = T_0$. The density at the bottom follows from the state equation: integrating (6.9a) over the domain gives,

$$p_{z=0} - p_{z=\infty} = mNg \quad (6.10)$$

with N the total number of particles in the system. From (6.2) and $p_{z=\infty} = 0$,

$$n_{z=0} k_B T_{z=0} \frac{n_c + n_{z=0}}{n_c - n_{z=0}} = mNg \quad (6.11)$$

from which we get the bottom density boundary condition,

$$n_{z=0} = \frac{-mNg - k_B T_0 n_c \pm \sqrt{(mNg + k_B T_{z=0} n_c)^2 + 4k_B T_{z=0} mNg n_c}}{2k_B T_{z=0}}. \quad (6.12)$$

This condition is a consequence of particle conservation, as we used that $\int_0^\infty n(z) dz = N$. Finally, as initial condition we take an exponentially decaying temperature field $T_0(z, t = 0) = T_0 e^{-z/5.0}$, and a constant density field $n(z, t = 0) = n_{z=0}$.

RESULTS

Equations (6.9) are solved using the numerical methods described in Appendix 6.6. Solutions are compared with event-driven DPM simulations of the granular Leidenfrost state. In both cases $r = 0.95$, and the same T_0 is used. Once the continuum system has been determined, there is no free parameter in the particle simulations except for l_x , which is chosen so that horizontal inhomogeneities cannot develop (a quasi-one-dimensional limit), $l_x = 5.0d$.

Numerical solutions capture the qualitative features of simulations, with good quantitative agreement for a range of temperatures $T_0 \in (30, 60)gd$, as shown in Figure 6.2. Discrepancies may have their origin in both the physical assumptions and choice of parameters made in the continuum equations and constitutive laws, as also in finite-number and finite-size effects of particle simulations; in what follows we fix the continuum model and parameters, and study the agreements by modifying the particle simulations. Discrepancies at low T_0 are marked by much lower densities and higher temperatures in the continuum solutions, possibly from dominant excluded volume and finite-size effects in DPM simulations. For high T_0 , on the other hand, densities are overall higher and temperatures lower in the continuum solutions, and there is good agreement in $\langle n(z) \rangle_t$ in the gaseous region. We remark that in the simulations shown $N = 60$, a remarkably low number of particles that can nevertheless be captured, in certain limits, by a continuum model.

In order to investigate the influence of finite-size effects, we use the methodology developed in Chapter 5 to obtain macroscopically equivalent systems with particles

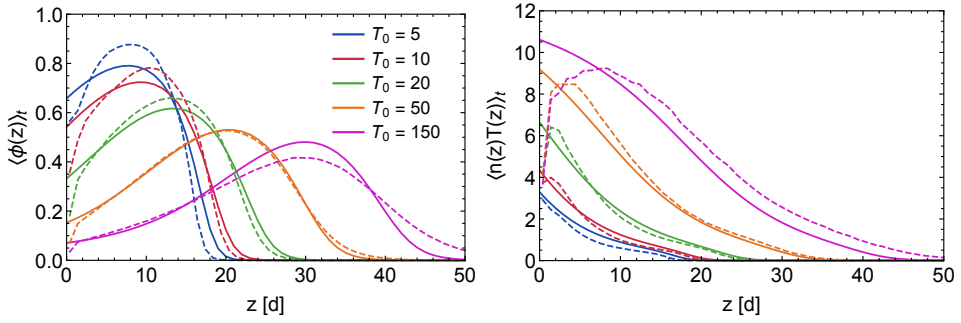


Figure 6.2: Time averaged packing fraction profiles $\langle \phi(z) \rangle_t$, left) and total fluctuating kinetic energy density $\langle n(z)T(z) \rangle_t$, right) for several different T_0 , specified in the labels. Numerical solutions of granular hydrodynamic equations are shown with solid lines, while event-driven discrete particle simulations with dashed lines.

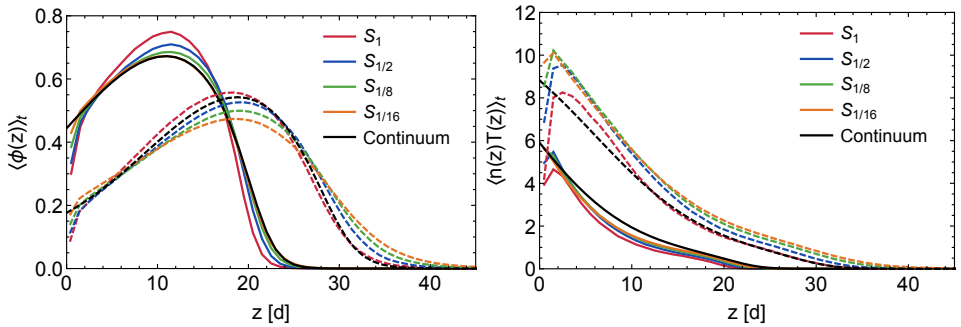


Figure 6.3: Time averaged packing fraction profiles $\langle \phi(z) \rangle_t$ (left) and total temperature profiles $\langle n(z)T(z) \rangle_t$ (right) from equivalent systems with different particle diameters d , as shown in the inset, and the numerical solution of the granular hydrodynamic equations. Two bottom temperatures are shown: $T_0 = 15$ (solid) and $T_0 = 50$ (dashed).

of different sizes. The method consists in taking d as control parameter and adjusting the rest of the system parameters such that the hydrodynamic description of the microscopic state, in this case given by (6.9), remains invariant (for a detailed description, we refer the reader to Chapter 5). As d is decreased, the total excluded volume from particle-wall interactions is expected to be reduced. For low T_0 we observe convergence of the microscopic averaged fields to the hydrodynamic solution, as shown in Figure 6.3 for $\langle\phi(z)\rangle_t$. The effect of excluded volume is clear by looking at the bottom boundary, where $\langle\phi(z)\rangle_t$ shows a monotonic increase as $d \rightarrow 0$, finally converging to the hydrodynamic solution. There is also a considerable decrease of $\langle\phi(z)\rangle_t$ at the highly packed region; as discussed in Chapter 5, we believe this to be mainly due to the effect of the side-walls. This case is representative for temperatures $T_0 < 30gd$. For higher T_0 equivalent systems also show the effects of reduced excluded volume effects, although in this case there is no convergence to the continuum solution as $d \rightarrow 0$. Temperature fields, on the other hand, do not improve the agreement beyond boundary effects, and even deviate farther from the continuous solution for $T_0 > 30gd$ as $d \rightarrow 0$. These suggests that the discrepancies may be an effect of the derived T_0 scaling with d , and the density decrease observed for systems with high T_0 may be a consequence of an overall higher temperature. Nevertheless, other factors may also be involved.

6.5 BOUSSINESQ APPROXIMATION

Increasing the energy injection from the granular Leidenfrost effect leads to a buoyancy-driven convective state (see Chapter 4). In the following section we consider (6.8) under the Boussinesq approximation, and compare the solutions with the fields obtained from DPM simulations. In the Boussinesq approximation the density is considered to be constant $n = n_b$, except at the gravity term. This approximation is often used in studies of Rayleigh-Bernard convection [166], and has even been compared with DPM simulations [167], although for considerably lower densities and energy injections. Here we push the boundary of the constant density approximation to see what is captured by this model or, equivalently, what characteristics are not present in the constant density limit.

Some rearrangement of (6.8) facilitates the interpretation of the Boussinesq limit. We define $P \equiv p - p_b(z)$ where $p_b(z) \equiv -mn_bgz\hat{z} + c$, with c the arbitrary constant that sets the level for the pressure. Then, in (6.8b), $-\nabla p - mng\hat{z} = -\nabla P + m(n_b - n)g\hat{z}$. With these considerations, (6.8) is then given by

$$\nabla \cdot \vec{v} = 0 \quad (6.13a)$$

$$\frac{\partial \vec{u}}{\partial t} + \vec{u} \cdot \nabla \vec{u} = -\frac{1}{mn_b} \nabla P + \frac{1}{mn_b} \nabla \cdot (2\mu\tau) + \frac{\Delta n}{n_b} g\hat{z} \quad (6.13b)$$

$$\frac{\partial T}{\partial t} + \vec{u} \cdot \nabla T = \frac{1}{n_b k_B} \nabla \cdot (\kappa \nabla T) - \frac{I}{n_b k_B}. \quad (6.13c)$$

with $\Delta n = n_b - n$, which is further approximated by $(n_b - n) \approx n_b \beta (T - T_b)$, with β the coefficient of volume expansion, in our case a free parameter. Notice that in the Boussinesq approximation the state equation loses significance, as the number density is constant, but the pressure is still a variable.

We now proceed to scale (6.13). We consider the most general scaling relations, as it will then facilitate the comparison between hydrodynamic and particle systems. These are

$$\vec{x} = x_0 \tilde{x}, \quad t = t_0 \tilde{t}, \quad n = n_0 \tilde{n}, \quad P = P_0 \tilde{P}$$

All scales should be given by the parameters x_0 , n_0 , t_0 and P_0 , but not all transport coefficients are known as a function of these quantities. Since there is no state equation, P_0 is also a parameter. The most direct one comes from $u = dx/dt = (x_0/t_0)d\tilde{x}/d\tilde{t} \equiv (x_0/t_0)\tilde{u}$. The strain rate tensor is given by $\tau = \frac{1}{2}(\nabla u + \nabla u^T)$, so $\tau = 1/t_0(\tilde{\nabla}\tilde{u} + \tilde{\nabla}\tilde{u}^T) \equiv \tilde{\tau}/t_0$. The temperature scale is given by the definition of granular temperature, $k_B T = \frac{1}{2}m(\langle u^2 \rangle - \langle u \rangle^2) = (x_0^2 m/t_0^2) \frac{1}{2}(\langle \tilde{u}^2 \rangle - \langle \tilde{u} \rangle^2) \equiv (x_0^2 m/t_0^2) k_B \tilde{T}$. The mean free path with the Boussinesq approximation becomes a constant,

$$l = \frac{1}{\sqrt{8}n_b d} \frac{n_c - n_b}{n_c - an_b} \equiv l_b. \quad (6.14)$$

The energy dissipation term results in

$$I = \frac{\epsilon}{\gamma_c l_b} n_b k_B T \left(\frac{k_B T}{m} \right)^{1/2} = \left(\frac{x_0^3 k_B^{3/2}}{t_0^3} \right) \frac{\epsilon}{\gamma_c l_b} n_b \tilde{T}^{3/2} \equiv \left(\frac{x_0^3 k_B^{3/2}}{t_0^3} \right) \tilde{I}_b. \quad (6.15)$$

The form of the thermal conductivity we know,

$$\kappa = \frac{n_b (\alpha l_b + d)^2}{l_b} \left(\frac{k_B T}{m} \right)^{1/2} = \left(\frac{x_0 k_B^{1/2}}{t_0} \right) \frac{n_b (\alpha l_b + d)^2}{l_b} \tilde{T}^{1/2} \equiv \left(\frac{x_0 k_B^{1/2}}{t_0} \right) \tilde{\kappa}. \quad (6.16)$$

The viscosity is determined by the Prandtl number

$$\mu = \frac{m \text{Pr}}{\kappa} = \left(\frac{t_0 m}{x_0 k_B^{1/2}} \right) \frac{\text{Pr}}{\tilde{\kappa}} \equiv \left(\frac{t_0 m}{x_0 k_B^{1/2}} \right) \tilde{\mu}_b \quad (6.17)$$

Substituting in (6.13) we obtain the general form:

$$\tilde{\nabla} \cdot \tilde{\vec{u}} = 0, \quad (6.18a)$$

$$\partial_{\tilde{t}} \tilde{\vec{u}} + \tilde{\vec{u}} \cdot \tilde{\nabla} \tilde{\vec{u}} = - \frac{t_0^2 P_0}{x_0^2 m n_b} \tilde{\nabla} \tilde{P}_b + \frac{t_0^2}{x_0^3 n_b k_B^{1/2}} \tilde{\nabla} \cdot (2 \tilde{\mu}_b \tilde{\tau}) + x_0 m \beta (T - T_b) g \hat{z}, \quad (6.18b)$$

$$\partial_{\tilde{t}} \tilde{T} + \tilde{\vec{u}} \cdot \tilde{\nabla} \tilde{T} = \frac{1}{n_b x_0 t_0 k_B^{1/2}} \tilde{\nabla} \cdot (\tilde{\kappa}_b \tilde{\nabla} \tilde{T}) - \frac{x_0 k_B^{1/2}}{n_b} \tilde{I}_b. \quad (6.18c)$$

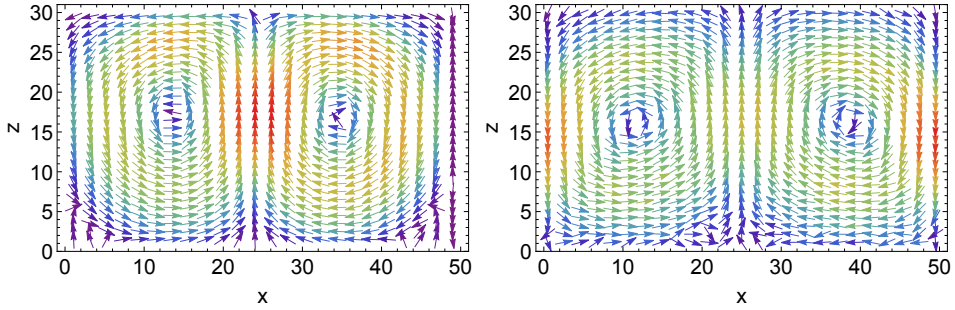


Figure 6.4: Velocity field $\vec{v}(\vec{x})$, obtained through solving the granular hydrodynamic equations in the Boussinesq approximation (left), and time-averaged velocity field $\langle \vec{v}(\vec{x}) \rangle_t$ computed from event-driven discrete particle dynamics simulations (right).

In terms of dimensionless numbers,

$$\tilde{\nabla} \cdot \tilde{\vec{u}} = 0, \quad (6.19a)$$

$$\partial_{\tilde{t}} \tilde{\vec{u}} + \tilde{\vec{u}} \cdot \tilde{\nabla} \tilde{\vec{u}} = -\text{At} \tilde{\nabla} \tilde{P}_b + \text{Re}^{-1} \tilde{\nabla} \cdot (2\tilde{\mu}_b \tilde{\tau}) + \text{Fr}^{-2} g \hat{z}, \quad (6.19b)$$

$$\partial_{\tilde{t}} \tilde{T} + \tilde{\vec{u}} \cdot \tilde{\nabla} \tilde{T} = \text{Pe}^{-1} \tilde{\nabla} \cdot (\tilde{\kappa}_b \tilde{\nabla} \tilde{T}) - \text{Gr} \tilde{I}_b. \quad (6.19c)$$

Finally, the set of boundary conditions must be specified. For the side boundaries we consider no flux $\vec{u} = 0$ and no temperature gradient in the normal direction, $\hat{n} \cdot \nabla T = 0$. For the bottom boundary we consider $T_{z=0} = T_0$, while for the velocity we consider a Neumann boundary condition $\nabla \vec{u} = 0$.

RESULTS

Equations (6.19) are solved using the numerical methods described in Appendix 6.6. The model captures the transition from an horizontally homogeneous state to a convective one, as is evident by looking at $\langle \vec{v}(\vec{x}) \rangle_t$, shown in Figure 6.4. For these cases, $\beta = 0.1$ and $P_0 = 1.0$; an initial exploration of the parameter space reveals the same overall features although with considerable changes in the critical temperature of transition T_0^* . For $T_0 > 200gd$ no steady state was reached, and eventually the numerical scheme became unstable; the transient state oscillated between unstable configurations of two and three convective rolls.

There is clear qualitative agreement between the continuum solutions and the time-averaged DPM simulations fields, as Figure 6.4 reveals. Nevertheless, differences are considerable. The most clear discrepancy is the relatively higher upward velocities in the centre than the sides in the continuum solutions, although this is expected to be a consequence of the selected boundary conditions. First investigations show that when using Neumann boundary conditions this effect disappears. Quantitatively, velocities in the Hydrodynamic case are seen to be consistently higher than

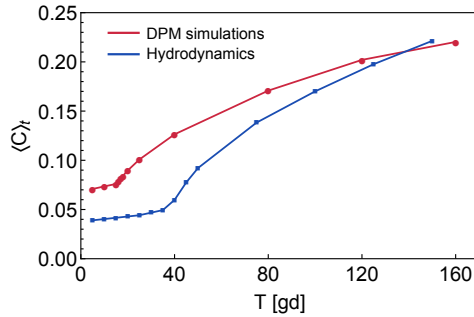


Figure 6.5: Velocity fields $\vec{v}(\vec{x})$, for event-driven discrete particle dynamics simulations (left) and continuum solution of granular hydrodynamics in the bousinesq approximation (right).

the DPM simulations. The reason of this discrepancies is unknown, although several free parameters have yet to be explored.

To quantify the transition to convection we use the convection intensity order parameter,

$$C \equiv \frac{1}{2} \max_z (\max_x (v_z(x, z)) - \min_x (v_z(x, z))). \quad (6.20)$$

The value of C increases as the velocity fields loses its homogeneity in the horizontal direction. Figure 6.5 shows $\langle C \rangle_t$ for both DPM simulations and the hydrodynamic solutions. In both cases the transition is evident as a steep increase of $\langle C \rangle_t$. Due to the aforementioned discrepancies in the velocities, the convection intensity in continuum solutions is lower than DPM simulations for most of the studied T_0 range; consequently, the transition is seen to require a higher T_0^* . Possibly, exploring the parameter space would lead to a better agreement.

6.6 CONCLUSIONS

In this chapter we have shown an initial analysis of the granular Leidenfrost state and its transition to buoyancy-driven convection using a granular hydrodynamic model in two distinct limits. By computing the Mach number it was shown that when modelled as a continuum, the bed of grains is in the highly incompressible limit. The relevant hydrodynamic equations were then derived and solved, overall showing similar features than discrete particle simulations of hard disks. In the one-dimensional and steady state limit, continuum solutions show density inversion and a decaying temperature field, both characteristic of the granular Leidenfrost state. The agreement with DPM simulations with a total of 60 particles is optimal in an intermediate range of energy injection, while maximal densities are underestimated in the low energy injection limit and overestimated in the high energy injection limit. By constructing macroscopically equivalent systems with different number

of particles it was possible to study finite-size effects; as the size of the particles was decreased, the agreement for low temperatures improved, while for higher temperatures the coarse-grained DPM simulation fields did not converge to the continuum solution. The source of these disagreements is currently under study.

The second limit considered corresponds to the two-dimensional granular hydrodynamic equations with a Buossinesq approximation. The transition to convection was observed in the velocity field, and shows a good qualitative agreement with DPM simulations. Nevertheless, there are important quantitative differences between the two methods. Work is being done in exploring further the parameter space, and establishing the origin of the disagreements.

APPENDIX: NUMERICAL METHODS

The methods to numerically solve the sets of equations (6.9) and (6.19) are detailed in what follows. These formulations are implemented in the finite-element package for solving partial differential equations FEniCS [168].

ONE-DIMENSIONAL NO-FLUX STATE

The one-dimensional model is solved by a simple Crank-Nicolson time-stepping scheme. The state equation is taken into account by substituting (6.2) in (6.9a):

$$\frac{1}{n_c - n} \left(nT \partial_z n + (n + n_c)T \partial_z n + n(n + n_c) \partial_z T + \frac{n(n + n_c)T \partial_z n}{n_c - n} \right) + mng = 0 \quad (6.21)$$

Now, let V_h be a continuous finite element space defined on a domain Ω . The weak formulation for (6.9) is given by: find $n \in V_h$ and $T \in V_h$ such that:

$$\int_{\Omega} q \left(\frac{1}{n_c - n} \left(nT \partial_z n + (n + n_c)T \partial_z n + n(n + n_c) \partial_z T + \frac{n(n + n_c)T \partial_z n}{n_c - n} \right) \right) dz + \int_{\Omega} q mng dz = 0, \quad \forall q \in V_h, \quad (6.22a)$$

$$\int_{\Omega} \frac{wn(T - T_0)}{\Delta t} + \frac{1}{2} \int_{\Omega} \partial_z w(k(T, n) \partial_z T) dz + \frac{1}{2} \int_{\Omega} wI(T, n) dz + \frac{1}{2} \int_{\Omega} \partial_z w(\kappa(T_0, n_0) \partial_z T_0) dz + \frac{1}{2} \int_{\Omega} wI(T_0, n_0) dz = 0, \quad \forall w \in V_h, \quad (6.22b)$$

where we applied a Crank-Nicolson time-stepping scheme for the time derivative. Here T is the unknown value and T_0 is the value of T from the previous time-step. Due to the strong non-linearities, we solve (6.22) in an iterative way per time-step, with an inner and outer iteration. The process of one outer iteration step is given as

follows: given a n_0 and T_m we apply a Newton method (the inner iterations) to:

$$\int_{\Omega} q \left(\frac{1}{n_c - n} \left(nT \partial_z n + (n + n_c)T \partial_z n + n(n + n_c) \partial_z T + \frac{n(n + n_c)T \partial_z n}{n_c - n} \right) \right) dz + \int_{\Omega} qmng dz = 0 \quad (6.23a)$$

$$\int_{\Omega} \frac{wn_0(T - T_0)}{\Delta t} + \frac{1}{2} \int_{\Omega} \partial_z w(\tilde{\kappa}(n_0) \sqrt{T_m/m_0} \partial_z T) dz + \frac{1}{2} \int_{\Omega} w\tilde{I}(T_0)T \sqrt{T_m/m_0} dz + \frac{1}{2} \int_{\Omega} \partial_z w(\tilde{\kappa}(n_0) \sqrt{T_0/m_0} \partial_z T_0) dz + \frac{1}{2} \int_{\Omega} w\tilde{I}(n_0)T_0 \sqrt{T_0/m_0} dz = 0 \quad (6.23b)$$

where $\tilde{\kappa}$ and \tilde{I} are given by (6.3) and (6.5). Having solved for T and n by the Newton method, we update $T_m = T$ and $n_0 = n$ and proceed to the next outer iteration. The outer iteration ends after some criteria of convergence tolerance has been set, after which we proceed to the next time step and set $T_0 = T$.

BOUSSINESQ APPROXIMATION

In order to solve equations (6.18) we decouple the temperature equation (6.19c) from the Navier-Stokes equation (6.19b), that is, given a temperature field T we update the velocity \vec{u} and pressure p by solving (6.19b). Given the velocity \vec{u} we update the temperature T by solving (6.19c). Per time-step we may iterate over this process multiple times for higher accuracy.

To solve the Navier-Stokes equation (6.19b) with the incompressibility condition (6.19a) we apply Chorin's method. For the initial setup of this method we used a FEniCS demo [168]. The Chorin's method is applied in three steps. The first step solves the momentum equation while ignoring the pressure, resulting in a tentative velocity \vec{u}^* : find $\vec{u}^* \in \vec{V}_h$ such that

$$\int_{\Omega} \frac{1}{\Delta t} (\vec{u}^* - \vec{u}^{n-1}) \cdot \vec{v} dx + \int_{\Omega} \nabla \vec{u}^{n-1} \vec{u}^{n-1} \cdot \vec{v} dx + \int_{\Omega} 2\mu(T)Re^{-1} \tau(\vec{u}^*) : \tau(\vec{v}) dx - \int_{\Omega} T\beta Fr^{-2} g \hat{z} \cdot \vec{v} dx = 0, \quad \forall \vec{v} \in \vec{V}_h \quad (6.24)$$

where β is a given constant. The second step computes a pressure: find $p \in Q_h$ such that

$$\int_{\Omega} \nabla p^n \cdot \nabla q dx = - \int_{\Omega} \frac{1}{\Delta t} \nabla \cdot \vec{u}^* q dx, \quad \forall q \in Q_h. \quad (6.25)$$

The third step updates the velocity based on \vec{u}^* and p^n : find $\vec{u}^n \in \vec{V}_h$ such that

$$\int_{\Omega} \vec{u}^n \cdot \vec{v} dx = \int_{\Omega} \vec{u}^* \cdot \vec{v} dx - \Delta t \nabla p^n \cdot \vec{v} dx, \quad \forall \vec{v} \in \vec{V}_h. \quad (6.26)$$

With the velocity and pressure known, we may solve for the temperature. We apply a Crank-Nicolson method to discretize (6.19c) in time. Set $T^n = T^0$ and $T^{n+1} = T$

then (6.19b) becomes

$$T + \frac{1}{2}\Delta t \left(\vec{u} \cdot \nabla T - \nabla \cdot \left(\kappa(T) P e^{-1} \nabla T \right) + I(T) \right) = T_0 - \frac{1}{2}\Delta t \left(\vec{u} \cdot \nabla T_0 - \nabla \cdot \left(\kappa(T_0) P e^{-1} \nabla T_0 + I(T_0) \right) \right). \quad (6.27)$$

This equation is non-linear in T so we apply a Picard/Newton method: write $T = T^1 + \delta T$ and note that

$$I(T) \approx I(T^1) + I'(T^1)\delta T, \quad (6.28)$$

$$\nabla \cdot \left(\kappa(T) P e^{-1} \nabla T \right) \approx \nabla \cdot \left(\kappa(T^1) P e^{-1} \nabla T^1 \right) + \nabla \cdot \left(\kappa(T^1) P e^{-1} \nabla \delta T \right).$$

We write (6.27) as

$$\delta T + \frac{1}{2}\Delta t \left(\vec{u} \cdot \nabla \delta T - \nabla \cdot \left(\kappa(T^1) P e^{-1} \nabla \delta T \right) + I'(T^1)\delta T \right) = T^0 - T^1 - \frac{1}{2}\Delta t \left(\vec{u} \cdot \nabla T^0 + \vec{u} \cdot \nabla T^1 - \nabla \cdot \left(\kappa(T^0) P e^{-1} \nabla T^0 \right) - \nabla \cdot \left(\kappa(T^1) P e^{-1} \nabla T^1 \right) + I(T^0) + I(T^1) \right) \quad (6.29)$$

The weak formulation becomes: find $\delta T \in V_h$ such that

$$\begin{aligned} \int_{\Omega} w \delta T \, dx + \frac{1}{2}\Delta t \int_{\Omega} w \vec{u} \cdot \nabla \delta T \, dx + \frac{1}{2}\Delta t \int_{\Omega} \nabla w \cdot \left(\frac{\kappa(T^1)}{P e} \right) \nabla \delta T \, dx \\ + \frac{1}{2}\Delta t \int_{\Omega} w I'(T^1) \delta T \, dx = \\ \int_{\Omega} w (T_0 - T_1) \, dx - \frac{1}{2}\Delta t \int_{\Omega} w \vec{u} \cdot \nabla T_1 \, dx - \frac{1}{2}\Delta t \int_{\Omega} w \vec{u} \cdot \nabla T_0 \, dx \\ - \frac{1}{2}\Delta t \int_{\Omega} \nabla w \cdot \left(\frac{\kappa(T^1)}{P e} \right) \nabla T_1 \, dx - \frac{1}{2}\Delta t \int_{\Omega} \nabla w \cdot \left(\frac{\kappa(T^1)}{P e} \right) \nabla T_0 \, dx \\ - \frac{1}{2}\Delta t \int_{\Omega} w I(T^1) \, dx - \frac{1}{2}\Delta t \int_{\Omega} w I(T^0) \, dx, \quad \forall w \in V_h. \quad (6.30) \end{aligned}$$

Having found δT we compute $T = T^1 + \delta T$ and iterate this process until some convergence tolerance has been met. Given the converged T we may then update again the velocity and pressure.

CONCLUSIONS AND OUTLOOK

There is no science without fancy, and no art without fact.

—Vladimir Nabokov

This thesis concerned the dynamics of vibrated granular matter using discrete particle simulations, experiments and theoretical analysis. Exploring further the rich phenomenology of vertically vibrated bed of grains has revealed new collective behaviours and intricate transition dynamics, novel examples of complex phenomena in out-of-equilibrium particle systems. By comparing simulations and experiments with hydrodynamic theoretical descriptions, an investigation has been made on the relation between discrete and continuum descriptions of what are by definition many-particle systems. Overall, an effort has been made to describe the same system using different model types, such that by comparing the results obtained in each case, insight has been gained on the physical validity of each approach, as also on the dynamics of the system.

Chapter 2 started by presenting the systems under study; vertically agitated narrow boxes filled with spherical grains. When highly agitated, grains separate in a dense, low temperature region on top of a rare, highly temperature one, a density inverted state referred to as granular Leidenfrost. In this thesis a first observation and characterization of semi-periodic oscillations in the granular Leidenfrost state was reported. These oscillations were named low-frequency oscillations (LFOs) due to their frequency being orders of magnitude lower than the container's shaking frequency. Simulations in both quasi-one-dimensional and quasi-two-dimensional geometries revealed that LFOs are not only present in the horizontally homogeneous granular Leidenfrost state, but also in the buoyancy-driven convective state that rises for higher energy inputs; the necessary condition of vertical density inversion is present in both states. The oscillations were characterized using the evolution of the centre of mass of the system, which showed that their amplitude is proportional to

ω , the frequency of vibration of the container, whereas the characteristic frequency of LFOs is inversely proportional to ω .

Modelling the grains bed as a continuum, an analysis of the density inverted scenario revealed that, in the right limits, the position of the dense region follows a forced harmonic oscillator equation of motion. An expression was derived for the expected LFO frequency as a function of a zero-order approximation of the density profile. For this, the depth-averaging mathematical technique was used, which proved to be useful in the description of highly constrained and vibrated granular media. The predicted frequencies show a remarkable agreement with particle simulations in the limit of high energy injections. A second model was proposed that considers thermodynamic and elasticity theory arguments, resulting in a very similar expression for the LFOs frequencies, suggesting that the results are general for a broad class of density inverted systems.

Experimental work, presented in Chapter 3, confirmed the existence of low-frequency oscillations in the granular Leidenfrost and buoyancy-driven convective states. The previously derived theoretical predictions for the frequency of the oscillations was shown to be accurate in the parameter range reachable by experiments. Experiments were realized using the Positron-Emission Particle Tracking technique, again proven to be very useful for the understanding of shaken granular matter: by following the trajectory of one particle and integrating its position over time, density and velocity profiles were obtained, in good agreement with simulations. Data analysis of the particle's position further revealed convective phenomena in highly-packed states, not easily observable by more traditional imaging methods, where usually only boundary layers can be imaged. This slow circulation of particles was shown to be present for very low energy injections.

In Chapter 4 a detailed examination of the granular Leidenfrost to buoyancy-driven convection transition was presented. The buoyancy-driven convective motion was observed to be preceded by time-dependent fluctuating convective flows present while still in the Leidenfrost state, and even far from the transition point. Their velocity was measured to be at least an order of magnitude lower than flows in buoyancy-driven convection. A first characterization of these transient flows revealed that the time of correlation of the velocity fields increases critically as the transition is approached. Furthermore, fluctuating convective states were not observed to be associated with temperature or density inhomogeneities, and can occur in highly packed Leidenfrost states. As the energy injection is increased, the correlation of these flows grows, eventually giving rise to density fluctuations, which proceed to dominate the dynamics. Density fluctuations were characterized using the static structure function which was able to capture the growth of these fluctuations as a clearly defined peak at a critical length-scale. This dominating wavelength corresponds with the critical convective cell size, which is independent of the size of the container. As the energy input increases further, the size of the convective cells also increases, which leads to intricate dynamics for containers which do not fit an

integer number of convective cells. Throughout the study of the transition, dissipative, periodic and elastic solid walls in the horizontal direction were considered, revealing that the critical points are only slightly affected by the different boundaries in small containers (and for the weak dissipation considered), and play no determinant role in very wide containers.

The critical behaviour of the granular Leidenfrost to buoyancy-driven convection transition was characterized by following the amplitude of the critical mode in the vertical velocity field. The shape of the transition was observed to be consistent with a quintic supercritical bifurcation. As this type of bifurcation is associated with spatially extended periodically excited systems—such as Faraday instabilities or vibrated coupled chains of pendula—we hypothesize that low-frequency oscillations play a fundamental role on the dynamics of these states, even well into the convective state. In order to obtain an adequate agreement it is necessary to include an additive noise-term in the corresponding amplitude equation, which quantifies, among other effects, fluctuations due to the finite-number of particles involved. The amplitude of the noise term was not seen to vary between small and large systems for sufficiently wide containers, suggesting that its origin depends on the amount of particles per base area unit, thus involving always the same amount of particles for a given filling height.

The relation between discrete and continuum descriptions of granular systems was studied further in Chapter 5. A methodology was developed to study the role of fluctuations arising in granular systems due to the low total number of particles (when compared to molecular systems). The method involves defining macroscopically equivalent systems, that is, systems that can have different microscopic properties but possess equivalent macroscopic fields. Considering a form of granular hydrodynamic equations, the dependency of all the terms with the size of the particles was derived. It was then proven that it is not possible to vary the size of the particles and retain the same macroscopic state in the most general flow case, and for simple microscopic systems involving only particle-particle dissipative interactions. Nevertheless, by adequately scaling the restitution coefficient and the energy injection parameters, it is possible to leave the hydrodynamic equations describing the granular Leidenfrost state invariant, for systems with different particle size and thus number of particles. Simulations that followed the found scaling laws showed that the density and temperature fields converge as the particle size is decreased. The observation of macroscopically equivalent granular Leidenfrost states then allowed us to observe that the amplitude of LFOs is inversely proportional to the total number of particles. This suggests that LFOs are driven by fluctuations due to the finite number of particles, i.e., that they are an essentially discrete phenomenon. On the other hand, the frequency of the oscillations was seen to converge to a given value, in accordance with the derived theoretical expression, which depends only on continuous, macroscopic quantities.

In the last section, Chapter 6, the granular hydrodynamic equations were solved

for systems in the granular Leidenfrost state and buoyancy-driven convection. This initial numerical analysis first established the correct physical limit in which to model the granular Leidenfrost state by a continuum theory. By computing the Mach number it was shown that the flow is on the highly incompressible limit. The difficulty of solving the full incompressible hydrodynamic equations for high energy injections and complex transport coefficients motivated the use of two different approximations. First, the steady-state, one-dimensional case was considered as a model of the Leidenfrost state. Comparing with DPM simulations and using the methodology derived in the previous chapter revealed that finite-size effects are a relevant source of disagreements between the continuum solution and the coarse-grained fields obtained from simulations. The agreement is in general worse for higher energy injections. The second case studied was the two-dimensional granular hydrodynamic model under the Buossinesq approximation. The transition to convection is observed in this case and has similar qualitative features as particle simulations.

Regarding the simulation method, event-driven simulations of hard-spheres show a remarkable agreement with experiments in the collisional regimes. This further confirms the validity of the hard-sphere approximation for highly agitated systems. It is nevertheless necessary to consider velocity dependent restitution coefficients in order to capture the physics in high density regions. It was also shown that the speed advantage of event-driven simulations is crucial for the study of long transients or very high shaking frequencies.

OUTLOOK AND RECOMMENDATIONS

At many points throughout this thesis the phenomena observed suggests deeper or new lines of future research. In what follows an overview of such ideas is given.

- Exploring further the phase-space of the vertically vibrated quasi-one-dimensional geometry could lead to an even better understanding of low-frequency oscillations. Of special interest are the dependency of the oscillations on the particles' interaction properties, such as the coefficients of restitution and friction. A few exploratory simulations have shown that modifying the restitution coefficient could lead to higher amplitudes of oscillation for lower vibration strengths, facilitating future experimental realizations. Also of interest is the inclusion of adhesive forces, as they could lead to more strongly separated phases, a limit where the theoretical models are expected to work better.
- The complete equation of motion derived for density inverted continuum systems, before disregarding higher order terms, could be numerically solved. The inclusion of the non-linear terms should result in temporal evolutions more akin to those found in simulations, which are far from the regular oscillations of harmonic oscillators and closer to more chaotic dynamics. It would be

of interest to include a stochastic forcing (instead of the sinusoidal boundary condition used in our work), to model the particle number fluctuations which drive the oscillations, and see how the forcing statistics has to be adapted for systems with different numbers of particles. Furthermore, the energy equation could be included in the description, possibly improving the predictive nature of the model by obtaining the density and/or velocity fields.

- Experiments suggest the existence of an inverted convective state for very low energy injections, in which the particles go up at the walls. In simulations with higher energy injections inverted convective states were observed, but only in specific cases and for short times, whereas experiments showed that this state is possible for low energy injections and with high stability. Exactly what parameters make that state possible remains an open question, as also how stable it is. Simulations that can handle highly packed states more accurately should be employed for any study of this very dense regime phenomenon.
- It was observed in simulations that the critical size of the buoyancy-driven convective rolls is independent on the width of the container. The other determinant factors have been predicted by a stability analysis of the granular hydrodynamic equations. Confirming this predictions in a wide region of phase-space remains to be done. Moreover, Equivalent Leidenfrost states with different numbers of particles could be used to determine if the particle-size is relevant. First observations indicate that for a given dissipation the number of particle layers is indeed a determinant variable, although it is not know in what form and until what extent is this true.
- The amplitude equation relevant for a system of vibrated coupled oscillators of the form proposed to be present in the Leidenfrost state should be derived. This would confirm or deny the relevance of the proposed quintic supercritical bifurcation. Derivations have already been done for coupled chains of pendula—which could be an adequate starting point— although these do not consider the finite-size and number effects that are present in granular phenomena.
- Experiments of vertically vibrated grains inside a container filled with liquid, realized by fellow researchers, suggested the presence of low-frequency oscillations, although the measurements where not conclusive. Suspensions, including colloidal systems, could provide ways to test the generality of our results, as predicted by the derived continuum analysis. By lowering the density difference between the grains and the surrounding media it is expected that the same phenomena can be observed for lower energy injection values, although hydrodynamic interactions are also expected to have a significant influence.
- The buoyancy-driven convective state in wide containers was seen to present complex, time-dependent dynamics. Convective cells are seen to merge, split,

and coexist with the Leidenfrost state. The dependency of the characteristic time-scales of these phenomena on the system properties could yield further insight into the nature of buoyancy-driven convection in granular systems. First observations suggest that the restitution coefficient of the particles dramatically affects the observed behaviour.

- The analysis of equivalent macroscopic states with different numbers of particles should be applied to other granular states. In vibrated monolayers that undergo phase-separation, either for mono- or poly-disperse grains, the size of the domains and the fluctuations that alter its shape could be studied as a function of the discretization, i.e. number of particles. The theoretical analysis should also be extended to include binary mixtures, and several segregation phenomena could be analysed in this context, a scenario that could be also relevant for practical applications.

BIBLIOGRAPHY

- [1] H. M. Jaeger, S. R. Nagel, and R. P. Behringer, "Granular solids, liquids, and gases," *Reviews of Modern Physics*, vol. 68, p. 1259, Oct. 1996.
- [2] K. Z. Y. Yen and T. K. Chaki, "A dynamic simulation of particle rearrangement in powder packings with realistic interactions," *Journal of Applied Physics*, vol. 71, pp. 3164–3173, Apr. 1992.
- [3] P. Pierrat and H. S. Caram, "Tensile strength of wet granula materials," *Powder Technology*, vol. 91, pp. 83–93, May 1997.
- [4] C. Goldenberg and I. Goldhirsch, "Small and large scale granular statics," *Granular Matter*, vol. 6, pp. 87–96, Oct. 2004.
- [5] Y. Jiang and M. Liu, "Granular solid hydrodynamics," *Granular Matter*, vol. 11, pp. 139–156, May 2009.
- [6] I. Goldhirsch, "Scales and kinetics of granular flows," *Chaos: An Interdisciplinary Journal of Nonlinear Science*, vol. 9, pp. 659–672, Sept. 1999.
- [7] G. D. R. MiDi, "On dense granular flows," *The European Physical Journal E*, vol. 14, pp. 341–365, Aug. 2004.
- [8] Y. Forterre and O. Pouliquen, "Flows of dense granular media," *Annual Review of Fluid Mechanics*, vol. 40, no. 1, pp. 1–24, 2008.
- [9] I. Goldhirsch, "Rapid granular flows," *Annual Review of Fluid Mechanics*, vol. 35, no. 1, pp. 267–293, 2003.
- [10] L. P. Kadanoff, "Built upon sand: Theoretical ideas inspired by granular flows," *Reviews of Modern Physics*, vol. 71, pp. 435–444, Jan. 1999.
- [11] B. J. Glasser and I. Goldhirsch, "Scale dependence, correlations, and fluctuations of stresses in rapid granular flows," *Physics of Fluids (1994-present)*, vol. 13, pp. 407–420, Feb. 2001.
- [12] L. Bocquet, W. Losert, D. Schalk, T. C. Lubensky, and J. P. Gollub, "Granular shear flow dynamics and forces: Experiment and continuum theory," *Physical Review E*, vol. 65, p. 011307, Dec. 2001.

- [13] L. Bocquet, J. Errami, and T. C. Lubensky, "Hydrodynamic model for a dynamical jammed-to-flowing transition in gravity driven granular media," *Physical Review Letters*, vol. 89, p. 184301, Oct. 2002.
- [14] E. Khain and B. Meerson, "Onset of thermal convection in a horizontal layer of granular gas," *Physical Review E*, vol. 67, p. 021306, Feb. 2003.
- [15] B. Meerson, T. Pöschel, and Y. Bromberg, "Close-packed floating clusters: Granular hydrodynamics beyond the freezing point?," *Physical Review Letters*, vol. 91, p. 024301, July 2003.
- [16] J. A. Carrillo, T. Pöschel, and C. Salueña, "Granular hydrodynamics and pattern formation in vertically oscillated granular disk layers," *Journal of Fluid Mechanics*, vol. 597, pp. 119–144, Feb. 2008.
- [17] S. Luding, "Towards dense, realistic granular media in 2d," *Nonlinearity*, vol. 22, p. R101, Dec. 2009.
- [18] C. G. Johnson and J. M. N. T. Gray, "Granular jets and hydraulic jumps on an inclined plane," *Journal of Fluid Mechanics*, vol. 675, pp. 87–116, May 2011.
- [19] J. J. Brey, M. I. García de Soria, P. Maynar, and V. Buzón, "Homogeneous steady state of a confined granular gas," *Physical Review E*, vol. 88, p. 062205, Dec. 2013.
- [20] P. Shukla and M. Alam, "Nonlinear vorticity-banding instability in granular plane couette flow: higher-order landau coefficients, bistability and the bifurcation scenario," *Journal of Fluid Mechanics*, vol. 718, pp. 131–180, Mar. 2013.
- [21] D. R. Tunuguntla, O. Bokhove, and A. R. Thornton, "A mixture theory for size and density segregation in shallow granular free-surface flows," *Journal of Fluid Mechanics*, vol. 749, pp. 99–112, June 2014.
- [22] J. J. Brey, M. J. Ruiz-Montero, and F. Moreno, "Hydrodynamics of an open vibrated granular system," *Physical Review E*, vol. 63, p. 061305, May 2001.
- [23] C. K. K. Lun, "Kinetic theory for granular flow of dense, slightly inelastic, slightly rough spheres," *Journal of Fluid Mechanics*, vol. 233, pp. 539–559, Dec. 1991.
- [24] A. Goldshtein and M. Shapiro, "Mechanics of collisional motion of granular materials. part 1. general hydrodynamic equations," *Journal of Fluid Mechanics*, vol. 282, pp. 75–114, Jan. 1995.
- [25] J. T. Jenkins and C. Zhang, "Kinetic theory for identical, frictional, nearly elastic spheres," *Physics of Fluids (1994-present)*, vol. 14, pp. 1228–1235, Mar. 2002.

- [26] J. J. Brey, J. W. Dufty, C. S. Kim, and A. Santos, "Hydrodynamics for granular flow at low density," *Physical Review E*, vol. 58, pp. 4638–4653, Oct. 1998.
- [27] V. Garzó and J. W. Dufty, "Dense fluid transport for inelastic hard spheres," *Physical Review E*, vol. 59, pp. 5895–5911, May 1999.
- [28] G. H. Ristow, *Pattern Formation in Granular Materials*. No. 164 in Springer Tracts in Modern Physics, Springer, 2000.
- [29] I. S. Aranson and L. S. Tsimring, "Patterns and collective behavior in granular media: Theoretical concepts," *Reviews of Modern Physics*, vol. 78, pp. 641–692, June 2006.
- [30] J. S. Olafsen and J. S. Urbach, "Two-dimensional melting far from equilibrium in a granular monolayer," *Physical Review Letters*, vol. 95, p. 098002, Aug. 2005.
- [31] E. Khain and I. S. Aranson, "Hydrodynamics of a vibrated granular monolayer," *Physical Review E*, vol. 84, p. 031308, Sept. 2011.
- [32] R. Brito, D. Risso, and R. Soto, "Hydrodynamic modes in a confined granular fluid," *Physical Review E*, vol. 87, p. 022209, Feb. 2013.
- [33] D. I. Goldman, J. B. Swift, and H. L. Swinney, "Noise, coherent fluctuations, and the onset of order in an oscillated granular fluid," *Physical Review Letters*, vol. 92, p. 174302, Apr. 2004.
- [34] I. Ortega, M. G. Clerc, C. Falcón, and N. Mujica, "Subharmonic wave transition in a quasi-one-dimensional noisy fluidized shallow granular bed," *Physical Review E*, vol. 81, p. 046208, Apr. 2010.
- [35] J. E. Macías, M. G. Clerc, C. Falcón, and M. A. García-Ñustes, "Spatially modulated kinks in shallow granular layers," *Physical Review E*, vol. 88, p. 020201, Aug. 2013.
- [36] G. Agez, M. G. Clerc, E. Louvergneaux, and R. G. Rojas, "Bifurcations of emerging patterns in the presence of additive noise," *Physical Review E*, vol. 87, p. 042919, Apr. 2013.
- [37] L. A. da Silva, E. H. Colombo, and C. Anteneodo, "Effect of environment fluctuations on pattern formation of single species," *Physical Review E*, vol. 90, p. 012813, July 2014.
- [38] J. S. Olafsen and J. S. Urbach, "Clustering, order, and collapse in a driven granular monolayer," *Physical Review Letters*, vol. 81, pp. 4369–4372, Nov. 1998.

- [39] A. Prevost, P. Melby, D. A. Egolf, and J. S. Urbach, "Nonequilibrium two-phase coexistence in a confined granular layer," *Physical Review E*, vol. 70, p. 050301, Nov. 2004.
- [40] P. Melby, F. V. Reyes, A. Prevost, R. Robertson, P. Kumar, D. A. Egolf, and J. S. Urbach, "The dynamics of thin vibrated granular layers," *Journal of Physics: Condensed Matter*, vol. 17, p. S2689, June 2005.
- [41] P. M. Reis, R. A. Ingale, and M. D. Shattuck, "Caging dynamics in a granular fluid," *Physical Review Letters*, vol. 98, p. 188301, Apr. 2007.
- [42] M. G. Clerc, P. Cordero, J. Dunstan, K. Huff, N. Mujica, D. Risso, and G. Varas, "Liquid-solid-like transition in quasi-one-dimensional driven granular media," *Nature Physics*, vol. 4, pp. 249–254, Mar. 2008.
- [43] G. Castillo, N. Mujica, and R. Soto, "Fluctuations and criticality of a granular solid-liquid-like phase transition," *Physical Review Letters*, vol. 109, p. 095701, Aug. 2012.
- [44] D. Blair, I. S. Aranson, G. W. Crabtree, V. Vinokur, L. S. Tsimring, and C. Josseland, "Patterns in thin vibrated granular layers: Interfaces, hexagons, and superoscillons," *Physical Review E*, vol. 61, pp. 5600–5610, May 2000.
- [45] F. Melo, P. B. Umbanhowar, and H. L. Swinney, "Hexagons, kinks, and disorder in oscillated granular layers," *Physical Review Letters*, vol. 75, pp. 3838–3841, Nov. 1995.
- [46] P. B. Umbanhowar, F. Melo, and H. L. Swinney, "Localized excitations in a vertically vibrated granular layer," *Nature*, vol. 382, pp. 793–796, Aug. 1996.
- [47] A. Rosato, K. J. Strandburg, F. Prinz, and R. H. Swendsen, "Why the brazil nuts are on top: Size segregation of particulate matter by shaking," *Physical Review Letters*, vol. 58, pp. 1038–1040, Mar. 1987.
- [48] J. B. Knight, H. M. Jaeger, and S. R. Nagel, "Vibration-induced size separation in granular media: The convection connection," *Physical Review Letters*, vol. 70, pp. 3728–3731, June 1993.
- [49] D. C. Hong, P. V. Quinn, and S. Luding, "The reverse brazil nut problem: Competition between percolation and condensation," *Arxiv preprint cond-mat/0010459*, 2000.
- [50] T. Shinbrot and F. J. Muzzio, "Reverse buoyancy in shaken granular beds," *Physical Review Letters*, vol. 81, pp. 4365–4368, Nov. 1998.
- [51] R. Brito and R. Soto, "Competition of brazil nut effect, buoyancy, and inelasticity induced segregation in a granular mixture," *The European Physical Journal Special Topics*, vol. 179, pp. 207–219, Dec. 2009.

- [52] M. E. Möbius, B. E. Lauderdale, S. R. Nagel, and H. M. Jaeger, "Brazil-nut effect: Size separation of granular particles," *Nature*, vol. 414, pp. 270–270, Nov. 2001.
- [53] G. H. Ristow, G. Straßburger, and I. Rehberg, "Phase diagram and scaling of granular materials under horizontal vibrations," *Physical Review Letters*, vol. 79, pp. 833–836, Aug. 1997.
- [54] T. Schnautz, R. Brito, C. A. Kruelle, and I. Rehberg, "A horizontal brazil-nut effect and its reverse," *Physical Review Letters*, vol. 95, p. 028001, July 2005.
- [55] F. Pacheco-Vázquez, G. A. Caballero-Robledo, and J. C. Ruiz-Suárez, "Superheating in granular matter," *Physical Review Letters*, vol. 102, p. 170601, Apr. 2009.
- [56] N. Rivas, S. Ponce, B. Gallet, D. Risso, R. Soto, P. Cordero, and N. Mujica, "Sudden chain energy transfer events in vibrated granular media," *Physical Review Letters*, vol. 106, p. 088001, Feb. 2011.
- [57] F. Pacheco-Vázquez, F. Ludewig, and S. Dorbolo, "Dynamics of a grain-filled ball on a vibrating plate," *Physical Review Letters*, vol. 113, p. 118001, Sept. 2014.
- [58] A. D. Rosato, D. L. Blackmore, N. Zhang, and Y. Lan, "A perspective on vibration-induced size segregation of granular materials," *Chemical Engineering Science*, vol. 57, pp. 265–275, Jan. 2002.
- [59] A. Kudrolli, "Size separation in vibrated granular matter," *Reports on Progress in Physics*, vol. 67, p. 209, Mar. 2004.
- [60] B. Thomas, M. O. Mason, Y. A. Liu, and A. M. Squires, "Identifying states in shallow vibrated beds," *Powder Technology*, vol. 57, pp. 267–280, Apr. 1989.
- [61] S. Douady, S. Fauve, and C. Laroche, "Subharmonic instabilities and defects in a granular layer under vertical vibrations," *EPL (Europhysics Letters)*, vol. 8, p. 621, Apr. 1989.
- [62] J. Ze-Hui, W. Yun-Ying, and W. Jing, "Subharmonic motion of granular particles under vertical vibrations," *EPL (Europhysics Letters)*, vol. 74, p. 417, May 2006.
- [63] C. R. Wassgren, C. E. Brennen, and M. L. Hunt, "Vertical vibration of a deep bed of granular material in a container," *Journal of Applied Mechanics*, vol. 63, pp. 712–719, Sept. 1996.
- [64] S. Luding, E. Clément, J. Rajchenbach, and J. Duran, "Simulations of pattern formation in vibrated granular media," *EPL (Europhysics Letters)*, vol. 36, p. 247, Nov. 1996.

- [65] E. Clément, L. Vanel, J. Rajchenbach, and J. Duran, "Pattern formation in a vibrated two-dimensional granular layer," *Physical Review E*, vol. 53, pp. 2972–2975, Mar. 1996.
- [66] K. M. Aoki and T. Akiyama, "Spontaneous wave pattern formation in vibrated granular materials," *Physical Review Letters*, vol. 77, pp. 4166–4169, Nov. 1996.
- [67] K. M. Aoki, T. Akiyama, Y. Maki, and T. Watanabe, "Convective roll patterns in vertically vibrated beds of granules," *Physical Review E*, vol. 54, pp. 874–883, July 1996.
- [68] Y. Lan and A. D. Rosato, "Convection related phenomena in granular dynamics simulations of vibrated beds," *Physics of Fluids (1994-present)*, vol. 9, pp. 3615–3624, Dec. 1997.
- [69] H. K. Pak, E. Van Doorn, and R. P. Behringer, "Effects of ambient gases on granular materials under vertical vibration," *Physical Review Letters*, vol. 74, pp. 4643–4646, June 1995.
- [70] M. E. Möbius, X. Cheng, G. S. Karczmar, S. R. Nagel, and H. M. Jaeger, "Intruders in the dust: Air-driven granular size separation," *Physical Review Letters*, vol. 93, p. 198001, Nov. 2004.
- [71] P. Eshuis, K. v. d. Weele, D. v. d. Meer, R. Bos, and D. Lohse, "Phase diagram of vertically shaken granular matter," *Physics of Fluids (1994-present)*, vol. 19, p. 123301, Dec. 2007.
- [72] Y. Lan and A. D. Rosato, "Macroscopic behavior of vibrating beds of smooth inelastic spheres," *Physics of Fluids (1994-present)*, vol. 7, pp. 1818–1831, Aug. 1995.
- [73] A. Kudrolli, M. Wolpert, and J. P. Gollub, "Cluster formation due to collisions in granular material," *Physical Review Letters*, vol. 78, pp. 1383–1386, Feb. 1997.
- [74] J. G. Leidenfrost, "On the fixation of water in diverse fire," *International Journal of Heat and Mass Transfer*, vol. 9, pp. 1153–1166, Nov. 1966.
- [75] I. U. Vakarelski, J. O. Marston, D. Y. C. Chan, and S. T. Thoroddsen, "Drag reduction by leidenfrost vapor layers," *Physical Review Letters*, vol. 106, p. 214501, May 2011.
- [76] F. Celestini and G. Kirstetter, "Effect of an electric field on a leidenfrost droplet," *Soft Matter*, vol. 8, pp. 5992–5995, May 2012.

- [77] D. Quéré, “Leidenfrost dynamics,” *Annual Review of Fluid Mechanics*, vol. 45, no. 1, pp. 197–215, 2013.
- [78] R. Abdelaziz, D. Disci-Zayed, M. K. Hedayati, J.-H. Pöhls, A. U. Zillohu, B. Erkartal, V. S. K. Chakravadhanula, V. Duppel, L. Kienle, and M. Elbahri, “Green chemistry and nanofabrication in a levitated leidenfrost drop,” *Nature Communications*, vol. 4, Oct. 2013.
- [79] P. Eshuis, K. van der Weele, D. van der Meer, and D. Lohse, “Granular leidenfrost effect: Experiment and theory of floating particle clusters,” *Physical Review Letters*, vol. 95, p. 258001, Dec. 2005.
- [80] P. Eshuis, K. v. d. Weele, M. Alam, H. J. v. Gerner, M. v. d. Hoef, H. Kuipers, S. Luding, D. v. d. Meer, and D. Lohse, “Buoyancy driven convection in vertically shaken granular matter: experiment, numerics, and theory,” *Granular Matter*, vol. 15, pp. 893–911, Dec. 2013.
- [81] M. Faraday, “On a peculiar class of acoustical figures; and on certain forms assumed by groups of particles upon vibrating elastic surfaces,” *Philosophical Transactions of the Royal Society of London*, vol. 121, pp. 299–340, Jan. 1831.
- [82] R. A. Bagnold, *The Physics of Blown Sand and Desert Dunes*. Mineola, N.Y: Dover Publications, 1966.
- [83] S. Luding, “Molecular dynamics simulations of granular materials,” in *The Physics of Granular Media* (H. Hinrichsen and D. E. Wolf, eds.), pp. 297–324, Wiley-VCH Verlag GmbH & Co. KGaA, 2004.
- [84] P. A. Vermeer, S. Diebels, W. Ehlers, H. J. Herrmann, and S. Luding, *Continuous and Discontinuous Modelling of Cohesive-Frictional Materials*. No. 568 in Lecture Notes in Physics, Springer, 2001.
- [85] D. Krijgsman, V. Ogarko, and S. Luding, “Optimal parameters for a hierarchical grid data structure for contact detection in arbitrarily polydisperse particle systems,” *Computational Particle Mechanics*, vol. 1, pp. 357–372, Sept. 2014.
- [86] B. D. Lubachevsky, “How to simulate billiards and similar systems,” *Journal of Computational Physics*, vol. 94, pp. 255–283, June 1991.
- [87] S. Luding and S. McNamara, “How to handle the inelastic collapse of a dissipative hard-sphere gas with the TC model,” *Granular Matter*, vol. 1, pp. 113–128, Dec. 1998.
- [88] S. Miller and S. Luding, “Event-driven molecular dynamics in parallel,” *Journal of Computational Physics*, vol. 193, pp. 306–316, Jan. 2004.

- [89] S. Luding, M. Huthmann, S. McNamara, and A. Zippelius, "Homogeneous cooling of rough, dissipative particles: Theory and simulations," *Physical Review E*, vol. 58, pp. 3416–3425, Sept. 1998.
- [90] M. N. Bannerman, R. Sargant, and L. Lue, "DynamO: a free o(n) general event-driven molecular dynamics simulator," *Journal of Computational Chemistry*, vol. 32, pp. 3329–3338, Nov. 2011.
- [91] S. Luding and H. J. Herrmann, "Cluster-growth in freely cooling granular media," *Chaos (Woodbury, N.Y.)*, vol. 9, pp. 673–681, Sept. 1999.
- [92] R. Sondergaard, K. Chaney, and C. E. Brennen, "Measurements of solid spheres bouncing off flat plates," *Journal of Applied Mechanics*, vol. 112, pp. 694–699, Sept. 1990.
- [93] J. Schäfer, S. Dippel, and D. E. Wolf, "Force schemes in simulations of granular materials," *Journal de Physique I*, vol. 6, pp. 5–20, Jan. 1996.
- [94] S. F. Foerster, M. Y. Louge, H. Chang, and K. Allia, "Measurements of the collision properties of small spheres," *Physics of Fluids (1994-present)*, vol. 6, pp. 1108–1115, Mar. 1994.
- [95] S. Luding, "Collisions & contacts between two particles," in *Physics of Dry Granular Media* (H. J. Herrmann, J.-P. Hovi, and S. Luding, eds.), no. 350 in NATO ASI Series, pp. 285–304, Springer Netherlands, Jan. 1998.
- [96] L. Vu-Quoc, X. Zhang, and L. Lesburg, "A normal force-displacement model for contacting spheres accounting for plastic deformation: Force-driven formulation," *Journal of Applied Mechanics*, vol. 67, pp. 363–371, Sept. 1999.
- [97] L.-O. Heim, J. Blum, M. Preuss, and H.-J. Butt, "Adhesion and friction forces between spherical micrometer-sized particles," *Physical Review Letters*, vol. 83, pp. 3328–3331, Oct. 1999.
- [98] W. B. Russel, D. A. Saville, and W. R. Schowalter, *Colloidal Dispersions*. Cambridge University Press, 1989.
- [99] B. J. Alder and T. E. Wainwright, "Phase transition for a hard sphere system," *Journal of Chemical Physics*, vol. 27, pp. 1208–1209, Nov. 1957.
- [100] J. D. Bernal, "Geometry of the structure of monatomic liquids," *Nature*, vol. 185, pp. 68–70, Jan. 1960.
- [101] "Theory of simple liquids," in *Theory of Simple Liquids (Fourth Edition)* (J.-P. Hansen and I. R. McDonald, eds.), p. i, Oxford: Academic Press, 2013.

- [102] S. Luding, E. Clément, A. Blumen, J. Rajchenbach, and J. Duran, "Interaction laws and the detachment effect in granular media," in *Symposium P – Fractal Aspects of Materials*, vol. 367 of *MRS Online Proceedings Library*, Jan. 1994.
- [103] J. Duran, T. Mazozi, S. Luding, E. Clément, and J. Rajchenbach, "Discontinuous decompaction of a falling sandpile," *Physical Review E*, vol. 53, pp. 1923–1930, Feb. 1996.
- [104] J. Duran, *Sands, Powders, and Grains - An Introduction to the Physics of Granular Materials*. Partially Ordered Systems, Springer, 1997.
- [105] M. H. Kalos, D. Levesque, and L. Verlet, "Helium at zero temperature with hard-sphere and other forces," *Physical Review A*, vol. 9, pp. 2178–2195, May 1974.
- [106] S. Torquato and F. Lado, "Effective properties of two-phase disordered composite media: II. evaluation of bounds on the conductivity and bulk modulus of dispersions of impenetrable spheres," *Physical Review B*, vol. 33, pp. 6428–6435, May 1986.
- [107] W. G. Hoover and F. H. Ree, "Melting transition and communal entropy for hard spheres," *The Journal of Chemical Physics*, vol. 49, pp. 3609–3617, Oct. 1968.
- [108] S. Auer and D. Frenkel, "Numerical prediction of absolute crystallization rates in hard-sphere colloids," *The Journal of Chemical Physics*, vol. 120, pp. 3015–3029, Feb. 2004.
- [109] J. Duran, T. Mazozi, E. Clement, and J. Rajchenbach, "Decompaction modes of a two-dimensional "sandpile" under vibration: Model and experiments," *Physical Review E*, vol. 50, pp. 3092–3099, Oct. 1994.
- [110] M. D. Rintoul and S. Torquato, "Hard-sphere statistics along the metastable amorphous branch," *Physical Review E*, vol. 58, pp. 532–537, July 1998.
- [111] F. Melo, P. Umbanhowar, and H. L. Swinney, "Transition to parametric wave patterns in a vertically oscillated granular layer," *Physical Review Letters*, vol. 72, p. 172, Jan. 1994.
- [112] S. G. K. Tennakoon and R. P. Behringer, "Vertical and horizontal vibration of granular materials: Coulomb friction and a novel switching state," *Physical Review Letters*, vol. 81, p. 794, July 1998.
- [113] M. Medved, "Connections between response modes in a horizontally driven granular material," *Physical Review E*, vol. 65, p. 021305, Jan. 2002.

- [114] K. Ahmad and I. J. Smalley, "Observation of particle segregation in vibrated granular systems," *Powder Technology*, vol. 8, pp. 69–75, Aug. 1973.
- [115] J. G. Leidenfrost, "De aquae communis nonnullis qualitatibus tractatus," 1756.
- [116] S. Luding, "Granular materials under vibration: Simulations of rotating spheres," *Physical Review E*, vol. 52, pp. 4442–4457, Oct. 1995.
- [117] Y. Tatara and N. Moriwaki, "Study on impact of equivalent two bodies : Coefficients of restitution of spheres of brass, lead, glass, porcelain and agate, and the material properties," *Bulletin of JSME*, vol. 25, pp. 631–637, Apr. 1982.
- [118] S. McNamara and S. Luding, "Energy nonequipartition in systems of inelastic, rough spheres," *Physical Review E*, vol. 58, pp. 2247–2250, Aug. 1998.
- [119] C. R. K. Windows-Yule, N. Rivas, and D. J. Parker, "Thermal convection and temperature inhomogeneity in a vibrofluidized granular bed: The influence of sidewall dissipation," *Physical Review Letters*, vol. 111, p. 038001, July 2013.
- [120] M. N. Bannerman, J. E. Kollmer, A. Sack, M. Heckel, P. Mueller, and T. Pöschel, "Movers and shakers: Granular damping in microgravity," *Physical Review E*, vol. 84, p. 011301, July 2011.
- [121] R. Ramírez, D. Risso, and P. Cordero, "Thermal convection in fluidized granular systems," *Physical Review Letters*, vol. 85, pp. 1230–1233, Aug. 2000.
- [122] E. W. C. Lim, "Granular leidenfrost effect in vibrated beds with bumpy surfaces," *The European Physical Journal E*, vol. 32, pp. 365–375, Aug. 2010.
- [123] N. Rivas, S. Luding, and A. R. Thornton, "Low-frequency oscillations in narrow vibrated granular systems," *New Journal of Physics*, vol. 15, p. 113043, Nov. 2013.
- [124] J. S. van Zon, J. Kreft, D. I. Goldman, D. Miracle, J. B. Swift, and H. L. Swinney, "Crucial role of sidewalls in velocity distributions in quasi-two-dimensional granular gases," *Physical Review E*, vol. 70, p. 040301, Oct. 2004.
- [125] K. Feitosa and N. Menon, "Breakdown of energy equipartition in a 2d binary vibrated granular gas," *Physical Review Letters*, vol. 88, p. 198301, Apr. 2002.
- [126] D. J. Parker, R. N. Forster, P. Fowles, and P. S. Takhar, "Positron emission particle tracking using the new birmingham positron camera," *Nuclear Instruments and Methods in Physics Research Section A: Accelerators, Spectrometers, Detectors and Associated Equipment*, vol. 477, pp. 540–545, Jan. 2002.

- [127] R. D. Wildman, J. M. Huntley, J.-P. Hansen, D. J. Parker, and D. A. Allen, "Single-particle motion in three-dimensional vibrofluidized granular beds," *Physical Review E*, vol. 62, pp. 3826–3835, Sept. 2000.
- [128] S. McNamara and E. Falcon, "Simulations of vibrated granular medium with impact-velocity-dependent restitution coefficient," *Physical Review E*, vol. 71, p. 031302, Mar. 2005.
- [129] J. M. Lifshitz and H. Kolsky, "Some experiments on anelastic rebound," *Journal of the Mechanics and Physics of Solids*, vol. 12, pp. 35–43, Feb. 1964.
- [130] T. Pöschel, N. V. Brilliantov, and T. Schwager, "Long-time behavior of granular gases with impact-velocity dependent coefficient of restitution," *Physica A: Statistical Mechanics and its Applications*, vol. 325, pp. 274–283, July 2003.
- [131] V. Folli, N. Ghofraniha, A. Puglisi, L. Leuzzi, and C. Conti, "Time-resolved dynamics of granular matter by random laser emission," *Scientific Reports*, vol. 3, July 2013.
- [132] J. A. C. Gallas, H. J. Herrmann, T. Pöschel, and S. Sokolowski, "Molecular dynamics simulation of size segregation in three dimensions," *Journal of Statistical Physics*, vol. 82, no. 1, pp. 443–450, 1996.
- [133] T. S. Majmudar, M. Sperl, S. Luding, and R. P. Behringer, "Jamming transition in granular systems," *Physical Review Letters*, vol. 98, p. 058001, Jan. 2007.
- [134] J. Talbot and P. Viot, "Wall-enhanced convection in vibrofluidized granular systems," *Physical Review Letters*, vol. 89, p. 064301, July 2002.
- [135] J. B. Knight, "External boundaries and internal shear bands in granular convection," *Physical Review E*, vol. 55, pp. 6016–6023, May 1997.
- [136] R. D. Wildman, J. M. Huntley, and D. J. Parker, "Convection in highly fluidized three-dimensional granular beds," *Physical Review Letters*, vol. 86, pp. 3304–3307, Apr. 2001.
- [137] M. G. Clerc, P. Cordero, J. Dunstan, K. Huff, N. Mujica, D. Risso, and G. Varas, "Liquid–solid-like transition in quasi-one-dimensional driven granular media," *Nature Physics*, vol. 4, pp. 249–254, Mar. 2008.
- [138] J. M. Ottino and D. V. Khakhar, "Mixing and segregation of granular materials," *Annual Review of Fluid Mechanics*, vol. 32, no. 1, pp. 55–91, 2000.
- [139] F. J. Muzzio, T. Shinbrot, and B. J. Glasser, "Powder technology in the pharmaceutical industry: the need to catch up fast," *Powder Technology*, vol. 124, pp. 1–7, Apr. 2002.

- [140] P. Coussot, *Rheometry of Pastes, Suspensions, and Granular Materials: Applications in Industry and Environment*. John Wiley & Sons, June 2005.
- [141] S. J. Antony, W. Hoyle, and Y. Ding, *Granular Materials: Fundamentals and Applications*. Royal Society of Chemistry, Jan. 2004.
- [142] S. T. Thoroddsen and A. Q. Shen, "Granular jets," *Physics of Fluids (1994-present)*, vol. 13, pp. 4–6, Jan. 2001.
- [143] J. R. Royer, D. J. Evans, L. Oyarte, Q. Guo, E. Kapit, M. E. Möbius, S. R. Waitukaitis, and H. M. Jaeger, "High-speed tracking of rupture and clustering in freely falling granular streams," *Nature*, vol. 459, pp. 1110–1113, June 2009.
- [144] J. Garcia-Ojalvo and J. Sancho, *Noise in Spatially Extended Systems*. Institute for Nonlinear Science, Springer, 1999.
- [145] D. L. Blair and A. Kudrolli, "Clustering transitions in vibrofluidized magnetized granular materials," *Physical Review E*, vol. 67, p. 021302, Feb. 2003.
- [146] J. Stambaugh, Z. Smith, E. Ott, and W. Losert, "Segregation in a monolayer of magnetic spheres," *Physical Review E*, vol. 70, p. 031304, Sept. 2004.
- [147] B. Miller, C. O'Hern, and R. P. Behringer, "Stress fluctuations for continuously sheared granular materials," *Physical Review Letters*, vol. 77, pp. 3110–3113, Oct. 1996.
- [148] G. Seiden and P. J. Thomas, "Complexity, segregation, and pattern formation in rotating-drum flows," *Reviews of Modern Physics*, vol. 83, pp. 1323–1365, Nov. 2011.
- [149] C. R. K. Windows-Yule and D. J. Parker, "Inelasticity-induced segregation: Why it matters, when it matters," *EPL (Europhysics Letters)*, vol. 106, p. 64003, June 2014.
- [150] P. Eshuis, D. van der Meer, M. Alam, H. J. van Gerner, K. van der Weele, and D. Lohse, "Onset of convection in strongly shaken granular matter," *Physical Review Letters*, vol. 104, p. 038001, Jan. 2010.
- [151] P. Couillet, T. Frisch, and G. Sonnino, "Dispersion-induced patterns," *Physical Review E*, vol. 49, pp. 2087–2090, Mar. 1994.
- [152] M. G. Clerc, S. Coulibaly, and D. Laroze, "Localized states beyond the asymptotic parametrically driven amplitude equation," *Physical Review E*, vol. 77, p. 056209, May 2008.
- [153] R. Soto, "Granular systems on a vibrating wall: The kinetic boundary condition," *Physical Review E*, vol. 69, p. 061305, June 2004.

- [154] H. J. Herrmann and S. Luding, "Modeling granular media on the computer," *Continuum Mechanics and Thermodynamics*, vol. 10, pp. 189–231, Aug. 1998.
- [155] I. Prigogine, *Self-Organization in Nonequilibrium Systems: From Dissipative Structures to Order through Fluctuations*. New York: Wiley, 1 edition ed., May 1977.
- [156] E. Bodenschatz, W. Pesch, and G. Ahlers, "Recent developments in rayleigh-bénard convection," *Annual Review of Fluid Mechanics*, vol. 32, no. 1, pp. 709–778, 2000.
- [157] J. Oh and G. Ahlers, "Thermal-noise effect on the transition to rayleigh-bénard convection," *Physical Review Letters*, vol. 91, p. 094501, Aug. 2003.
- [158] C. R. K. Windows-Yule, N. Rivas, D. J. Parker, and A. R. Thornton, "Low-frequency oscillations and convective phenomena in a density-inverted vibrofluidized granular system," *Physical Review E*, vol. 90, p. 062205, Dec. 2014.
- [159] J. H. P. Dawes, "The emergence of a coherent structure for coherent structures: localized states in nonlinear systems," *Philosophical Transactions of the Royal Society A: Mathematical, Physical and Engineering Sciences*, vol. 368, pp. 3519–3534, Aug. 2010.
- [160] J. Swift and P. C. Hohenberg, "Hydrodynamic fluctuations at the convective instability," *Physical Review A*, vol. 15, pp. 319–328, Jan. 1977.
- [161] G. Agez, M. G. Clerc, and E. Louvergneaux, "Universal shape law of stochastic supercritical bifurcations: Theory and experiments," *Physical Review E*, vol. 77, p. 026218, Feb. 2008.
- [162] B. J. Alder and T. E. Wainwright, "Studies in molecular dynamics. i. general method," *The Journal of Chemical Physics*, vol. 31, pp. 459–466, Aug. 1959.
- [163] R. Soto and M. M. Mansour, "Hydrodynamic boundary condition in vibrofluidized granular systems," *Physica A: Statistical Mechanics and its Applications*, vol. 369, pp. 301–308, Sept. 2006.
- [164] J. M. N. T. Gray, M. Wieland, and K. Hutter, "Gravity-driven free surface flow of granular avalanches over complex basal topography," *Proceedings of the Royal Society of London A: Mathematical, Physical and Engineering Sciences*, vol. 455, pp. 1841–1874, May 1999.
- [165] E. L. Grossman, T. Zhou, and E. Ben-Naim, "Towards granular hydrodynamics in two dimensions," *Physical Review E*, vol. 55, p. 4200, Apr. 1997.

- [166] D. R. Moore and N. O. Weiss, "Two-dimensional rayleigh-benard convection," *Journal of Fluid Mechanics*, vol. 58, pp. 289–312, Apr. 1973.
- [167] A. Puhl, M. M. Mansour, and M. Mareschal, "Quantitative comparison of molecular dynamics with hydrodynamics in rayleigh-b\'enard convection," *Physical Review A*, vol. 40, pp. 1999–2012, Aug. 1989.
- [168] H. P. Langtangen, "A FEniCS tutorial," in *Automated Solution of Differential Equations by the Finite Element Method* (A. Logg, K.-A. Mardal, and G. Wells, eds.), no. 84 in *Lecture Notes in Computational Science and Engineering*, pp. 1–73, Springer Berlin Heidelberg, Jan. 2012.

ACKNOWLEDGEMENTS

It feels strange to *write* “thank you”; I will always prefer a hug, and a strong handshake will also do if the social conventions and local customs so demand. But the greedy thesis is always hungry for more, and I don’t want to make her angry just before saying goodbye. I’ll dedicate just a few words to nostalgia: these four years were definitely adventurous, or maybe I should say novelesque, to pay at least some homage to my other companion, literature. I’m sure than more than anything I’ll remember the people, because few things in life are really better than those moments of real friendship and love. Enschede will be the crazy happenings, the laughs, definitely the best conversations and maybe the emergency trips; Enschede for sure will be the place where I met and fell in love with Sophie. I’ve already dedicated a few pages to science (see Chapter 2), so nothing more to say about that, just “farewell, ideas”. It should be enough to say that dedicating just a second or two to the memories of these years, and this work, leave me with a great feeling, something like a deep smile.

First, I say out of profound gratitude that nothing of this thesis would have been possible without the incredible support from Stefan and Anthony. Thank you for trusting in me and giving me so much freedom, for being there when I needed you, and for the incredible collaboration opportunities. Your confidence in me was an enormous gift, thank you so much. Thank you Ant for the trips and all the great scenes, I think we did a great job of walking on the thin line between job and fun. I learned from you both and enjoyed your company; you were great.

I would also like to especially thank Devaraj, for all the time and effort you dedicated to me without any official obligations, but just out of pure scientific and teaching spirit; that was very inspiring. Thank you for all the attention you paid to our work, the invitations, the patience, and the great scientific discussions. Your positive spirit and energy are contagious.

I know a few words wont do justice (at least not in all cases), but I would like to thank: Sebastian, for the drive, dialogue and genius; Chanse, for the talks and the inspiring energy; SinQuenza, for the flow, the adventures and the joyful friendship; Sylvia, for her incredible humour, help with everything and keeping things in perspective; Loraine and Zainab, for feeding me in the worst of times, and keeping the house full of life; Mike, for the guitar soundtrack; Vanessa and Kuni, for making the office such a nice place to work in; Thomas, for the careful revision of the maths; Abhi, for the help with the thesis; Chris, for the translation and refreshing humour; Vitaliy, for the nice discussions; to the rest of the MSM group: thanks for

the nice spirit, the talks, the dinners and the infinitely varied perspectives; Kit, for all the work and power, together with Dave Parker, for letting us use their incredible facilities; Sander, for the collaboration and the lovely tours of Oxford; Leah, for the refreshing attitude; Ivan, for those walks and talks; Lissy, for the contagious cheerful spirit; Nekane, for the laughs; Elena, for the awesomeness; all the AKI people, for the parties and keeping me sane; Vasko, for the comedy, for the Ireland memories, and for somehow leading me to Sophie; Yoyo, for the wedding and the jazz; all the guys from Brinkstraat and the conservatory; Fabian, for the fun fun fun and the print; Nicolas, for the knowledge; Dino, for the coding; Rodrigo, Nicolas, Patricio, Marcel, for the inspiration; Leonardo and Loreto, the parents, for all the help and bringing Chile to Enschede; Juancho and Adriana, for the funny lunches; Federico and Rodolfo, for sharing the party that I'm sure will be historical; Enrique, for the cumbias; all the rest of the POF guys, for being in the university; all the tango people who will never read this, for the passion of dancing and the strange worlds; Kita, for the visit to Enschede and the trips; the Chatismo Magico: Lletto, Josefina, Correa, Andrea, Ferre, Feña, Montt, Caco, Coni, Coloro, Coca, for the magic and love; Joe, for being present and always wishing the best; my family, for so many things; and Sophie, for the care, the love, my deepest happiness, and all the other things that lie far beyond words.

PUBLICATIONS

DURING DOCTORATE:

- Low-frequency oscillations and convective phenomena in a density-inverted vibrofluidised granular system
C.R.K. Windows-Yule, N. Rivas, D.J. Parker, A.R. Thornton
Physical Review E, 90 (6), 062205, 2014.
- Influence of initial conditions on granular dynamics near the jamming transition¹
C.R.K. Windows-Yule, A.D. Rosato, N. Rivas, D.J. Parker
New Journal of Physics 16 (6), 063016, 2014.
- Structure characterization of hard sphere packings in amorphous and crystalline states¹
V. Ogarko, N. Rivas, S. Luding
The Journal of Chemical Physics 140 (21), 211102, 2014.
- Low-frequency oscillations in narrow vibrated granular systems
N. Rivas, S. Luding, A.R. Thornton
New Journal of Physics 15 (11), 113043, 2013.
- Thermal convection and temperature inhomogeneity in a vibrofluidized granular bed: the influence of sidewall dissipation¹
C.R.K. Windows-Yule, N. Rivas, D.J. Parker
Physical Review Letters 111 (3), 038001, 2013.
- Phase-coexisting patterns with segregation and controlled convection in vertically vibrated binary granular mixtures¹
I. Ansari, N. Rivas, A. Meheboob
Physical Review Letters, Submitted.
- From the granular Leidenfrost state to buoyancy-driven convection
N. Rivas, A.R. Thornton, S. Luding, D. van der Meer
Physical Review E. Submitted.

1. Not presented in the thesis.

- Size-scalings of granular hydrodynamics.
N. Rivas, S. Luding, D. van der Meer
In preparation.
- Hydrodynamics of the granular Leidenfrost state.
N. Rivas, S. Rhebergen, A. Thornton
In preparation.

PREVIOUS WORK:

- Characterization of the energy bursts in vibrated granular systems
N. Rivas, P. Cordero, D. Risso, R. Soto
Granular Matter 14 (2), 157-162, 2012.
- Sudden chain energy transfer events in vibrated granular media
N. Rivas, S. Ponce, B. Gallet, D. Risso, R. Soto, P. Cordero, N. Mujica
Physical Review Letters 106 (8), 88001, 2011.
- Segregation in quasi-two-dimensional granular systems
N. Rivas, P. Cordero, D. Risso, R. Soto
New Journal of Physics 13, 055018, 2011.

SUMMARY

The subject of this thesis is the dynamics of granular materials. Granular matter is defined as collections of macroscopic, dissipative particles. The size of the individual particles (grains) must be large enough so that thermal fluctuations may be ignored. The loss of kinetic energy at every grain-grain collision implies the need of an external energy source to keep grains in movement. This thesis centres on a specific energy injection method: vibrated systems, where the grains container is shaken such that particles gain energy through collisions with the walls. As far-from-equilibrium dissipative systems, vibrated granular matter presents many distinct out-of-equilibrium stable states and complex transitions between them. In this thesis both particle simulations and different continuum models are used to investigate further the relation between discrete and continuum descriptions of particle systems, a subject of fundamental scientific interest.

A collective, semi-periodic movement of the grains inside vertically vibrated containers is for the first time identified and characterized. A simulational study of these oscillations is presented in Chapter 2, and Chapter 3 mainly describes an experimental observation of it. The oscillations take place in density-inverted states, such as the granular Leidenfrost effect, where grains separate in a high temperature region near the moving bottom wall and a dense region on top. The quasiperiodic movement is usually orders of magnitude slower than the energy injection shaking frequency, thus they are named low-frequency oscillations (LFOs). Furthermore, from the equations of mass and momentum conservation in continuum media an expression for the typical natural oscillation frequency is derived, in good agreement with both simulations and experiments in the high energy injection limit.

Increasing the energy input and system size takes the system from the granular Leidenfrost state to a buoyancy-driven convective state. Chapter 4 presents an in-depth study of this transition, revealing the existence of fluctuating convective flows far before the transition, as also suggesting a reinterpretation of the dynamics that includes the influence of LFOs. The characteristic length and time-scales of precursory fluctuations are measured, and the amplitude of the critical mode is observed to be consistent with a quintic supercritical amplitude equation.

The last two chapters of this thesis study the granular Leidenfrost to convection transition using granular hydrodynamics. Chapter 5 deals directly with the relation of discrete and continuum descriptions of granular systems. A methodology is proposed to quantify the finite-number effects on fluctuations, involving scalings that leave the granular hydrodynamic equations invariant while varying the total num-

ber of particles. This method allows us to conclude that LFOs are a finite-number, discretization phenomena, although the mode of oscillation is seen to be a macroscopically determined quantity. In Chapter 6 the granular hydrodynamic equations are numerically solved, and the solutions compared with particle simulations. Deviations of the continuum model due to finite-size and higher order effects are discussed. Finally, it is observed that to first order the transition can be understood as a Rayleigh-Bernard instability described by Navier-Stokes-like equations in the Boussinesq approximation.

SAMENVATTING

Dit proefschrift onderzoekt de dynamica van granulaire materie: groepen van macroscopische deeltjes met energetische verliezen. De grootte van de individuele deeltjes is dermate gekozen dat thermische fluctuaties verwaarloosd kunnen worden. Kenetische energie wordt bij elke botsing tussen verschillende deeltjes omgezet in warmte, wat impliceert dat er een externe bron nodig is om de deeltjes in beweging te houden. Dit proefschrift richt zich op trillende systemen, waarbij een omhulsel met daarin deeltjes in zijn geheel dermate geschud wordt, dat er energie wordt toegevoegd door botsingen tussen de deeltjes en het omhulsel. Zoals vaker in systemen ver van een evenwicht, zijn er in granulaire materie in aangeslagen toestand veel verschillende stabiele staten uit evenwicht te vinden, met complexe overgangen tussen deze.

De eerste twee hoofdstukken zijn toegewijd aan een nieuw gemeenschappelijk gedrag waargenomen in een vertikaal trillend systeem met een laag van deeltjes. Wanneer sterk aangeslagen, scheiden de deeltjes zich in een regio met een hogere temperatuur aan de onderzijde en een regio met een hogere dichtheid aan de bovenzijde, vergelijkbaar met het Leidenfrost-effect waar vloeistof zich begeeft boven gas. In deze situatie met een omgekeerde dichtheid nemen we, zowel in simulaties als experimenten, waar dat er een semi-periodieke verplaatsing plaatsvindt binnen de laag deeltjes, met een snelheid van enkele ordergroottes lager dan de externe trillingen. Wij noemen dergelijke semi-periodieke verplaatsingen ook wel laag-frequente oscillaties (LFO's). Typische amplitudes en frequenties blijken respectievelijk evenredig en omgekeerd evenredig met de toegevoerde hoeveelheid energie samen te hangen. Bovendien leiden we van de wetten van behoud van massa en impuls uitdrukkingen af voor de typische frequentie van de oscillaties welke overeenstemmen met zowel simulaties als experimenten.

Het vergroten van de energie-toevoer laat het systeem overgaan van een Leidenfrost-staat voor granulaire materie tot een door drijfvermogen gedreven convectieve staat. In hoofdstuk 3 wordt deze overgang beschreven aan de hand van de bifurcatietheorie. De karakteristieke lengte en tijdschaal van de voorafgaande fluctuaties zijn gemeten en de amplitude van de kritische mode blijken uit waarnemingen overeen te stemmen met de vijfdegraadsvergelijking voor superkritische amplitudes. Dit leidt ons om de dynamica van de Leidenfrost staat ter herinterpreteren als een serie van gekoppelde oscillatoren, daarbij meegenomen de aanwezigheid van de voorheen genoemde LFO's.

De laatste twee hoofdstukken van dit proefschrift onderzoeken de overgang tussen

het granulaire Leidenfrost en een staat van convectie met behulp van granulaire hydrodynamica. Met als doel het kwantificeren van een eindig aantal effecten in de voorafgaande fluctuaties, stellen we een methode voor om macroscopisch equivalente systemen met aanzienlijk verschillende hoeveelheden deeltjes te vinden. Deze verschalingen zijn afgeleid zodat de granulaire hydrodynamische vergelijkingen onafhankelijk blijven van de grootte van de deeltjes. Dit blijkt alleen mogelijk te zijn in het geval van een tijdsinvariante staat, waarbij simulaties een convergerend macroscopisch veld laten zien. Tijdens de overgang blijken de ruis-termen van de amplitudevergelijkingen, welke de groei van de kritische modes beschrijven, omgekeerd evenredig te zijn ten opzichte van de totale hoeveelheid deeltjes in het systeem. Daarnaast zijn de granulaire hydrodynamische vergelijkingen numeriek opgelost voor het bestudeerde systeem, wat bevestigt dat tot de eerste orde de overgang begrepen kan worden als een Rayleigh-Bernard instabiliteit beschreven door de Navier-Stokes-achtige vergelijkingen in de Boussinesq-benadering. Ten slotte worden de afwijkingen van deze klassieke overgang door het gebruik van een eindige hoeveelheid deeltjes en hogere orde effecten bestudeerd.